



AFAL TR-87-043

AD:

**AD-A189 808**

Final Report  
for the period  
30 Sept 1985 to  
31 March 1987

# **Crack Opening and Extension in Inert Solid Propellant**

## **An Experimental Study**

**DTIC**  
**ELECTE**  
**S** JAN 05 1988 **D**  
H

September 1987

Authors:  
D. Post  
C. W. Smith  
in Collaboration  
with  
R. Czarnek

Virginia Polytechnic Institute & State Univ.  
Dept. of Engineering Science & Mechanics  
Blacksburg, VA 24061

F04611-85-C-0098  
352-236-1

### **Approved for Public Release**

Distribution is unlimited. The AFAL Technical Services Office has reviewed this report, and it is releasable to the National Technical Information Service, where it will be available to the general public, including foreign nationals.

*prepared for the:* **Air Force  
Astronautics  
Laboratory**

Air Force Space Technology Center  
Space Division, Air Force Systems Command  
Edwards Air Force Base,  
California 93523-5000

**NOTICE TO ACCOMPANY THE DISSEMINATION OF  
EXPORT-CONTROLLED TECHNICAL DATA**

1. Export of information contained herein, which includes, in some circumstances, release to foreign nationals within the United States, without first obtaining approval or license from the Department of State for items controlled by the International Traffic in Arms Regulations (ITAR), or the Department of Commerce for items controlled by the Export Administration Regulations (EAR), may constitute a violation of law.

2. Under 22 U.S.C. 2778 the penalty for unlawful export of items or information controlled under the ITAR is up to 2 years imprisonment, or a fine of \$100,000, or both. Under 50 U.S.C., Appendix 2410, the penalty for unlawful export of items or information controlled under the EAR is a fine of up to \$1,000,000, or five times the value of the exports, whichever is greater; or for an individual, imprisonment of up to 10 years, or a fine of up to \$250,000, or both.

3. In accordance with your certification that establishes you as a "qualified U.S. contractor," unauthorized dissemination of this information is prohibited and may result in disqualification as a qualified U.S. contractor, and may be considered in determining your eligibility for future contracts with the Department of Defense.

4. The U.S. Government assumes no liability for direct patent infringement, or contributory patent infringement or misuse of technical data.

5. The U. S. Government does not warrant the adequacy, accuracy, currency, or completeness of the technical data.

6. The U.S. Government assumes no liability for loss, damage, or injury resulting from manufacture or use for any purpose of any product, article, system, or material involving reliance upon any or all technical data furnished in response to the request for technical data.

7. If the technical data furnished by the Government will be used for commercial manufacturing or other profit potential, a license for such use may be necessary. Any payments made in support of the request for data do not include or involve any license rights.


8. A copy of this notice shall be provided with any partial or complete reproduction of these data that are provided to qualified U.S. contractors.

## FOREWORD


This final report on Crack Opening and Extension in Inert Solid Propellant was submitted by Virginia Polytechnic Institute & State University under contract number F04611-85-C-0098 with the Air Force Astronautics Laboratory (AFAL), Edwards Air Force Base, CA 93523-5000. W. R. Lloyd, M. Rezvani, T. J. Theiss, Y. Guo, B. Han, and J. Jo provided valuable assistance in conducting the experiments reported in this study. The AFAL project manager was Dr C. T. Liu.

This technical report has been reviewed and is approved for publication and distribution in accordance with the distribution statement on the cover and on the DD Form 1473.

  
CHI T. LIU  
Project Manager

  
FRANCISCO Q. ROBERTO  
Chief, Propellant Development  
Branch

FOR THE COMMANDER

  
KENNETH E. MURPHY, Lt Col, USAF  
Deputy Director  
Solid Rocket Division

Accession For	
NTIS GRA&I	<input checked="checked" type="checkbox"/>
DTIC TAB	<input type="checkbox"/>
Unannounced	<input type="checkbox"/>
Justification	
By	
Distribution/	
Availability Code	
Dist	Avail and/or Special
A-1	

Block 11. Experimental Study

Block 19.

utilized to infer the distribution of the dominant eigenvalue through the thickness of the model in a continuum sense. Free surface values compare favorably with Benthem's analytical result. The near tip material response was strongly influenced by its heterogeneous nature.

## TABLE OF CONTENTS

	<u>Page</u>
INTRODUCTION .....	1
Program Objectives .....	1
Program Scope .....	2
WORK PLAN AND ACCOMPLISHMENTS .....	2
Singularity Order Measurement; Background and Techniques ...	2
Singularity Order Distribution .....	12
Inert Propellant Tests: Deformation Measurement Methods and Results .....	14
Specimen and Loading .....	14
Displacement Measurements, Methods .....	18
Utility of W Measurements .....	20
Test Conditions .....	23
Results: Representative Raw Data .....	23
Results: Crack Blunting .....	31
Results: Fracture Surfaces .....	35
Results: Global Deformations .....	39
Interpretation: Process Zone .....	55
Determination of $\lambda_u$ for Inert Propellant .....	57
SUMMARY AND RECOMMENDATIONS .....	64
Summary .....	64
Recommendations .....	67
REFERENCES .....	68
APPENDIX A INSERTION OF CRACKS IN POLYURETHANE MODELS .....	70
APPENDIX B ALGORITHMS FOR CONVERTING OPTICAL DATA INTO FRACTURE PARAMETERS (LEFM AND $\lambda_u$ UNDEFINED) .....	70
Mode I LEFM Algorithm for Photoelastic Data .....	70
Mode I LEFM Moire Algorithm .....	73
Algorithms for Accounting for Free Boundary Effect on the Crack Tip Singularity at the Free Surface .....	75
References .....	76
APPENDIX C ALGORITHMS FOR CONVERTING OPTICAL DATA INTO FRACTURE PARAMETERS ( $\lambda_u$ UNDEFINED) .....	76
Photoelastic Algorithms for Accounting for Free Boundary Effect on the Crack Tip Singularity at the Free Surface .....	76
References .....	79
APPENDIX D CHOICE OF EXPERIMENTAL METHODS .....	79
References .....	81
APPENDIX E THE GRID METHOD .....	81
Printing the Grid .....	81
Test Apparatus and Procedure .....	83

Data Extraction .....	85
Data Reduction .....	85
APPENDIX F SHADOW MOIRE METHOD .....	86
APPENDIX G U,V,W METHOD .....	87
References .....	93
APPENDIX H PHENOMENOLOGICAL ANALYSIS OF CRACK OPENING AND	
GROWTH .....	93
Introduction .....	93
Crack Blunting .....	93
Localization of the Pre-crack Zone .....	94
Rubber-rich Surface Layer .....	97
Auxiliary Observations .....	97
Failure Process .....	99
Force Transfer .....	103
Crack Growth .....	105
Oblique Paths and Shear Strains .....	105
Failure of Ligaments and Surface Layer .....	107
Path of Crack Growth .....	110
Crack Stoppers, Bridges .....	112
References .....	114

# LIST OF FIGURES

	<u>Page</u>
Fig. 1 Plan View of Large and Small Specimen Configurations for Polyurethane .....	5
Fig. 2 Test Setup for Moire Displacement Measurements on Polyurethane Specimens .....	6
Fig. 3 Typical (a) Photoelastic and (b) Moire Near Tip Fringe Patterns for a Small Polyurethane Model .....	8
Fig. 4 Determination of $\lambda_u$ from Moire Data for a Small Polyurethane Specimen .....	9
Fig. 5 Crack Front Curvature of Growing Crack .....	11
Fig. 6 Compact Bending Specimen Used in Stress Freezing Work	13
Fig. 7 Determination of $\sigma^0/\sigma$ from Raw Photoelastic Data from a Single Slice .....	15
Fig. 8 Determination of $\lambda_g$ from Test Data .....	16
Fig. 9 Distribution of $\lambda$ Across the Half Thickness of a Compact Bending Specimen .....	17
Fig. 10 Load vs. Grip Displacement of Test 1 .....	19
Fig. 11 Shadow moire pattern of W field. Test 8; 0.6 in. (15 mm) thick specimen; 1.0 in. (25 mm) per min load rate; maximum crack opening prior to crack growth; sensitivity 0.002 in. (0.05 mm) per fringe order .....	21
Fig. 12 Projection moire pattern of W field. 0.6 in. (15 mm) thick specimen; crack growth phase; sensitivity 0.0011 in. (0.028 mm) per fringe order .....	22
Fig. 13a Grid deformations during the crack blunting phase. Test 1; specimen thickness 0.2 in. (5 mm); cross-head speed 0.05 in. (1.3 mm)/min. ....	25
Fig. 13b Grid deformations during the crack growth phase .....	27
Fig. 14 Deformation for maximum crack opening prior to crack growth. (a) Spec. 1; (b) Spec. 10; (c) Spec. 3 .....	32
Fig. 14 cont. Deformation for maximum crack opening prior to crack growth. (d) Spec. 5; (e) Spec. 7; (f) Spec. 8	33
Fig. 15a Deformation during crack growth phase, Grid 125 lines per inch (5 lines per mm) .....	36

	<u>Page</u>
Fig. 15b Deformation during crack growth phase. Grid 500 lines per inch (20 lines per mm); Specimen 9 .....	38
Fig. 16a Displaced positions of digitized grid points. Test 1, frame 12 .....	40
Fig. 16b Contour map of V displacement. Test 1, frame 12. V = 0.05 N mm = 0.002 N in. ....	41
Fig. 16c Contour map of V displacement. Test 1, frame 12. V = 0.05 N mm = 0.002 N in. ....	42
Fig. 16d Contour map of U displacement. Test 1, frame 12. U = 0.01 N mm = 0.0004 N in. ....	43
Fig. 16e Contour map of strain $\epsilon_y$ . Test 1, frame 12. $\epsilon_y =$ 0.05 N. ....	44
Fig. 16f Contour map of strain $\epsilon_y$ . Test 1, frame 12. $\epsilon_y =$ 0.05 N. ....	45
Fig. 16g Contour map of strain $\epsilon_x$ . Test 1, frame 12. $\epsilon_x =$ 0.02 N. ....	46
Fig. 16h Contour map of strain $\gamma_{xy}$ . Test 1, frame 12. $\gamma_{xy} =$ 0.04 N. ....	47
Fig. 17a V-displacement fields for maximum crack opening prior to crack growth .....	51
Fig. 17b $\epsilon_y$ fields for maximum crack opening prior to crack growth .....	52
Fig. 18 Displacement V and strain $\epsilon_y$ accumulated during sequential one second intervals during crack opening phase. Specimen 7; 0.6 in. (15 mm) thick; 1.0 in. (25 mm) per min loading rate .....	54
Fig. 19 The rol of $(V)_0$ in Equation 1 .....	59
Fig. 20 Data plot for determination of $\lambda_u$ for inert propellant	60
Fig. 21 $\lambda_\sigma$ distribution for inert propellant .....	63



## LIST OF TABLES

	<u>Page</u>
Table 1: Mechanical Properties of Polyurethane .....	3
Table 2: Test Conditions .....	24
Table 3: Blunt Tip Height .....	34
Table 4: Test Data for $\lambda$ Determination .....	61
Table 5: Test Data for $\lambda$ Measurements .....	61

## INTRODUCTION

➤ When cracks occur in rocket motor grains, they may significantly alter the subsequent motor performance. Consequently as performance requirements are advanced, it becomes critical to incorporate fracture control concepts into the evaluation of the structural integrity of motor grains. While most such concepts are typically based upon two dimensional analysis, the motor geometry and conditions of use suggest the presence of significant three dimensional effects. Over the past decade, attempts have been made to develop mathematical models for predicting fracture behavior in rocket motors but model validation has been inhibited by lack of an extensive data base for validating three dimensional effects. Moreover, certain such effects have only recently been identified, and have not been evaluated for rocket propellant.

In particular, the near tip behavior of cracks in solid propellant material during opening and extension of the crack needs to be quantified experimentally. ←

### Program Objectives

The objectives of the present program were:

1) To measure the components of the displacement field on the specimen surfaces around the crack tip at time intervals at constant head rate extension during the opening and extension of the crack in "biaxial" specimens of inert propellant and extract surface strain fields from the data.

11) To determine the dominant singularity order for the crack at the specimen surface in the inert propellant and infer its distribution through the specimen thickness from frozen stress measurements.

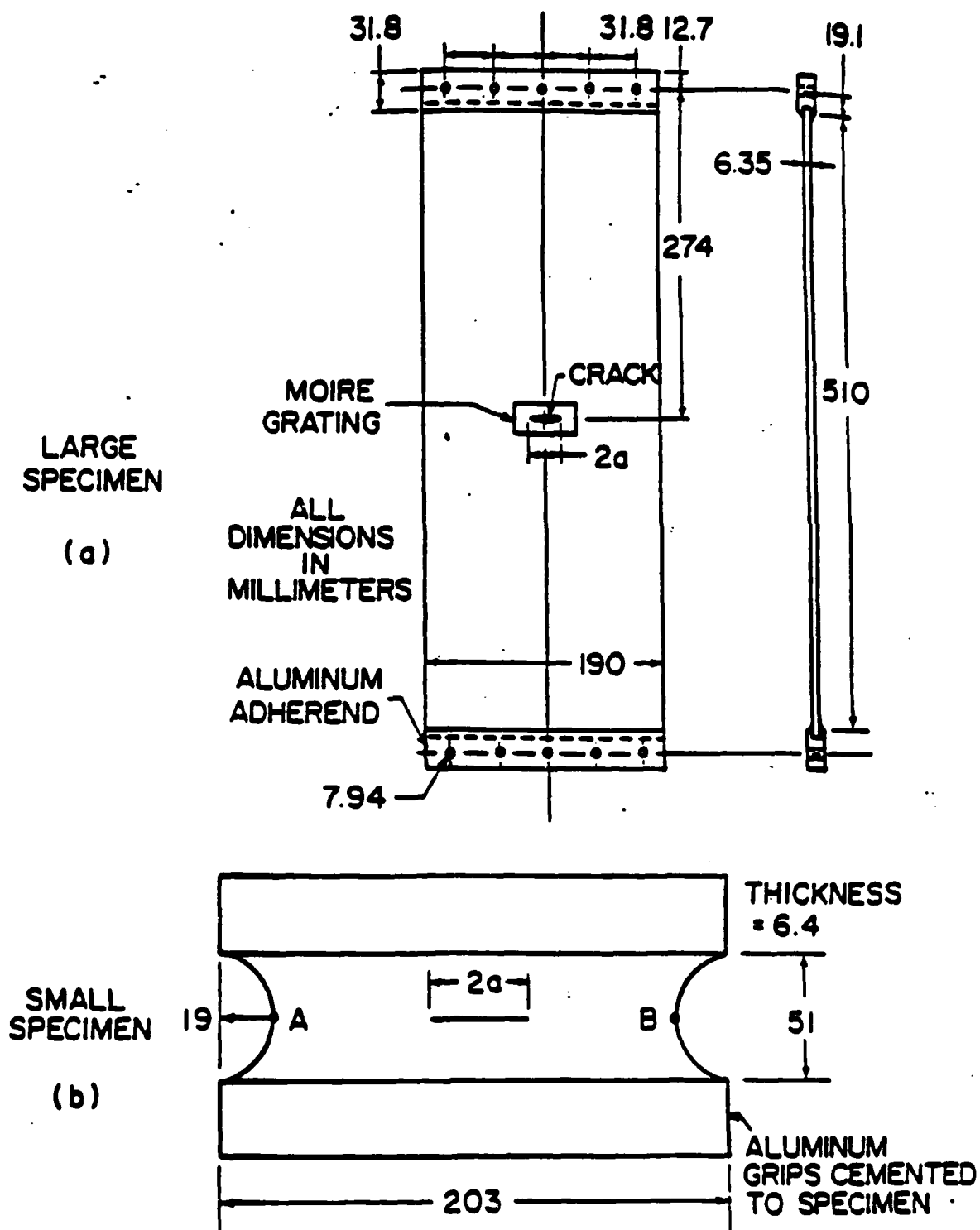
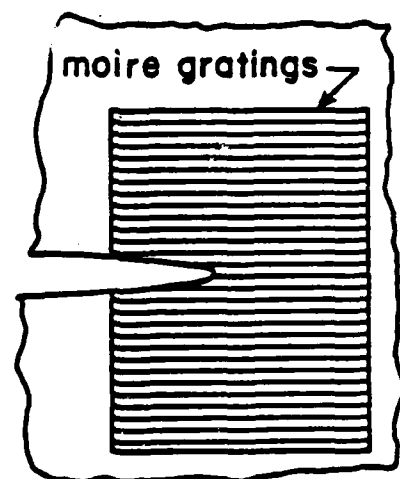
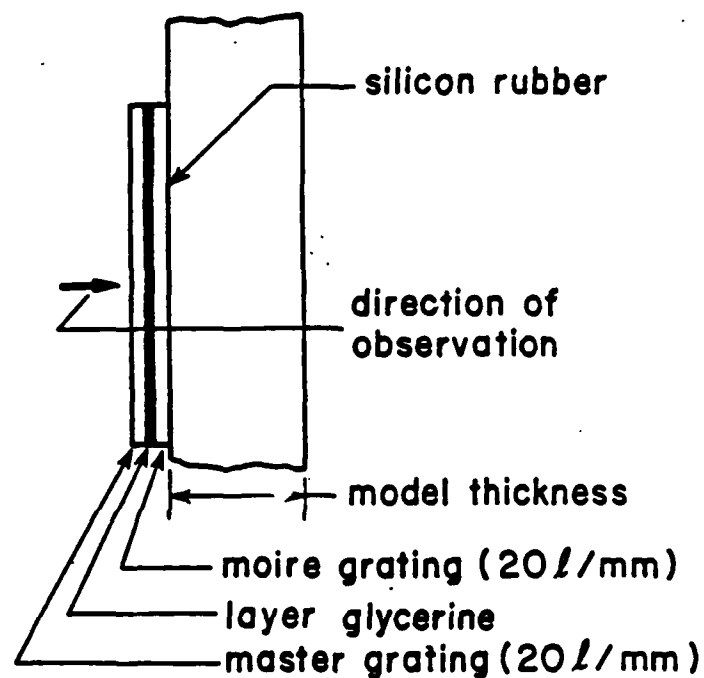


Fig. 1 Plan View of Large and Small Specimen Configurations for Polyurethane.



Plan View  
Showing Crack Tip



Edge View

Fig. 2 Test Setup for Moiré Displacement Measurements on Polyurethane Specimens.

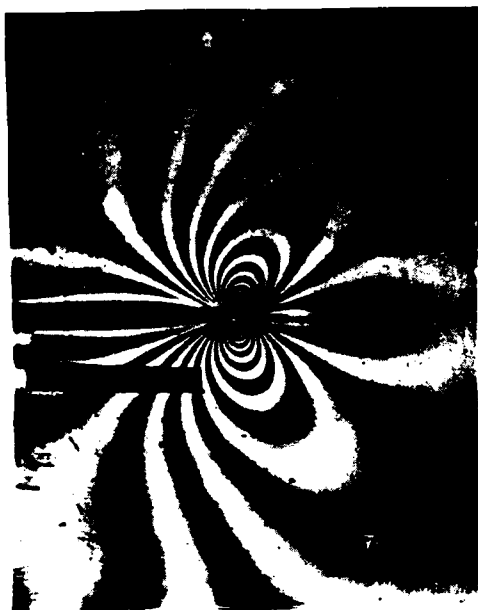
- v) Compare the the thickness averaged results with numerical solutions from LEFM and surface values of  $\lambda_U$  with analytical results.

The entire test procedure described above was first applied to the large specimens. However, since the primary interest here was focused on the small specimens, we shall report only results from the large specimens and then present details in conjunction with the discussion of the test results from the small specimen tests.

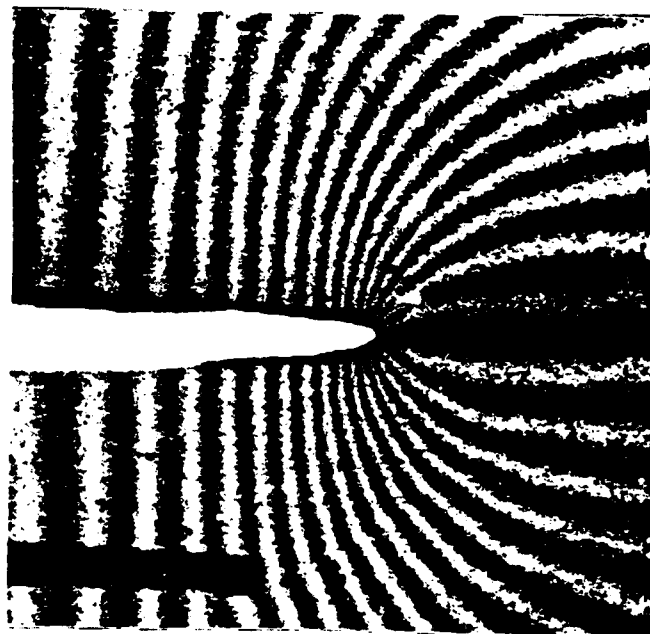
From the through thickness photoelastic tests, stress intensity values obtained from the LEFM method of analysis described in Appendix B agreed closely with numerical results reported in Ref. [5] for large plates with through cracks, thus confirming that  $\lambda_\sigma = |1 - \lambda_U| \approx 1/2$  for the through thickness data. From the moire analysis at global strain levels ranging up to 1%, the value of  $\lambda_U$  (Eq. B9 Appendix B) at the free surface was found to be  $= 0.65 \pm .02$ , agreeing reasonably well with Benthem's result of 0.67. Only data prior to crack growth were used in these determinations. Crack growth began at a global strain level of about 1.5% after which  $\lambda_U$  values decreased.

Typical near tip through thickness photoelastic and free surface moire patterns are shown in Figs. 3a and 3b respectively for a small specimen. Analysis of digitized photoelastic data from several global strain levels on the small specimen using LEFM from which the thickness averaged SIF is obtained using the data zone which agrees with numerical LEFM results revealed a constricted local data zone.

Figure 4 illustrates how  $\lambda_U$  is determined from the moire data using the displacement algorithm described in Eq. B9, Appendix B. Tests were run over a global strain level range of 2.0 to 2.8% without crack growth.



a) Dark Field  
 $\epsilon = 3.5\%$   
 M.F. = 1.85



b)  $\epsilon = 4.4\%$   
 M.F. = 5.7

Fig. 3 Typical (a) Photoelastic and (b) Moire Near Tip Fringe Patterns  
for a Small Polyurethane Model.

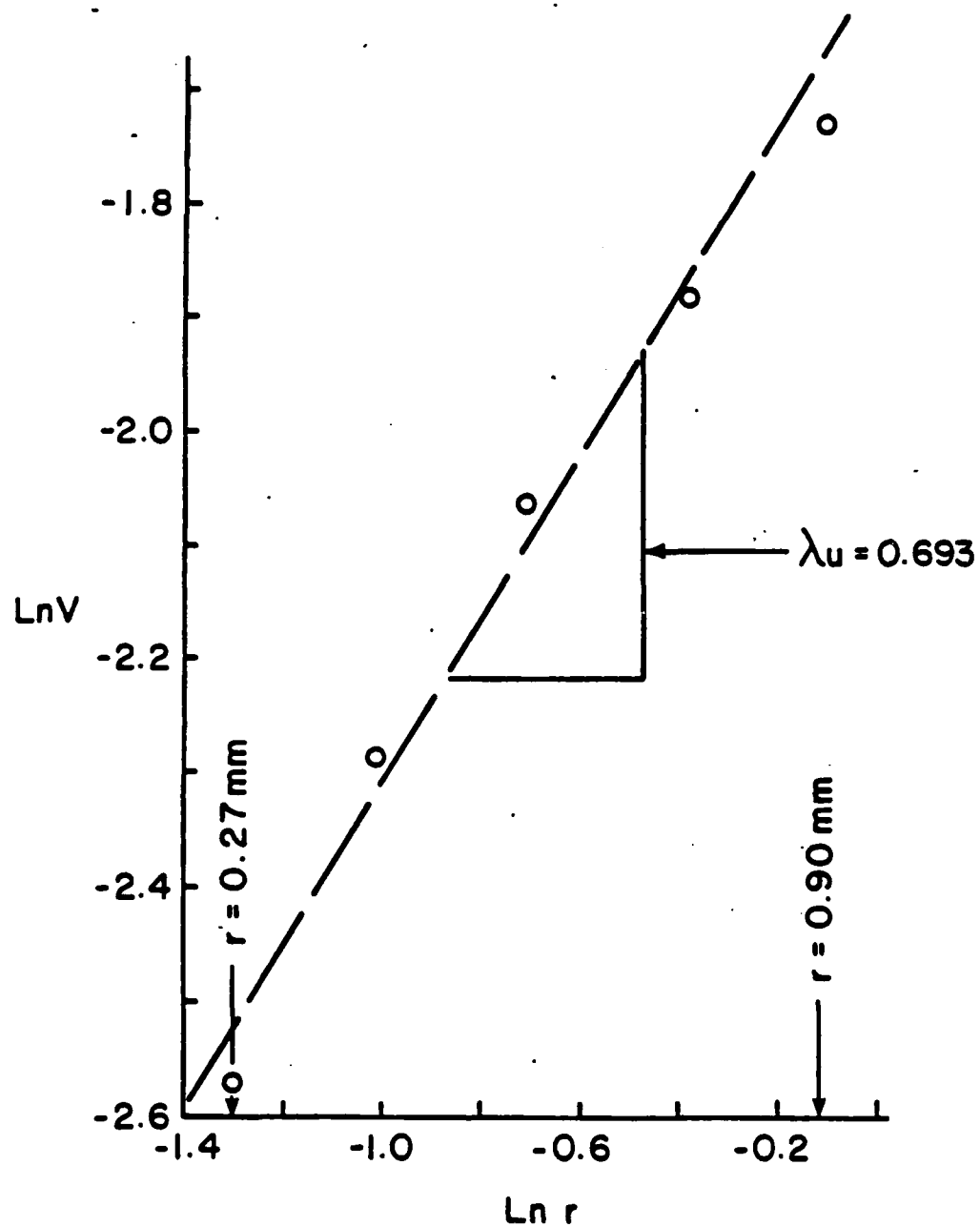


Fig. 4 Determination of  $\lambda_u$  from Moire Data for a Small Polyurethane Specimen.

The moire data yielded  $(\lambda_U)_{AVG} = 0.65$  which again agrees well with Benthem's result.

It is important to note that the data zone dominated by the lowest eigenvalue was found to be severely constricted in the small specimen. For example, in the large specimens, the moire data zone extended from 0.60 to 3.5 mm from the crack tip along  $\theta = \pi/2$ . However, in the small specimen with constant displacement loading, the zone was constricted to approximately 0.2 to 0.9 mm from the crack tip (along  $\theta = \pi/2$ ). A similar, though less severe, contraction occurred in the photoelastic data.

Several additional tests were conducted in order to obtain preliminary findings on other effects. As a result of these additional tests, the following observations are made:

- i) Increasing model thicknesses from 6.4 mm to 12.7 mm did not alter values of  $\lambda_U$  of the large models.
- ii) Measurements on grown cracks suggested the presence of some crack front curvature as shown in Fig. 5.
- iii) Crack tip profiles retained a nearly elliptic shape as shown in Fig. 3b and revealed no macroscopic evidence of crazing in either the opened crack without growth or grown cracks.

The above results suggest that:

- i) The zone dominated by the lowest eigenvalue is severely constricted in the small biaxial specimen.





← Crack front after growth

← — Initial crack front

← — Center of initial crack

Fig. 5 Crack Front Curvature of Growing Crack.

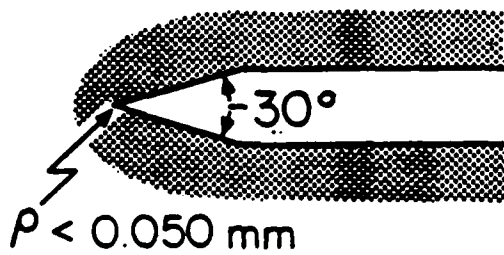
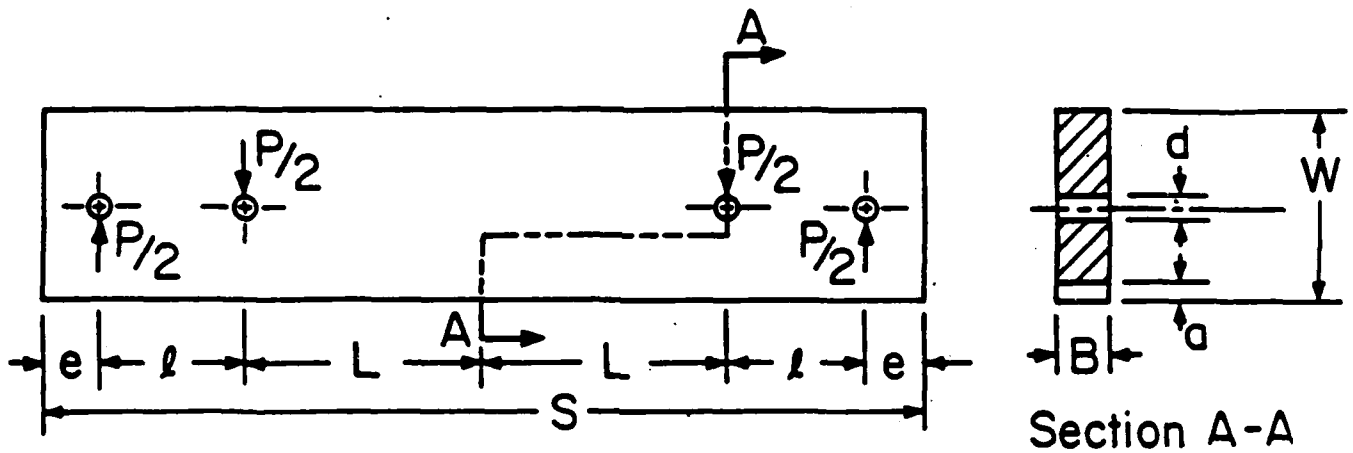
ii) The influence of the free surface on singularity order when using thickness averaged data is negligible.

iii) In nearly incompressible materials such as polyurethane, the above noted effect is quite strong, as predicted analytically by Benthem when surface measurements are made.

#### Singularity Order Distribution

In addition to the measurement of the singularity order at the free surface, it was desired to estimate the singularity order distribution through the specimen thickness. Having previously established that the body geometry, if sufficiently thick, did not alter the value of the dominant singularity at the free surface [2], one might expect that the distribution of the dominant eigenvalue through the same thickness of body might also be unaffected by body geometry at least for straight front cracks. Following this line of reasoning, a frozen stress photo-elastic analysis of a compact bending specimen was conducted in order to estimate the distribution of the dominant stress eigenvalue  $\lambda_\sigma$  across the specimen thickness ( $\lambda_\sigma = |\lambda_U - 1|$ ).

A compact bending model consisting of the geometry pictured in Fig. 6 was cut from a plate of stress free transparent stress freezing material. A straight front artificial crack was machined into the model and it was subjected to a stress freezing cycle under four point bending. Subsequent to load removal at room temperature, thin slices mutually orthogonal to the crack surface and the crack front were removed and analyzed utilizing both the Tardy and fringe multiplication analysis techniques.



$W = 25.70$  mm

$d = 6.35$  mm

$a = 12.82$  mm

$B = 13.33$  mm

$e = 12.7$  mm

$l = 50.8$  mm

$L = 76.2$  mm

$S = 279.4$  mm

$P = 2.32$  N

Fig. 6 Compact Bending Specimen Used in Stress Freezing Work.

Raw data from a single slice are shown in Fig. 7. Algorithms for converting photoelastic data into fracture parameters are discussed in Appendices B and C. By fitting Eq. B4 to this data, the slope of the linear part of the curve, or  $\sigma^0$  can be determined. This, in effect determines  $\tau_0$  (Eq. C7) for the case where  $\lambda_g = 1/2$  for each slice. For slices near the boundary, computed  $\tau_0$  values begin to decrease. Beginning at this location from the free surface, we arbitrarily impose a linear decrease on the computed value of  $\tau_0$  down to zero at the free surface. By imposing this condition, our resulting value of  $\lambda_g$ , measured from a plot of Eq. C9 agrees with both Benthem's results and those obtained from a moire interferometric analysis at the free surface [2]. A log-log plot of  $\tau_{\max} - \tau_0$  vs.  $r$  for one slice near the center of the beam is shown in Fig. 8.

Figure 9 shows the values of  $\lambda_g$  across the thickness of a compact bending specimen as obtained from two separate tests using the above procedure. This plot reveals the thickness of the boundary layer through which  $\lambda_g$  varies for an incompressible homogeneous material.

#### Inert Propellant Tests: Deformation Measurement, Methods and Results

##### Specimen and Loading

The specimen geometry is illustrated in Fig. 1b. The same dimensions were used, except the inert propellant specimens were approximately 0.2 in. (5 mm) and 0.6 in. (15 mm) thick. The artificial cracks were  $2a = 38$  mm long, made by pressing a specially prepared razor blade through the specimen thickness; the blade was modified by grinding its short edges to form sharp cutting edges.

The specimen material is manufactured by Morton Thiokol, Inc., under the trade name H-24 Inert Propellant. The principal ingredients

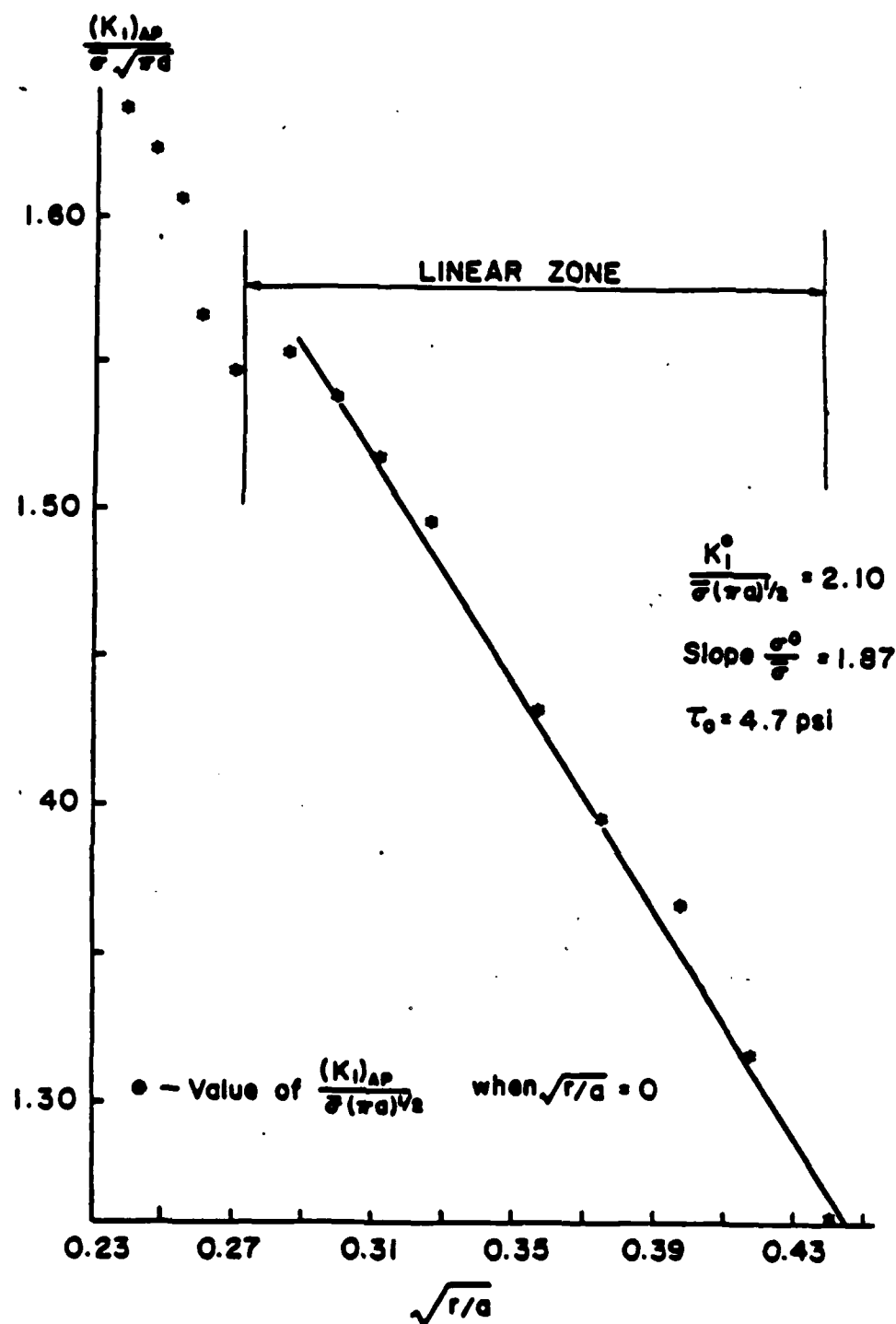


Fig. 7 Determination of  $\sigma^0/\sigma$  from Raw Photoelastic Data from a Single STIc.

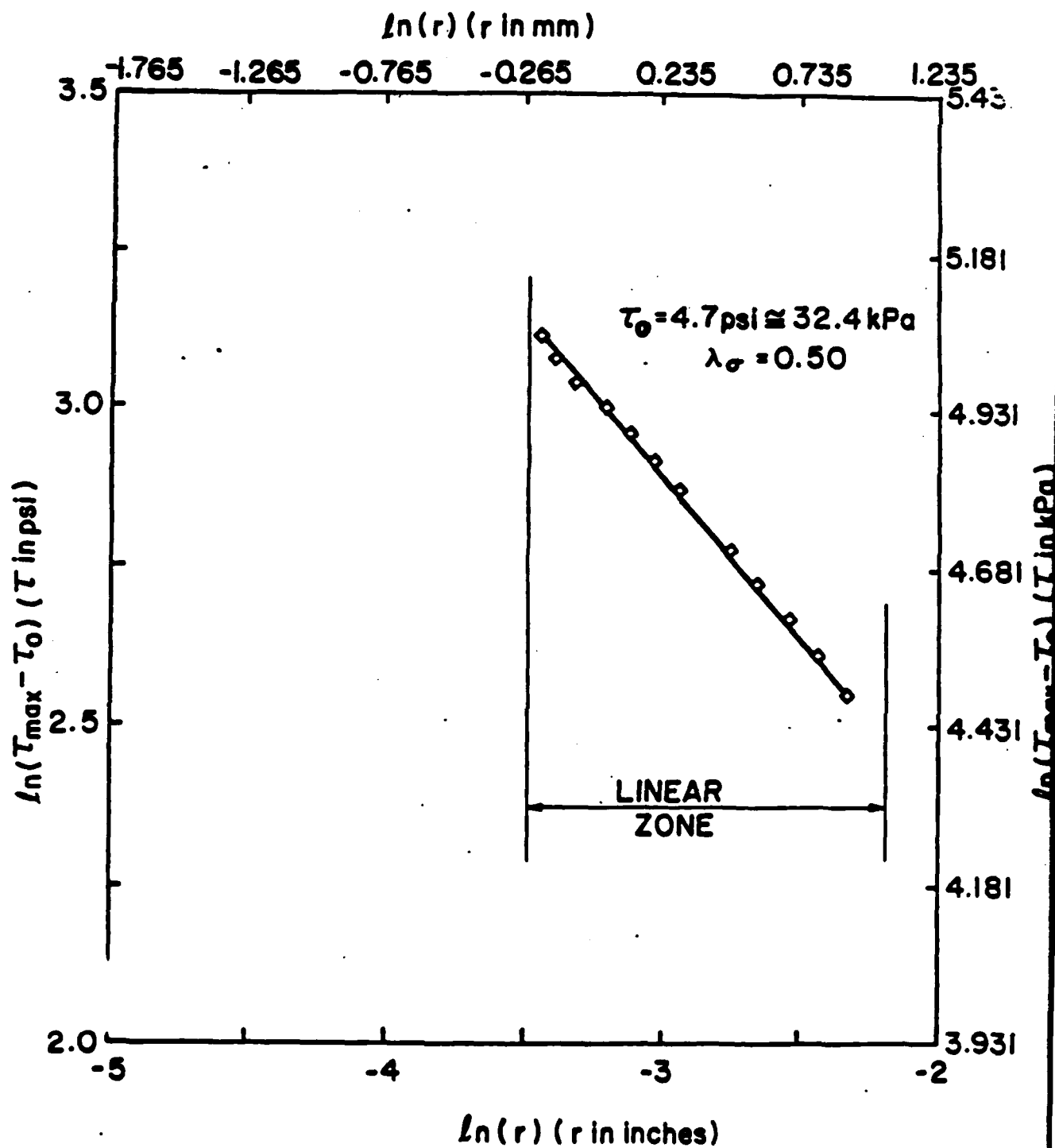


Fig. 8 Determination of  $\lambda_\sigma$  from Test Data.

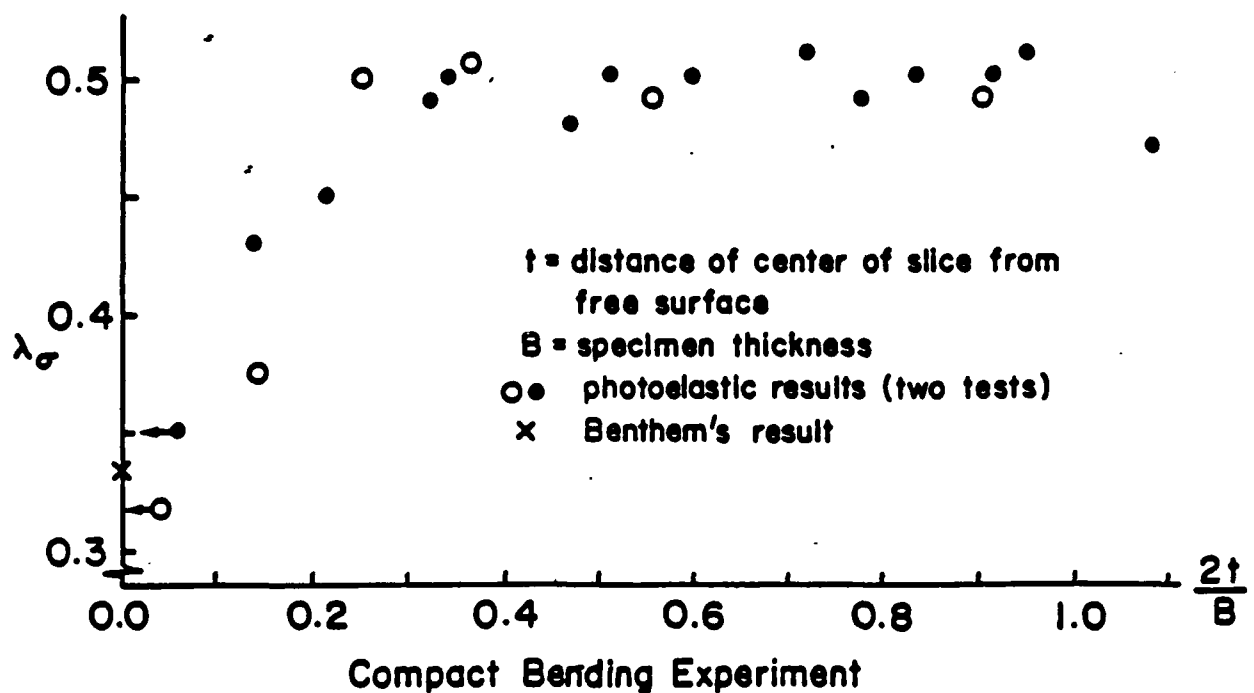


Fig. 9 Distribution of  $\lambda_\sigma$  Across the Half Thickness of a Compact Bending Specimen.

are:

polybutadiene resin	10% by weight
potassium chloride	70%
powdered aluminum	15%
ammonium perchlorate	5%

It is a dark gray rubbery solid. It was supplied as 5 mm and 15 mm sheets, presumably cast to final thickness in smooth molds. One surface of each sheet was tacky (or sticky) and the other surface was not.

The material is a heterogeneous composite of very stiff inclusions in a compliant matrix of polybutadiene rubber. The volume fraction of inclusions is approximately 75%. The principal inclusion, potassium chloride, is a salt with essentially cubical shaped grains of widths said to range between 10 and 200  $\mu\text{m}$ ; in fact, grains as large as 500  $\mu\text{m}$  (0.5 mm) were found, and a great abundance of 400  $\mu\text{m}$  grains were found

in the material. Many crystals of potassium chloride were broken and they exhibited irregular shapes instead of cubes. The secondary inclusions were small compared to the potassium chloride.

The specimens were cemented into relatively rigid aluminum grips (Fig. 1b) and installed in a tensile testing machine. The installation assured parallel translation of the grips (i.e., no rotation of the grips). Various constant cross-head speeds, or grip separation rates, were used from 0.01 to 1.0 inches (0.25 to 25 mm) per minute. A typical graph of load vs. grip extension is shown in Fig. 10. The maximum load was reached before visible crack extension occurred, and the load continued to decrease with crack growth. Since cross-head speed is constant for each test, the graph also represents load vs. time.

#### Displacement Measurements, Methods

The grid method was used for in-plane displacement measurements  $U$  and  $V$ . The shadow moiré method was used simultaneously on the back surface of the specimen to measure out-of-plane displacements  $W$ . Rationale for selecting these methods in preference to other experimental techniques is given in Appendix D. Details of the grid method, as applied here, are given in Appendix E, which includes methods for applying the grid to the specimen. Details of the shadow moiré method are given in Appendix F.

A separate method was developed and demonstrated for acquiring  $U$ ,  $V$  and  $W$  displacements simultaneously from the same zone of observation, i.e., from one side of the specimen. This is described in Appendix G. It utilizes the grid method for  $U$  and  $V$  and two-beam coherent projection moiré for  $W$ . The data are collected by a single photograph from which



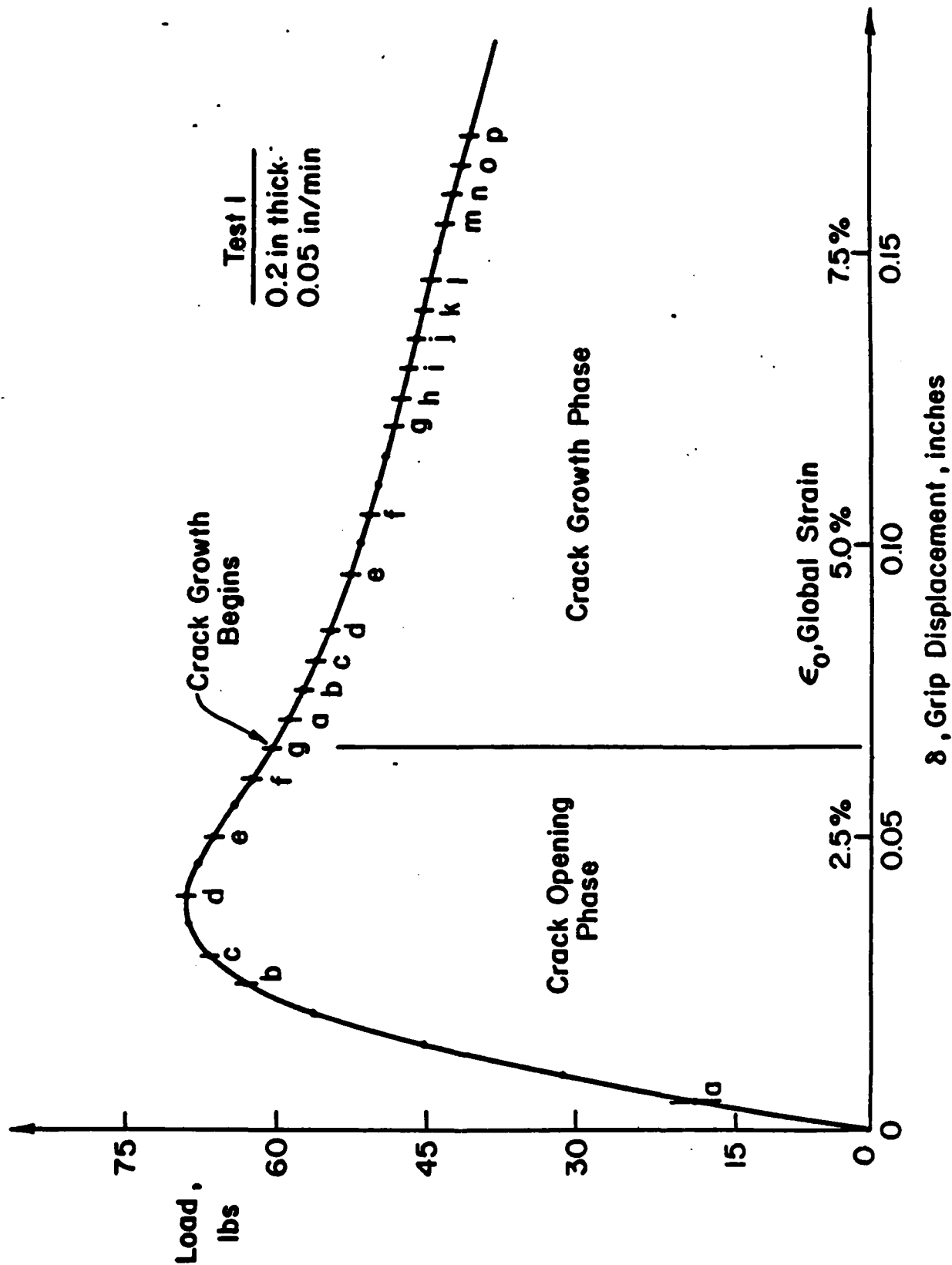


Fig. 10 Load vs. grip displacement for Test 1. To convert to metric  
1 in. = 25 mm; 1 lb. = 4.45 N.

the grid lines can be digitized and the W displacement field extracted by an optical filtering process.

#### Utility of W Measurements

The algorithms used to determine fracture parameters in this work require V, alone, and not W. A question can be raised, however, equivalent to that for assessing the magnitudes of finite strains: to what extent do out-of-plane rotations influence the change of length, or relative displacement of end points, of a line segment? If W is insignificant in the calculation of in-plane strains, the influence of W on the fracture algorithm is negligible.

That is the condition realized in these tests. The influence of W on  $\epsilon_y$ , for example, is given by the Lagrangian large strain relationship

$$\epsilon_y^L = \sqrt{1 + 2 \frac{\partial V}{\partial y} + \left(\frac{\partial U}{\partial y}\right)^2 + \left(\frac{\partial V}{\partial y}\right)^2 + \left(\frac{\partial W}{\partial y}\right)^2} - 1 \quad (1)$$

where L signifies the Lagrangian formulation. Data extracted from the W-displacement fields, e.g., from Fig. 11 or 12, discussed in subsequent sections, assures that  $(\partial W/\partial y)^2$  is negligible in comparison to  $2\partial V/\partial y$ .

This independence of W was observed from preliminary tests. Accordingly, the utility of W measurements was subordinated to qualitative observation of its distribution during the crack opening and crack growth phases. The qualitative character could be assessed from the back side of the specimen as well as the front. This removed the requirement for observing U, V and W at the same location; it allowed an easier test procedure in which the grid method and shadow moire method could be set up independently of each other on front and back surfaces, respectively.

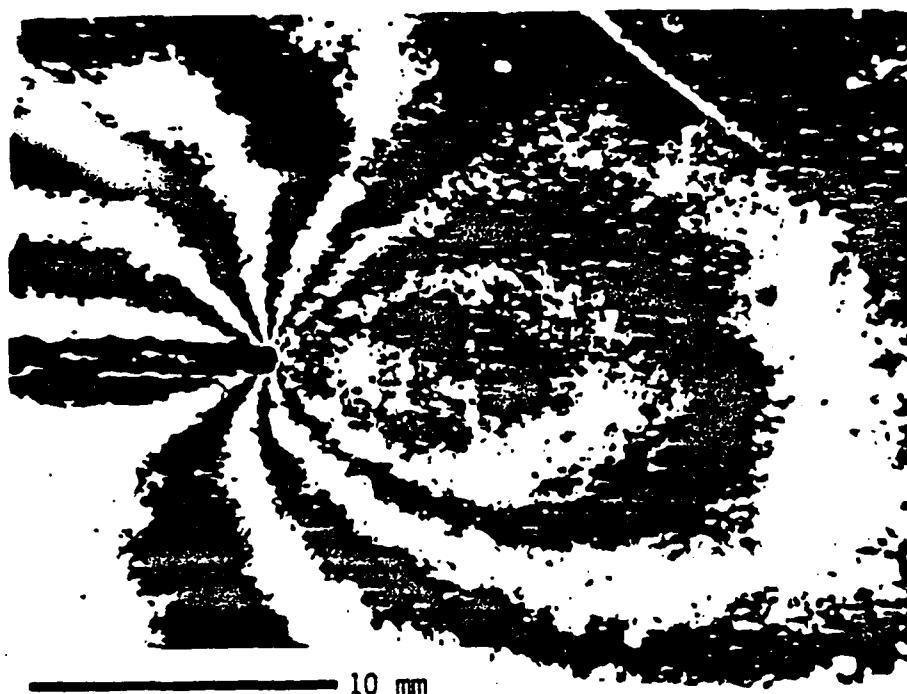


Fig. 11 Shadow moiré pattern of W field. Test 8; 0.6 in. (15 mm) thick specimen; 1.0 in. (25 mm) per min loading rate; maximum crack opening prior to crack growth; sensitivity 0.002 in. (0.05 mm) per fringe order.



Fig. 12 Projection moiré pattern of W field. 0.6 in. (15 mm) thick specimen; crack growth phase; sensitivity 0.0011 in. (0.028 mm) per fringe order.

For problems where the influence of  $W$  is significant, the method described in Appendix G could be used.

#### Test Conditions

Numerous preliminary tests were conducted to establish the experimental techniques. Subsequently, data were extracted from tests outlined in Table 2. Test No. 4 was conducted but it was not successful.

The tests were conducted at room temperature, approximately 72°F. The specimen material was stored in its original moisture-proof wrappings. It was exposed to the environment while the specimen was cut to shape, while the grid was being applied, while it was being set up for testing and while it was being tested -- in all, for a period of 4 to 8 hours. Between steps in this process it was protected again in moisture-proof wrappings. This procedure was used for each specimen except No. 1, which was exposed to the environment for a longer time.

#### Results: Representative Raw Data

A sequence of photographs of the crack and the 125 lines/inch (5 lines/mm) grid is given in Fig. 13 for Test No. 1. Figure 13a illustrates the crack opening phase, in which the width of the crack increases as the grip separation proceeds. Figure 13b illustrates the crack growth phase. For each photograph, the corresponding load, grip displacement and global strain is indicated in Fig. 10 by the same lower case letter as used in Fig. 13. Global strain  $\epsilon_0$  is defined as

$$\epsilon_0 = \left( \frac{\delta}{h_0} \right) 100\% \quad (2)$$

Table 2

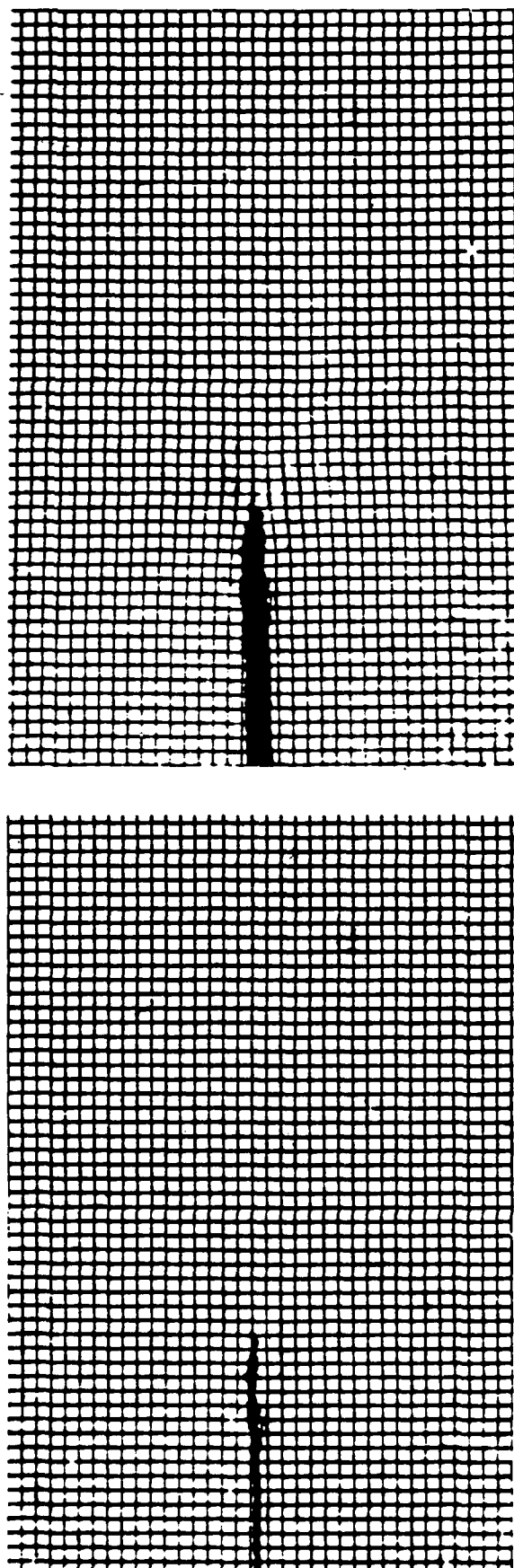
TEST CONDITIONS

Test No.	Date	Specimen Thickness inches	Cross-head Speed, in./min.	Grid Freq. (lines/in.)		Shadow Moire	Frame Nos. Digitized
				Tacky Side	Grid Material Non-tacky Side		
1	6/30/86	0.2	0.045	125/Alum.*	-	No	0,4,6,7,12
2	9/12/86	0.2	0.07	125/Alum	-	Yes	0,20,23
3	9/30/86	0.6	0.10	125/Alum	-	Yes	0,10
5	12/15/86	0.6	0.10	125/T10**	-	Yes	1,7,8
6	12/29/86	0.6	0.10	500/T10	125/T10	No	0,5,9
7	1/13/87	0.6	1.0	-	125/T10	Yes	0,1,2,3,4,5,6,7,8
8	1/23/87	0.6	1.0	-	125/T10	Yes	0,3
9	2/18/87	0.6	0.01	125/Alum	500/Alum	No	--
10	3/26/87	0.2	1.0	-	125/T10	No	0,4,5,14

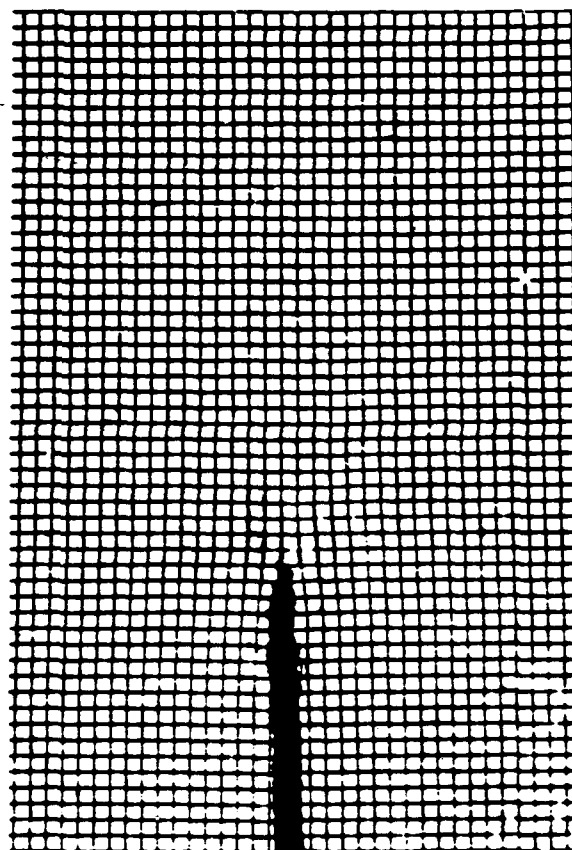
To convert to metric: 1 in. = 25.4 mm

\* Evaporated aluminum film

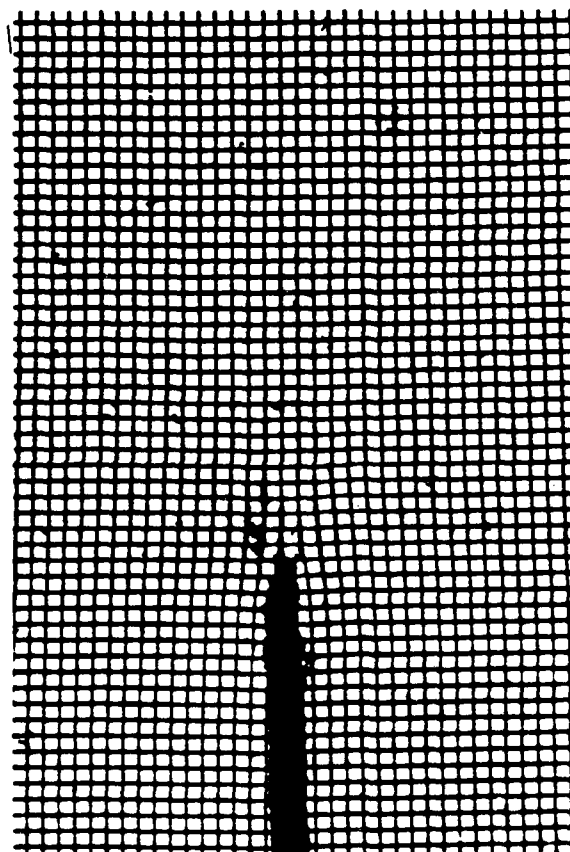
\*\* Titanium dioxide powder



(a)

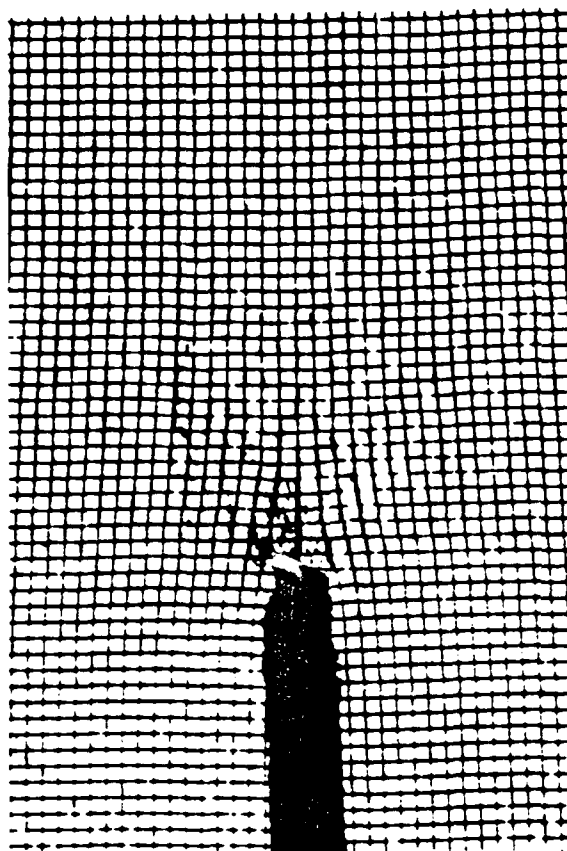


(b)

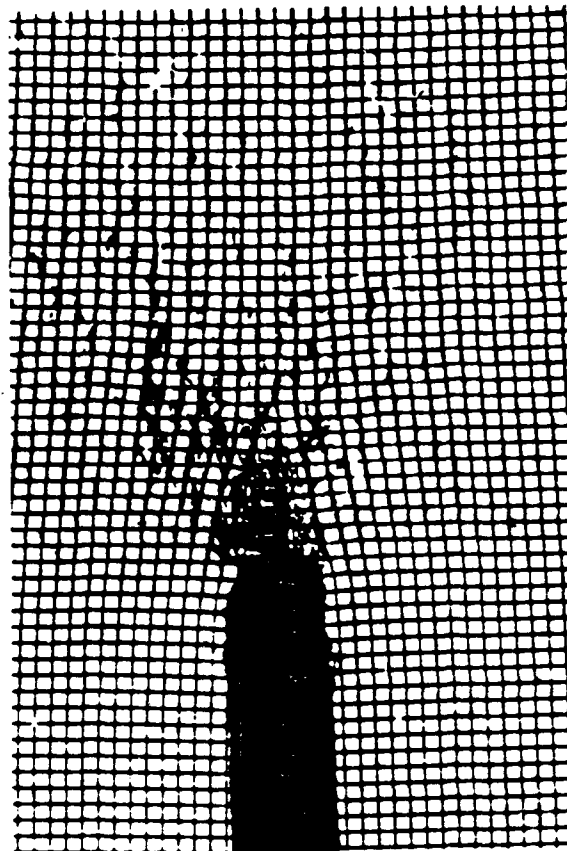


(c)

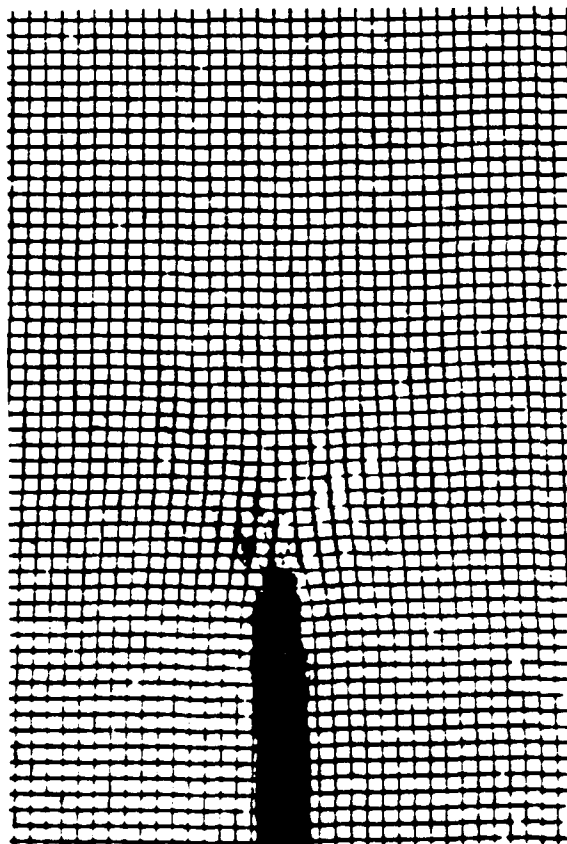
Fig. 13a Grid deformations during the crack blunting phase. Test 1; specimen thickness 0.2 in. (5 mm); cross-head speed 0.05 in. (1.3 mm)/min.



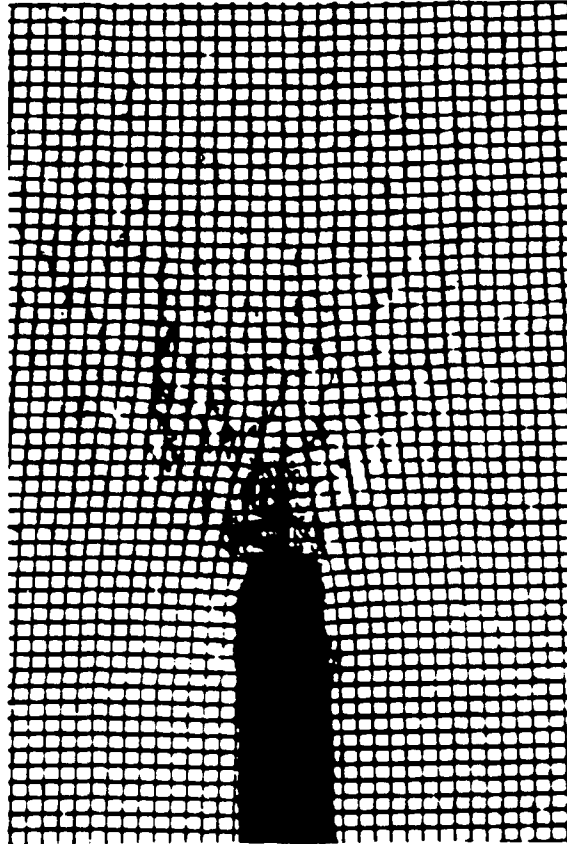
(e)



(g)



(d)



(f)

Fig. 13a cont. Grid deformations during the crack blunting phase.



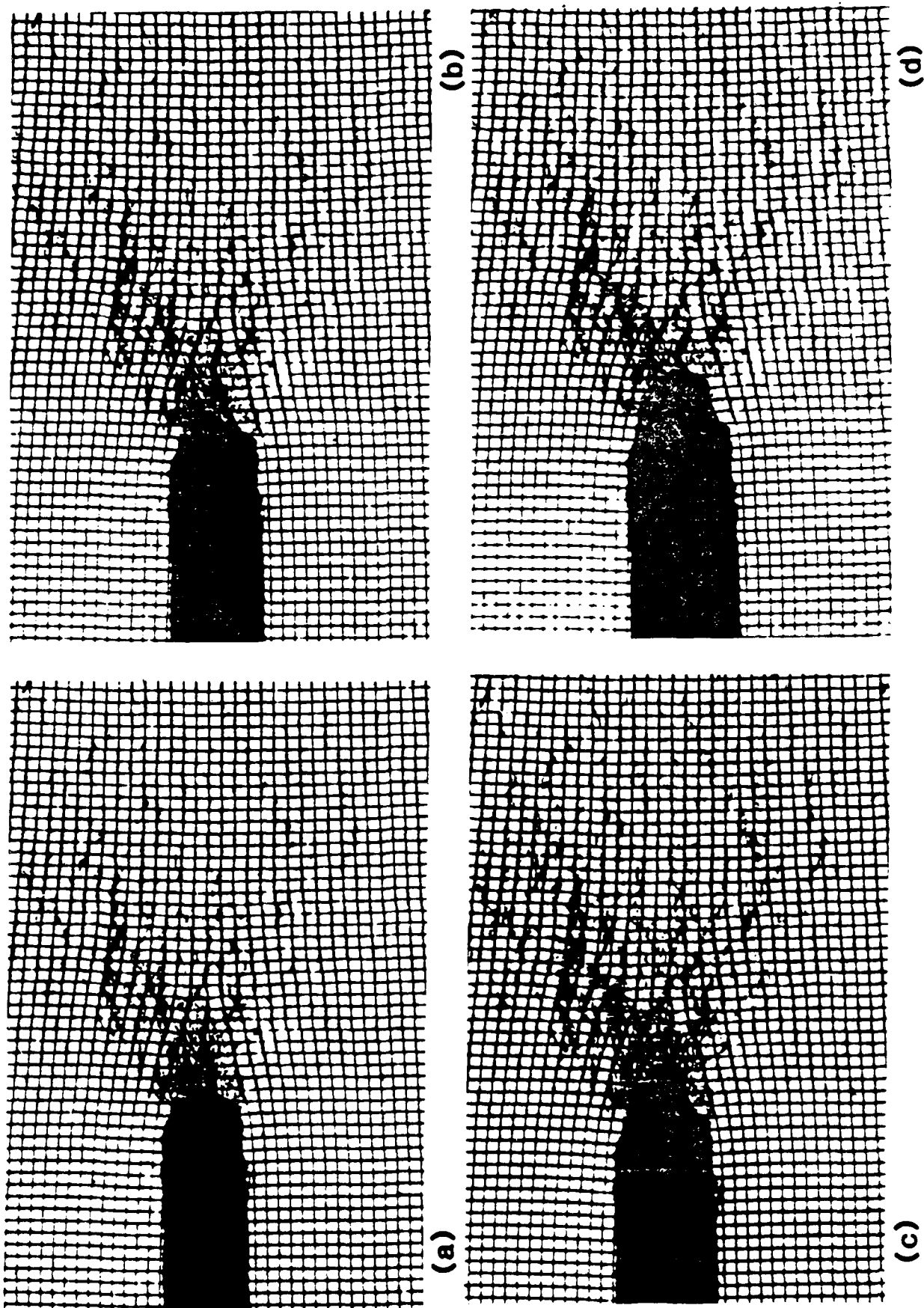
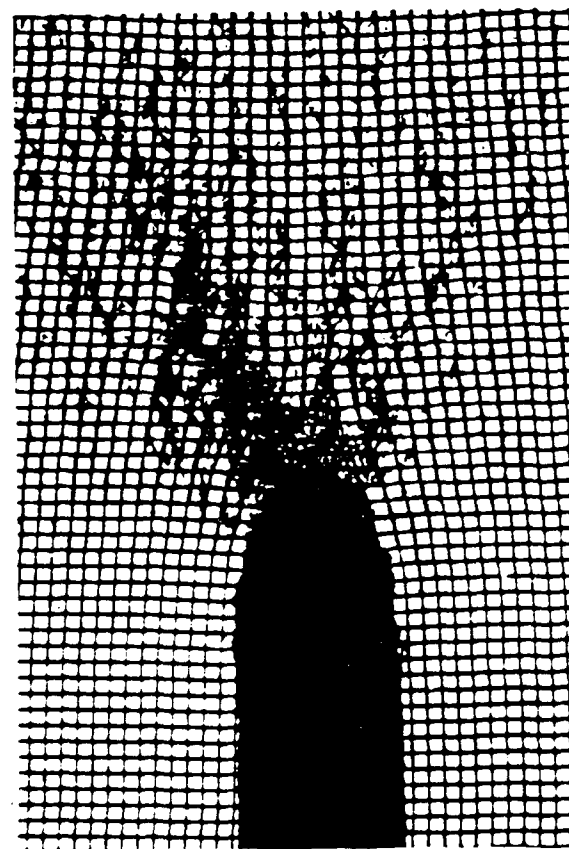
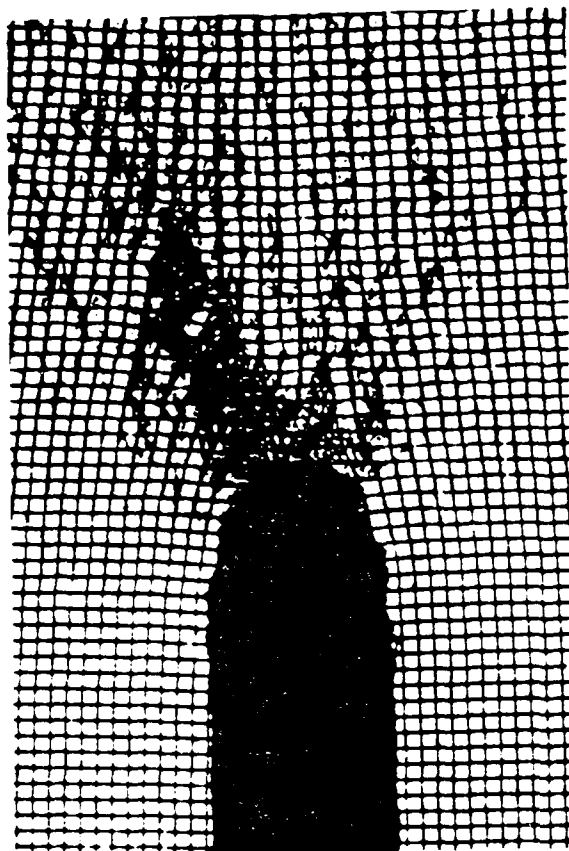


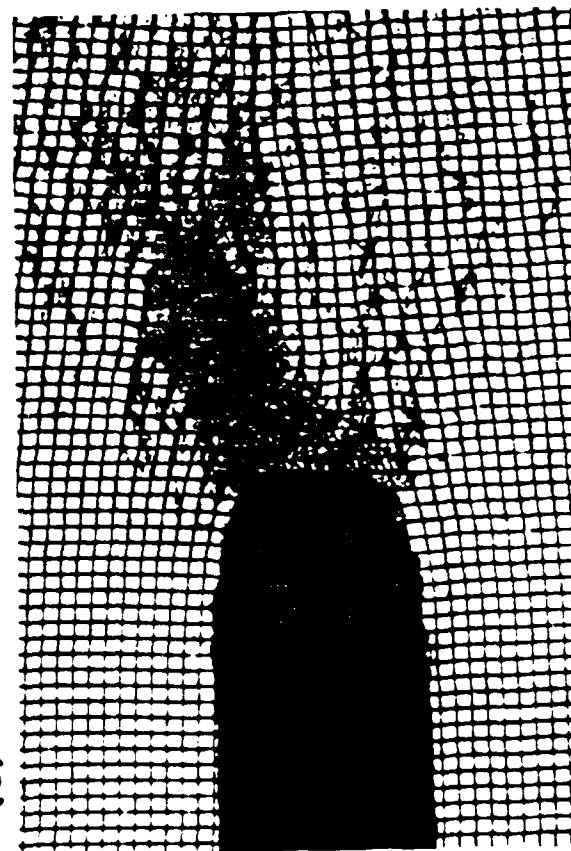
Fig. 13b Grid deformations during the crack growth phase.



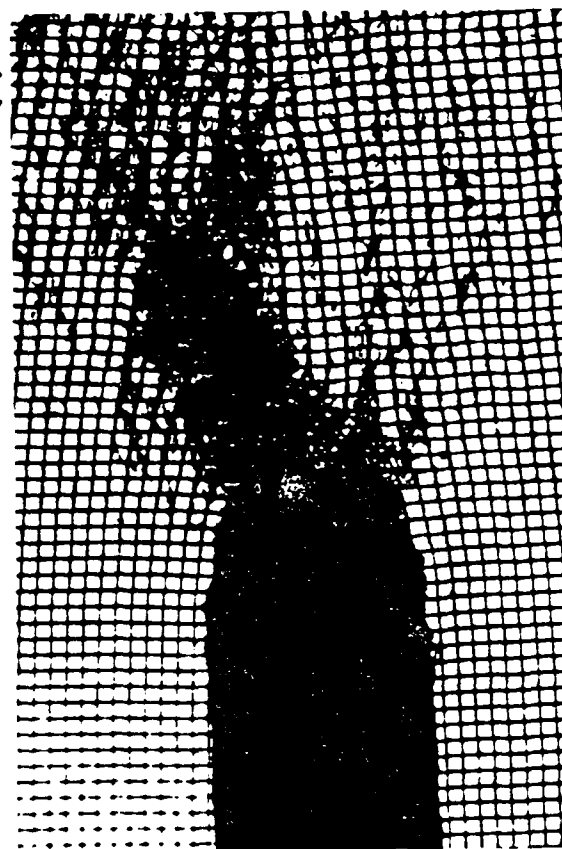
(e)



(f)



(g)



(h)

Fig. 13b cont. Grid deformations during the crack growth phase.

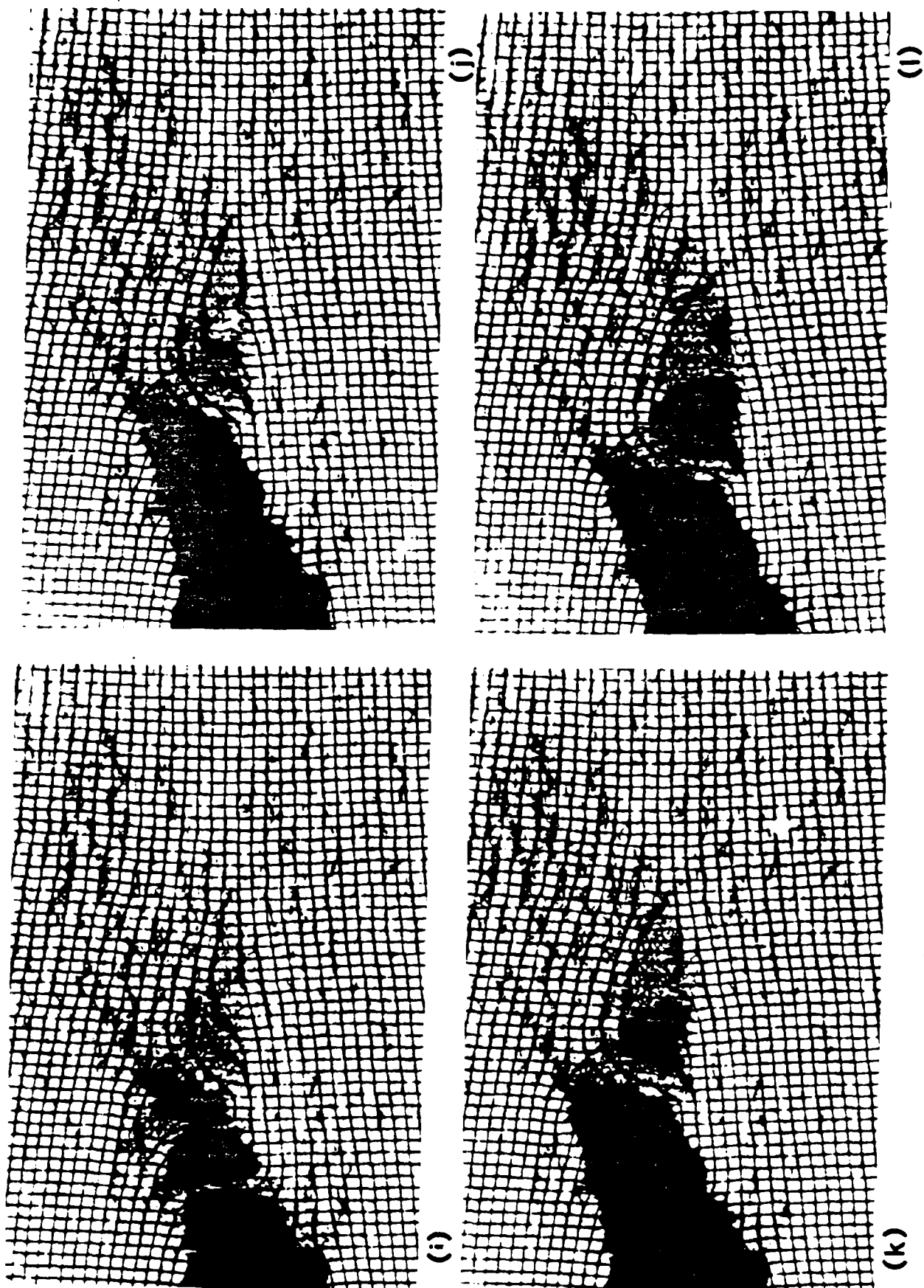
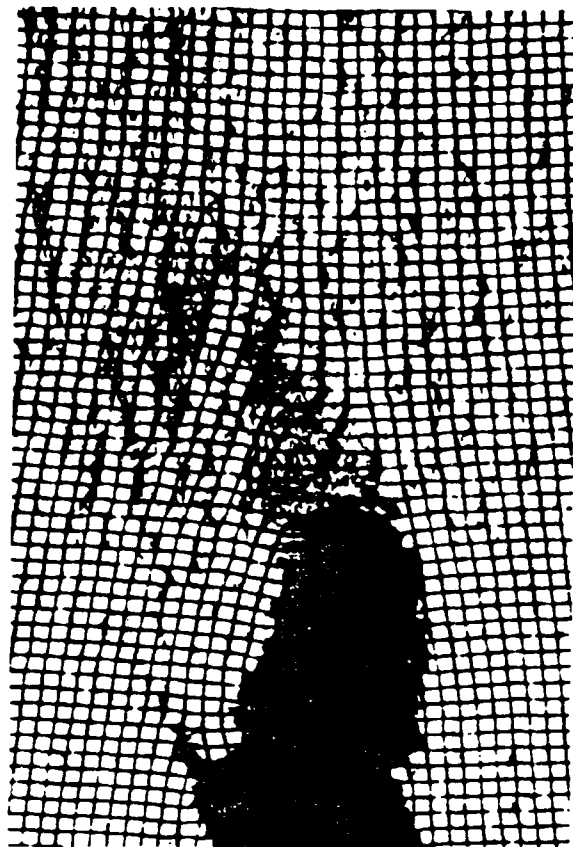
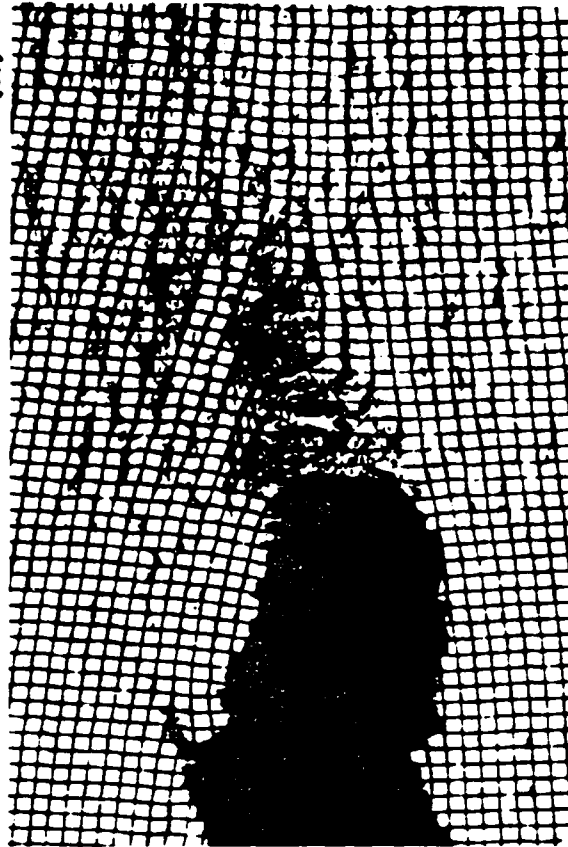


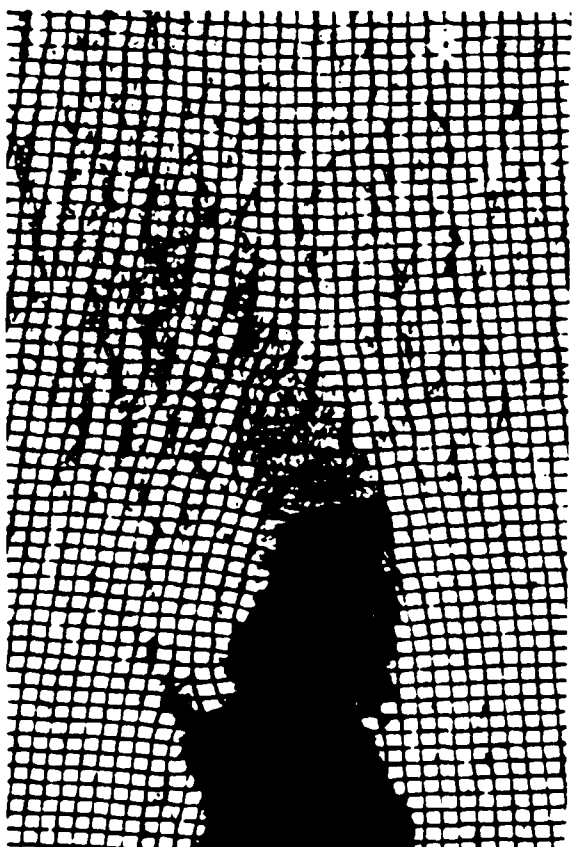
Fig. 13b cont. Grid deformations during teh crack growth phase.



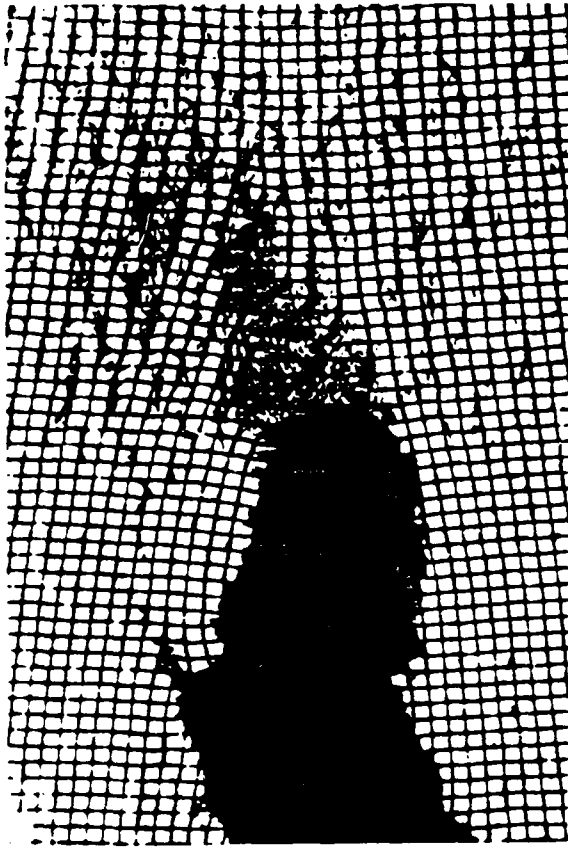
(n)



(p)



(m)



(o)

Fig. 13b cont. Grid deformations during the crack growth phase.

where  $\delta$  is the grip displacement and  $h_0$  is the initial height of the specimen.

A contour map of out-of-plane displacements  $W$  is illustrated by Fig. 11. This was taken in Test No. 8 with a 0.6 inch (15 mm) thick specimen and 1 inch/min (25 mm/min) loading rate. It shows the condition of maximum crack opening prior to crack extension. The contour interval, or sensitivity, is 0.002 inches (0.05 mm) per fringe order.

Figure 12 is a contour map of  $W$  obtained by the simultaneous  $U, V, W$  method, using a 0.6 inch (15 mm) thick specimen in the crack extension phase. The contour interval is 0.0012 inches (0.03 mm) per fringe order.

#### Results: Crack Blunting

Insight into the heterogeneous nature of the material and probabilistic character of its performance can be found in Fig. 14 and Table 3. Figure 14 shows the crack and the surrounding deformed grid for various test specimens at the maximum crack opening prior to crack growth. The degree of blunting is rather different in each case, different in a nonsystematic distribution. The cracks terminate with fairly straight blunted tips, essentially perpendicular to the crack length. The degree of blunting will be quantified here by the length of this straight portion, called blunt-tip height. While this length is not rigorously defined because the crack tips are slightly curved, it can be measured with suitable accuracy as the distance between boundary points where the radius of curvature of the boundary becomes small.

The blunt-tip height is given in Table 3. The three replicate specimens with 0.6 in. (15 mm) thickness and 0.1 in./min (2.5 mm/min)

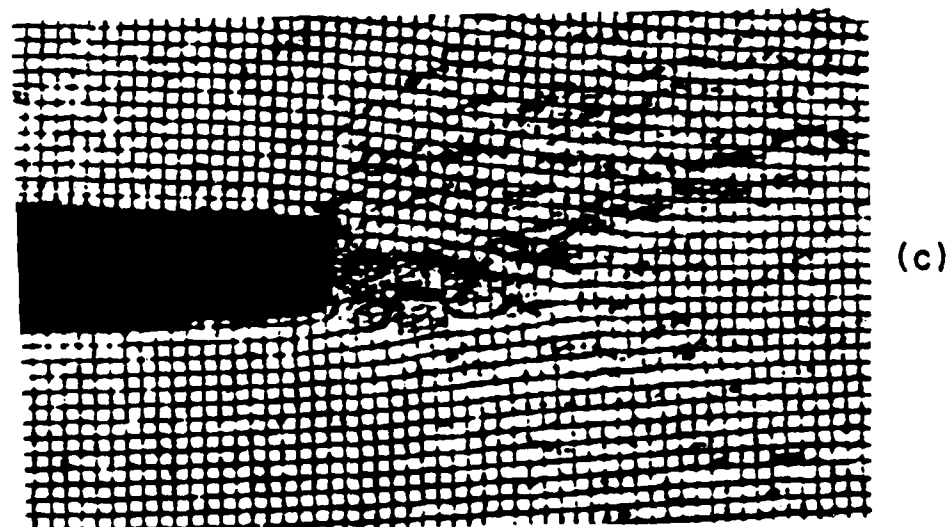
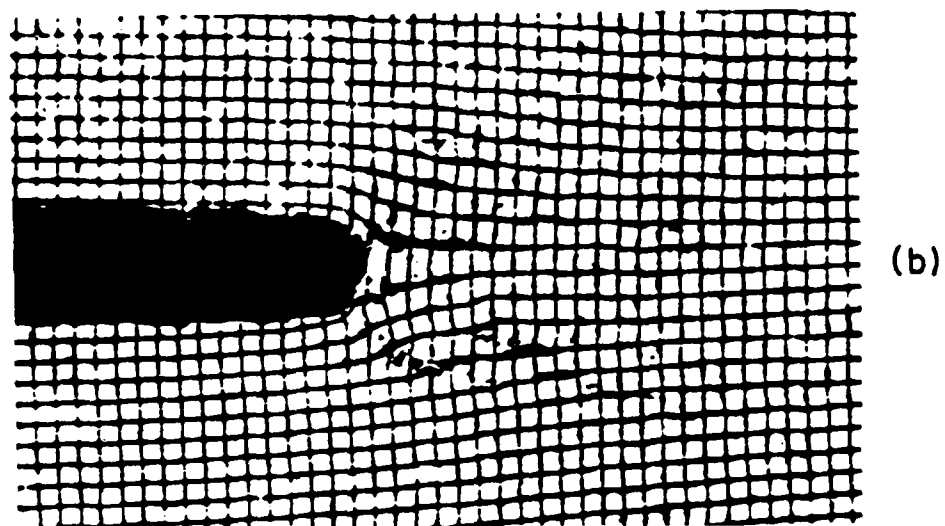
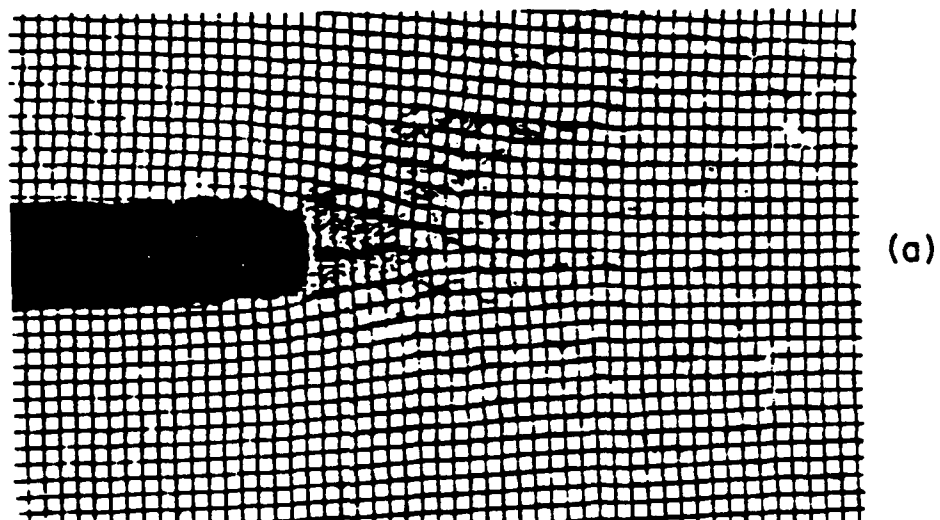
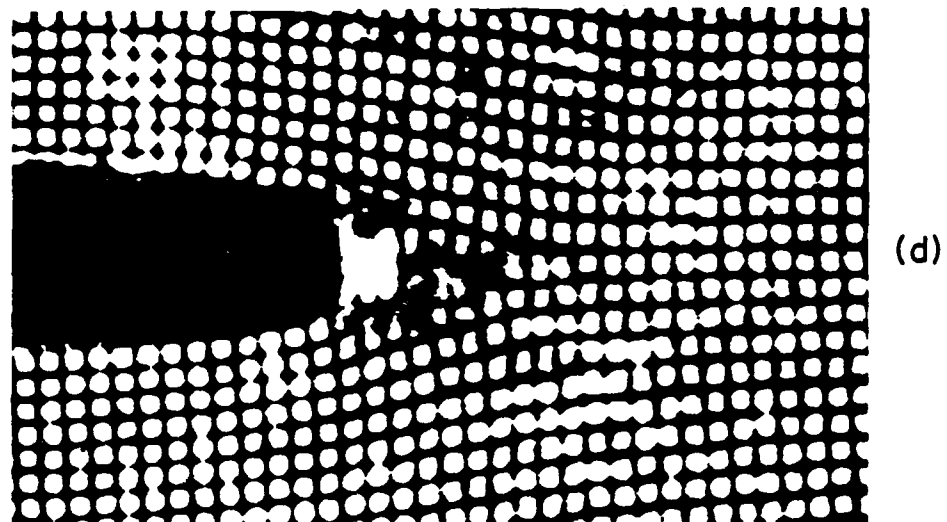
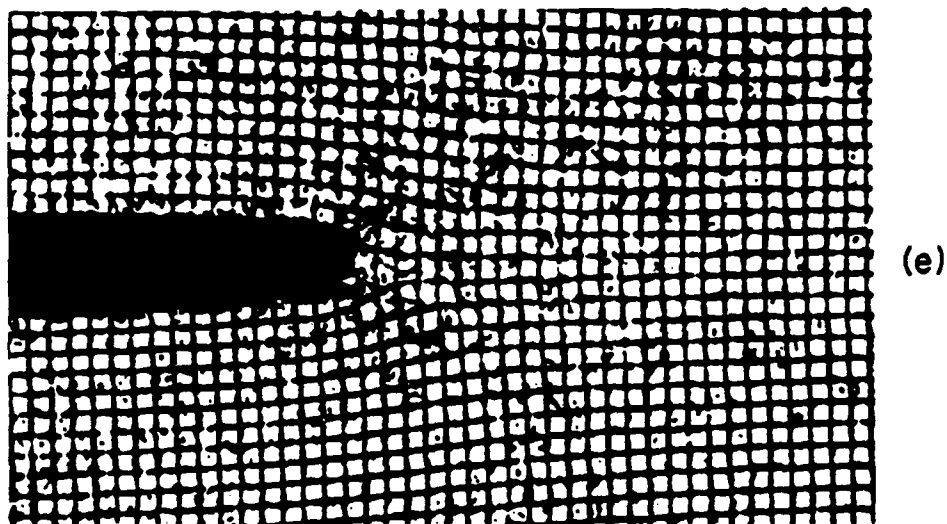


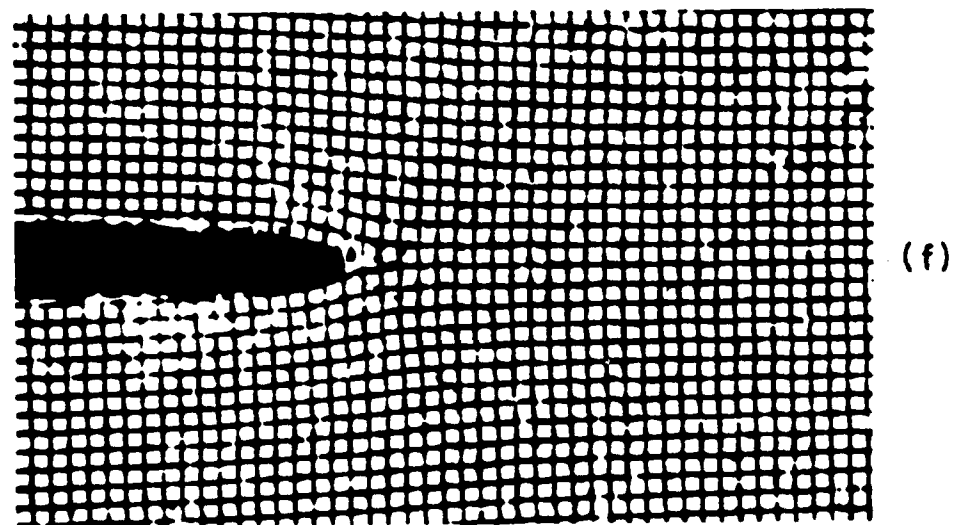
Fig. 14 Deformation for maximum crack opening prior to crack growth.  
(a) Spec. 1; (b) Spec. 10; (c) Spec. 3.



(d)



(e)



(f)

Fig. 14. cont. Deformation for maximum crack opening prior to crack growth. (d) Spec. 5; (e) Spec. 7; (f) Spec. 8.

Table 3  
BLUNT-TIP HEIGHT

Test No.	Specimen Thickness inches	Cross-head Speed, in./min	Blunt-tip Height, inches*		
			for Max. Opening prior to growth inches	During Crack Growth	
1	0.2	0.045	0.040	1.0	larger & smaller
2	0.2	0.07	0.056	1.4	larger & smaller
10	0.2	1.0	0.016	0.4	larger & smaller
9	0.6	0.0	0.024	0.6	same & smaller
3	0.6	0.10	0.056	1.4	larger & smaller
5	0.6	0.10	0.032	0.8	larger & smaller
6	0.6	0.10	**	**	0.016 in. (0.4 mm) typical
7	0.6	1.0	0.028	0.7	smaller
8	0.6	1.0	0.012	0.3	same & smaller

\* On 125 lines/in. grid surface

\*\* Crack growth began immediately upon loading

To convert to metric: 1 in. = 25.4 mm



loading rate exhibit significantly different blunting behavior both before and during crack growth. It suggests that the local arrangement of inclusions at the crack tip plays a role in the blunting phenomenon.

In addition, blunt-tip heights measured on the tacky side of the specimen regularly exceeded those on the non-tacky side. The average blunt-tip height was twice as great on the tacky side.

Table 3 indicates a typically smaller blunting at the 1.0 in./min (25 mm/min) loading rate. This is consistent with the viscoelastic nature of the rubber matrix. Since these results were all from the non-tacky side, and in view of the large variation found with replicate specimens, the results cannot be viewed as a definitive trend.

Crack-tip blunting that occurs during crack extension is illustrated in Fig. 13b and also by several examples in Figs. 15a and b. The blunting qualities observed during the crack opening phase are exhibited in the crack growth phase, too. The magnitude of blunting varies from specimen to specimen, it is different on the two outside surfaces of the specimen at any instant, and it varies irregularly with position in the specimen as the crack front advances. Since the local arrangement of inclusions is a random function of position, crack-tip blunting might be expected to vary with position of the advancing crack tip. With regard to its magnitude, the results indicate smaller crack-tip blunting during crack growth, compared to crack opening, when the loading rate was increased to 1.0 in./min (25 mm/min).

#### Results: Fracture Surfaces

The fracture surfaces were very rough. Abrupt changes of slope of the fracture surface were evident, both along the crack length and along

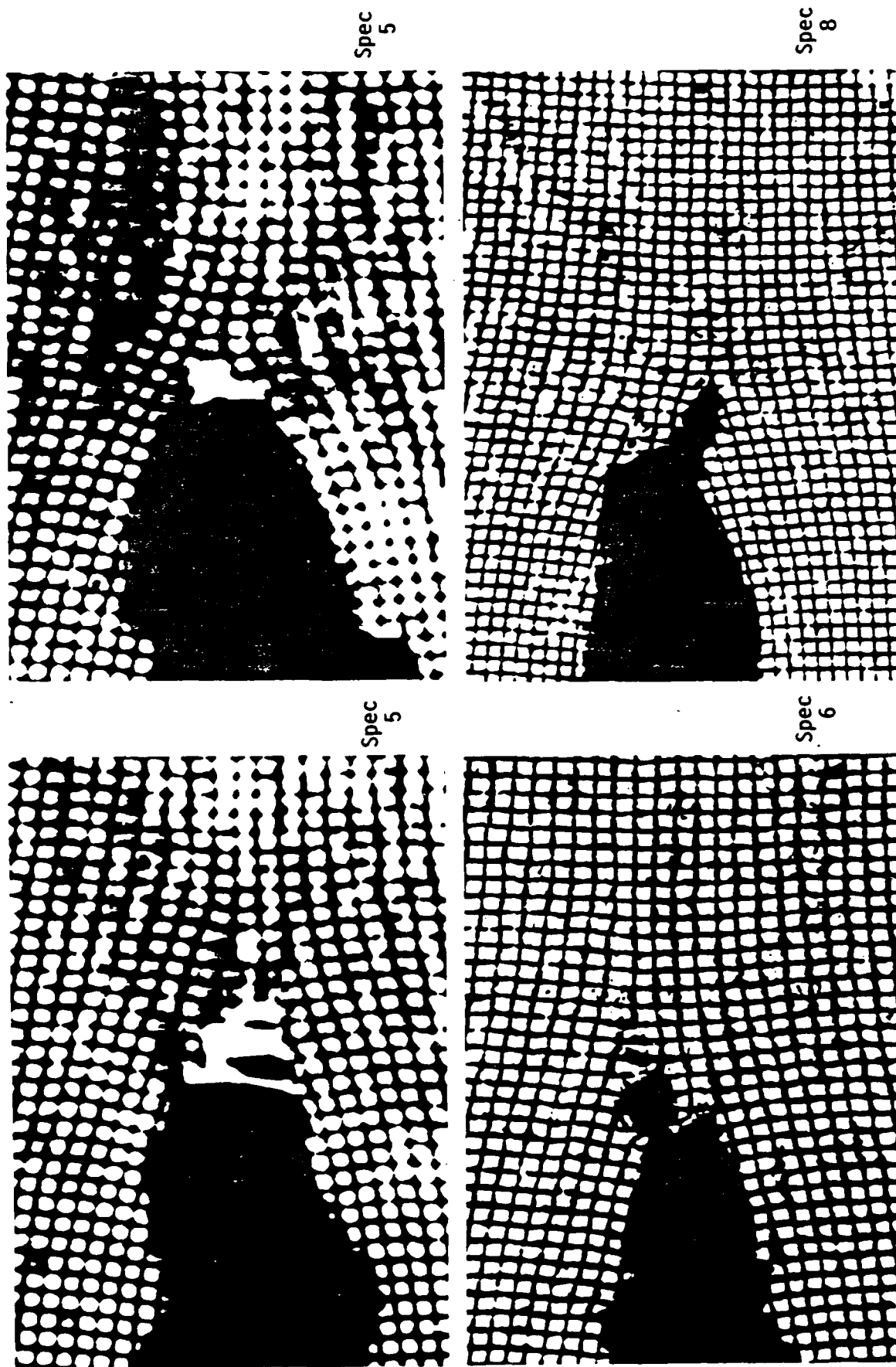


Fig. 15a Deformation during crack growth phase. Grid 125 lines per inch (5 lines per mm).

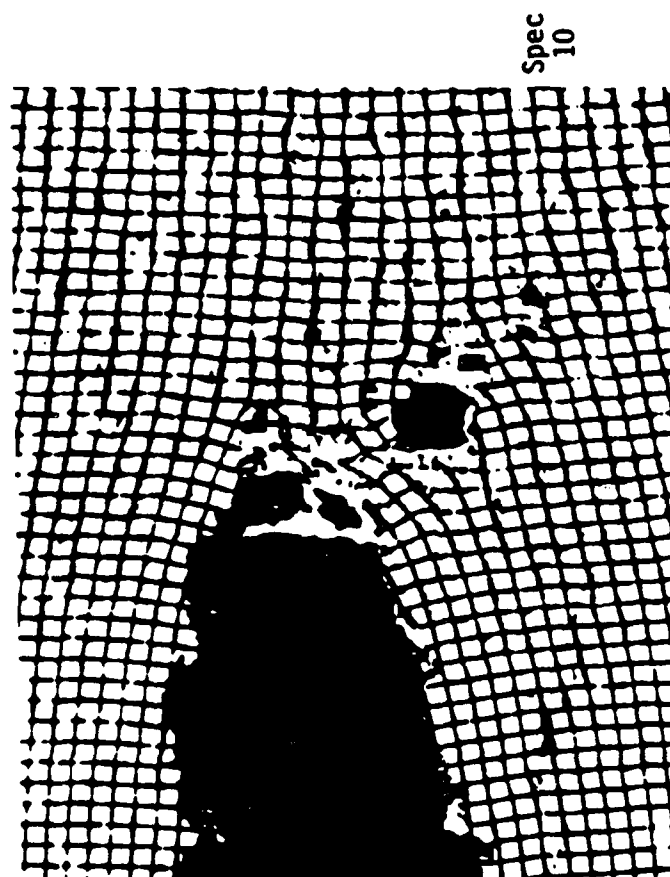
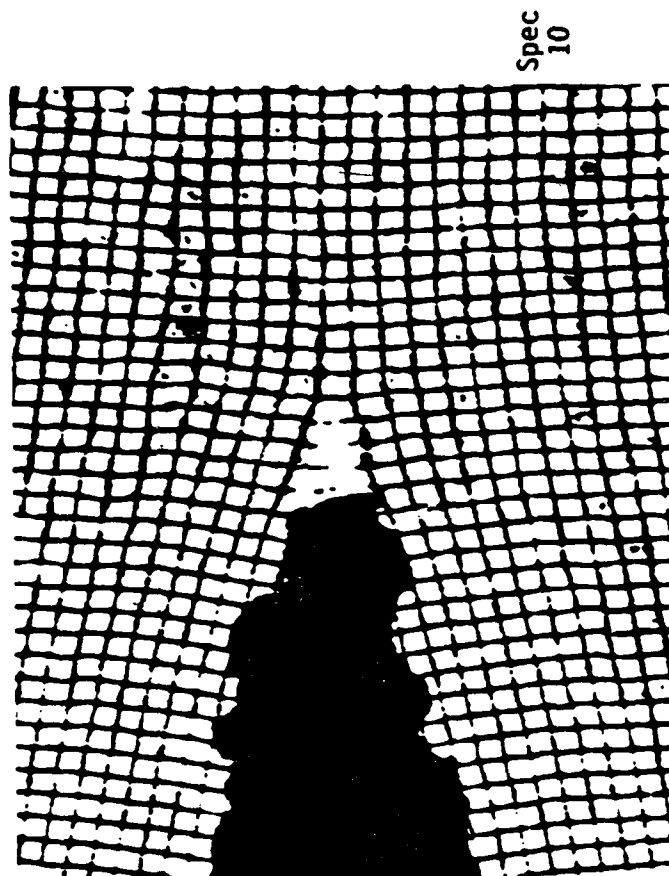


Fig. 15a cont. Deformation during crack growth phase. Grid 125 lines per inch (5 lines per mm).

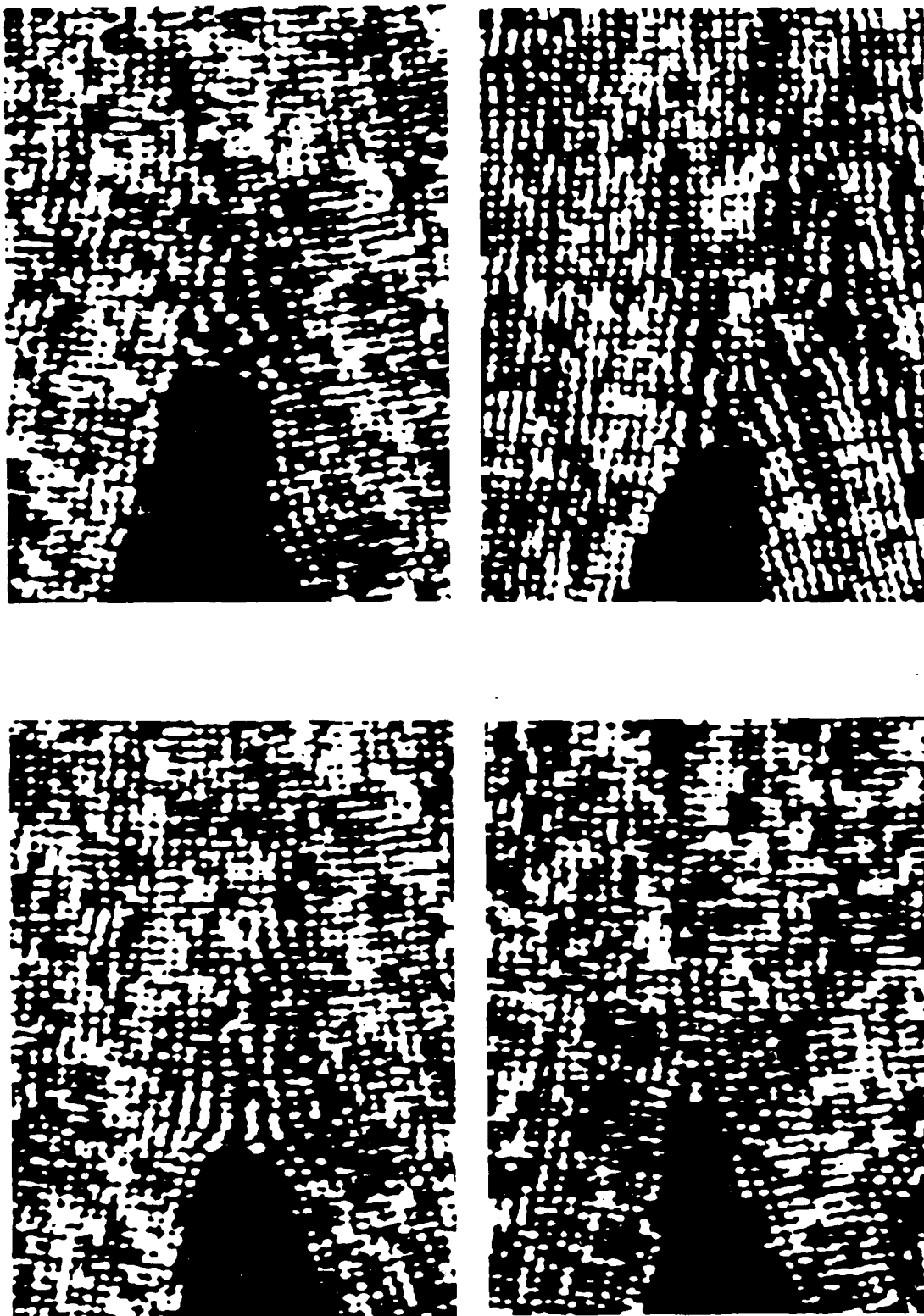


Fig. 15b Deformation during crack growth phase. Grid 500 lines per inch (20 lines per mm); Specimen 9.

the crack border, i.e., across the specimen thickness. The fracture appeared to be confined to the rubber matrix. Inclusions were not dislodged, but remained imbedded in the matrix on both sides of the fracture, again with very few exceptions.

#### Results: Global Deformations

By mutual agreement, displacement and strain data are being transmitted to the sponsor on computer diskettes for the tests and frame numbers shown in Table 2. The results of data reduction are given for a representative case in the sequence of graphs of Fig. 16a-h. The data are taken from the deformed grid of Fig. 13a [image (g)], which represents the maximum crack opening prior to crack growth.

The locations of grid intersection points were digitized and their displacements relative to the undeformed grid [Fig. 13a, image (a)] were calculated. Four-point smoothing was used (Appendix E), which reduced the experimental error of reading the grid and it attenuated local anomalies that existed in the real deformation of the heterogeneous specimen. It is a smoothing function of modest strength, which does not mask the nonuniform deformations, but attenuates them.

Figure 16a indicates the displaced positions of the digitized grid points. Its particular purpose, here, is to show that data were taken at small intervals near the crack and at larger intervals in remote zones. The corresponding locations of data points are marked in the subsequent graphs. However, they are shown in their original positions, not their displaced positions. The x,y positions of all points in the subsequent graphs, and the displacements and strains at these points, are all mapped on the original coordinates of the specimen. The lips of the crack are represented in Fig. 16 by a single line of zero width.

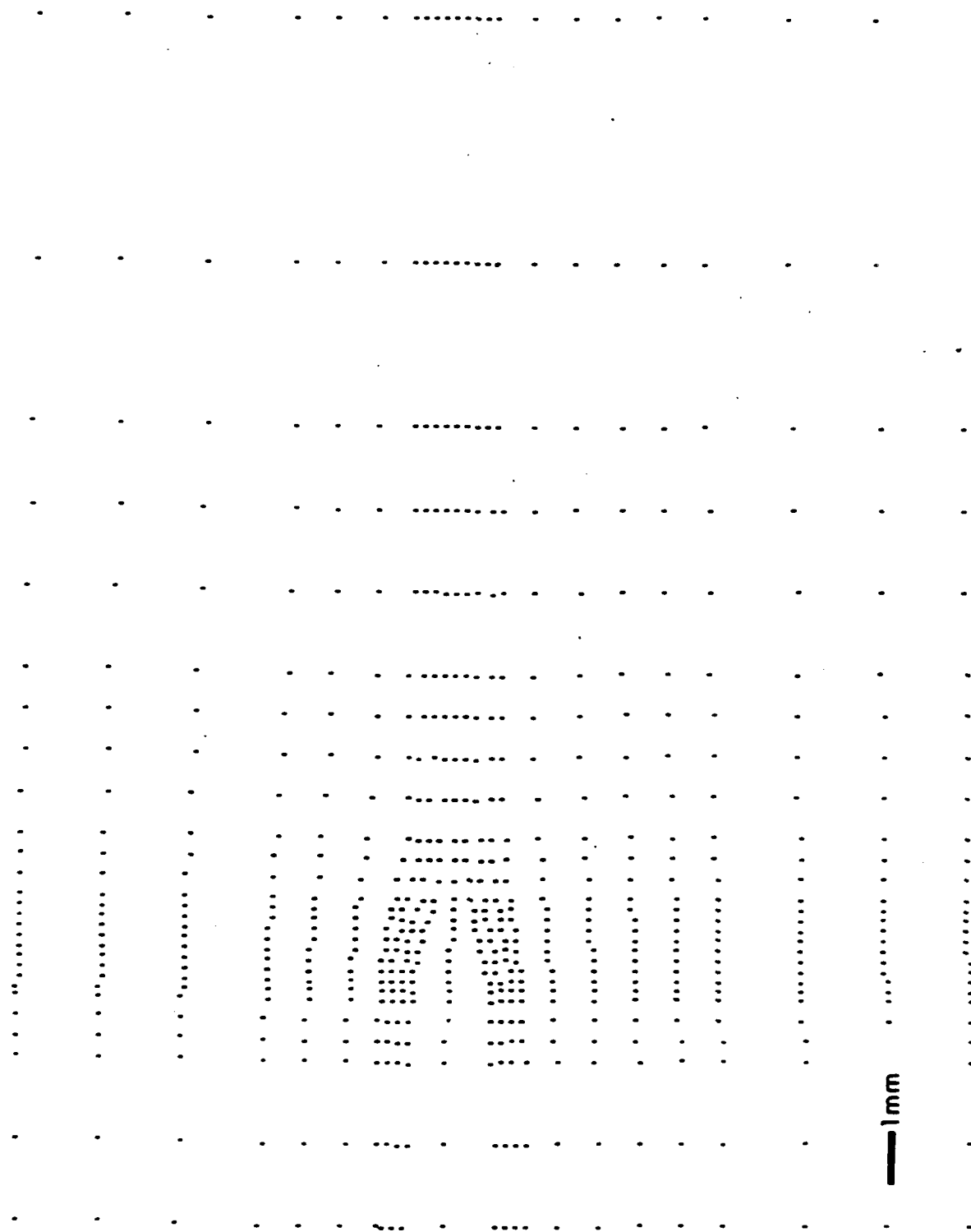


Fig. 16a. Displaced positions of digitized grid points. Test 1, frame 12.

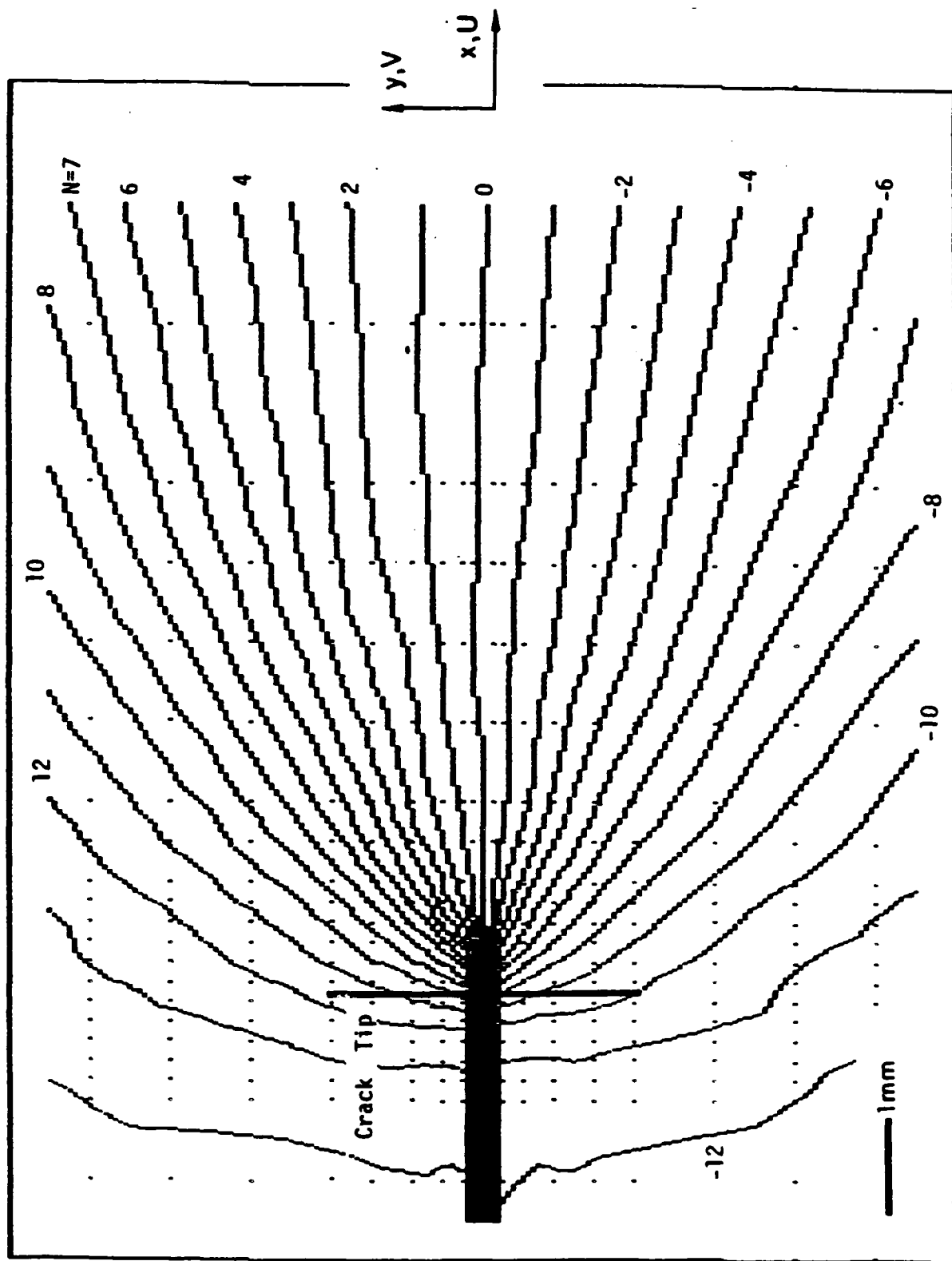


Fig. 16b Contour map of V displacement. Test 1, frame 12.  $V = 0.05 \text{ N}$   
 $\text{mm} = 0.002 \text{ N in.}$

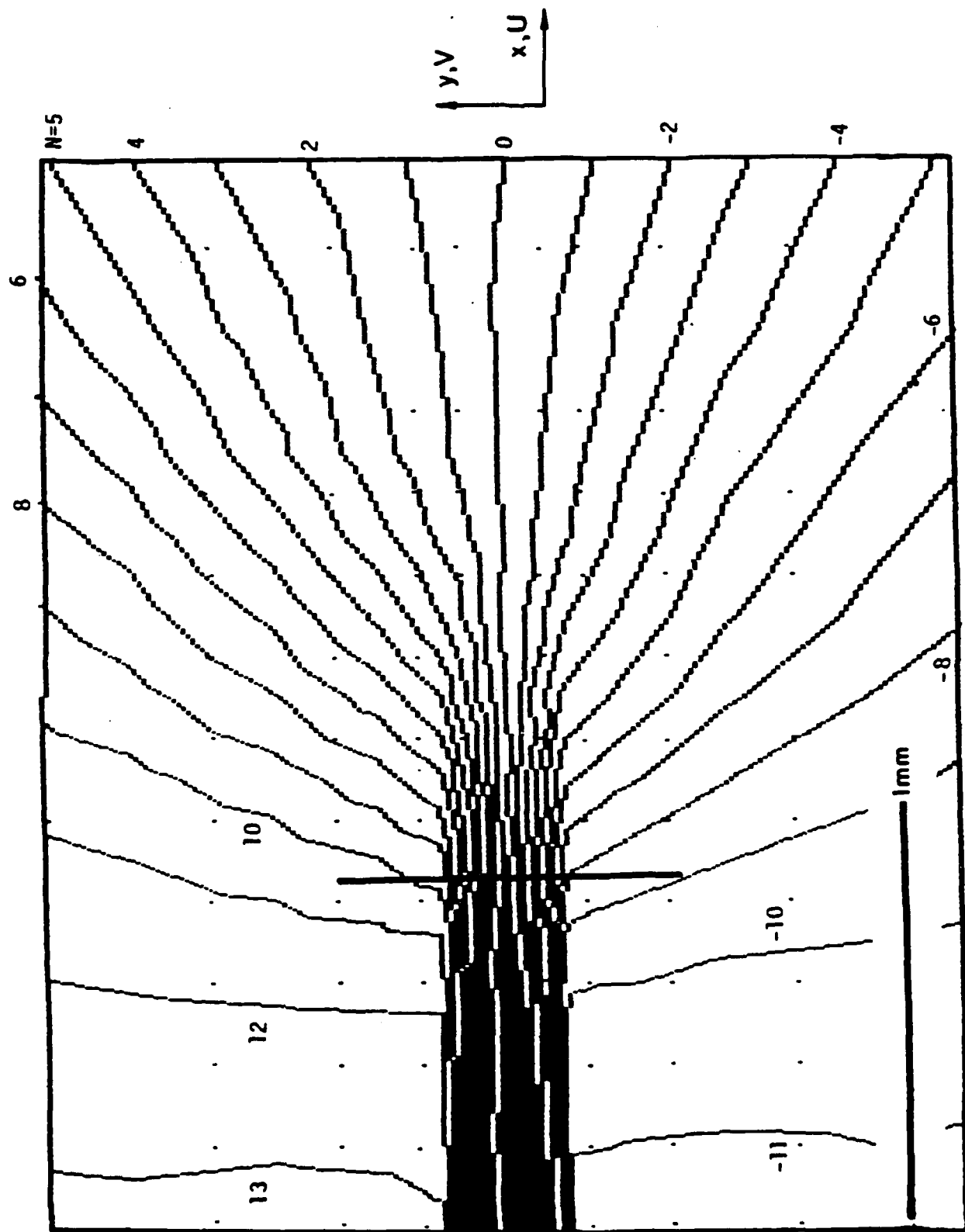


Fig. 16c Contour map of V displacement. Test 1, frame 12.  $V = 0.05 \text{ N}$   
 $\text{mm} = 0.002 \text{ N in.}$



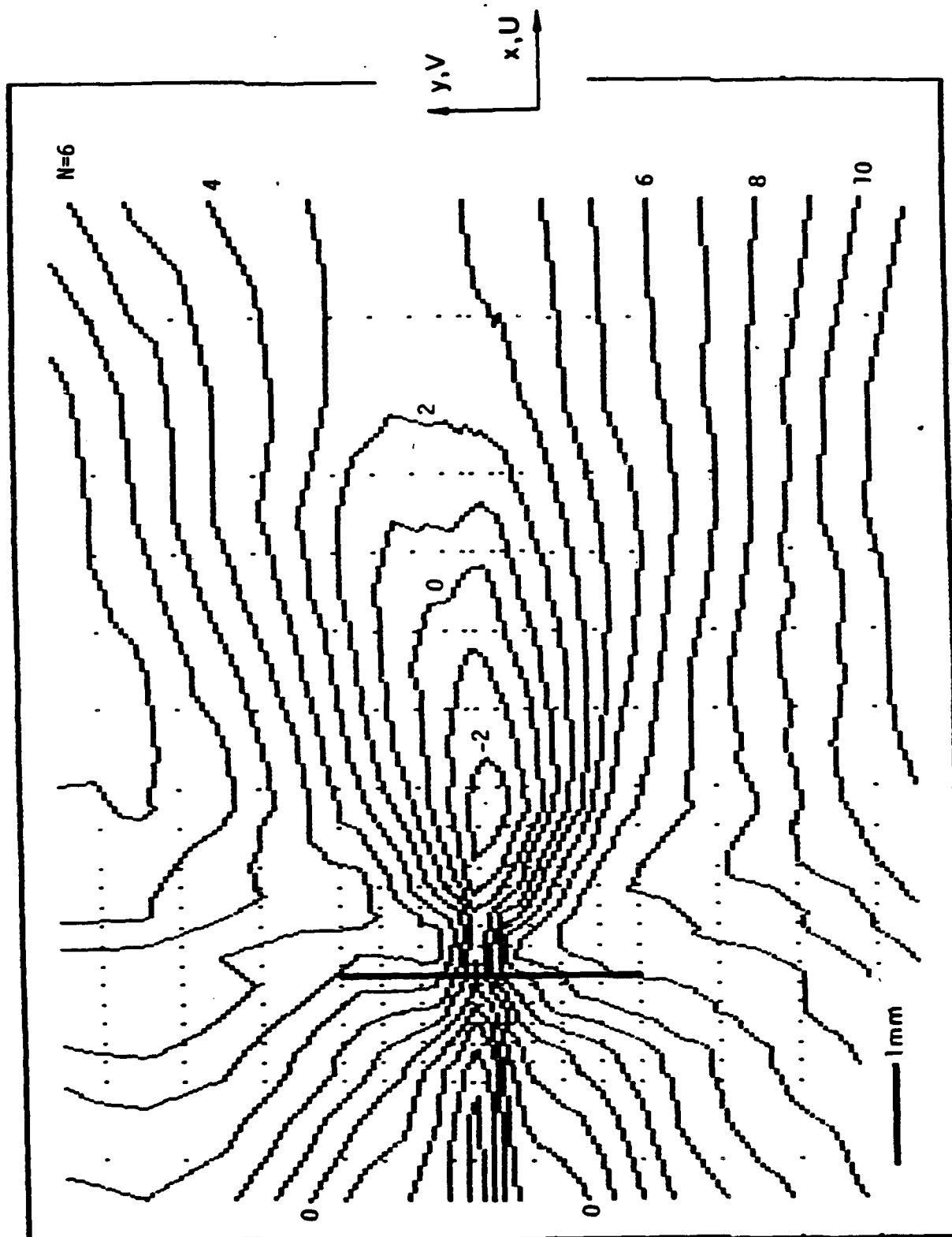


Fig. 16d Contour map of U displacement. Test 1, frame 12.  $U = 0.01 \text{ N}$   
 $\text{mm} = 0.0004 \text{ N in.}$

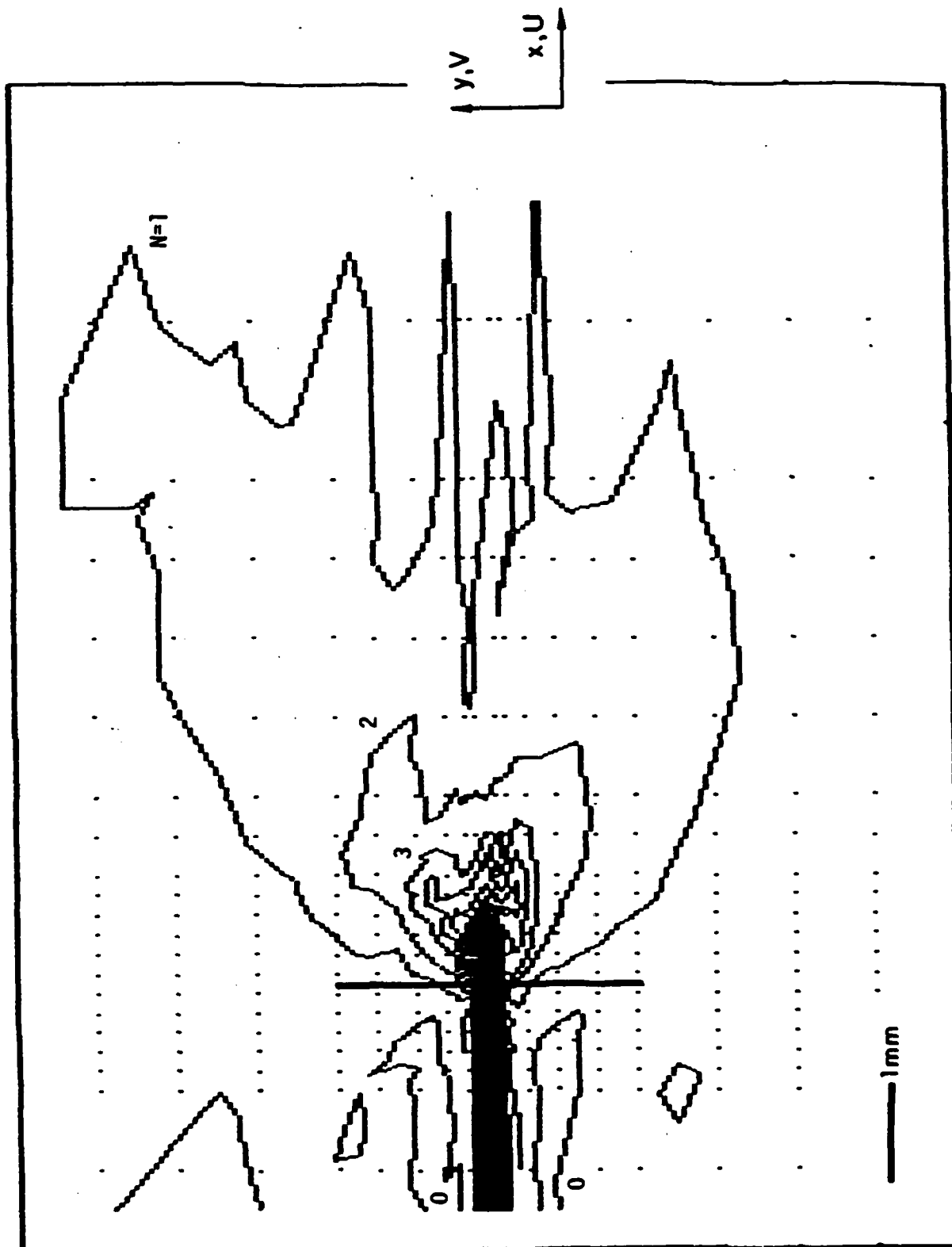


Fig. 16e Contour map of strain  $\epsilon_y$ . Test 1, frame 12.  $\epsilon_y = 0.05 N_1$

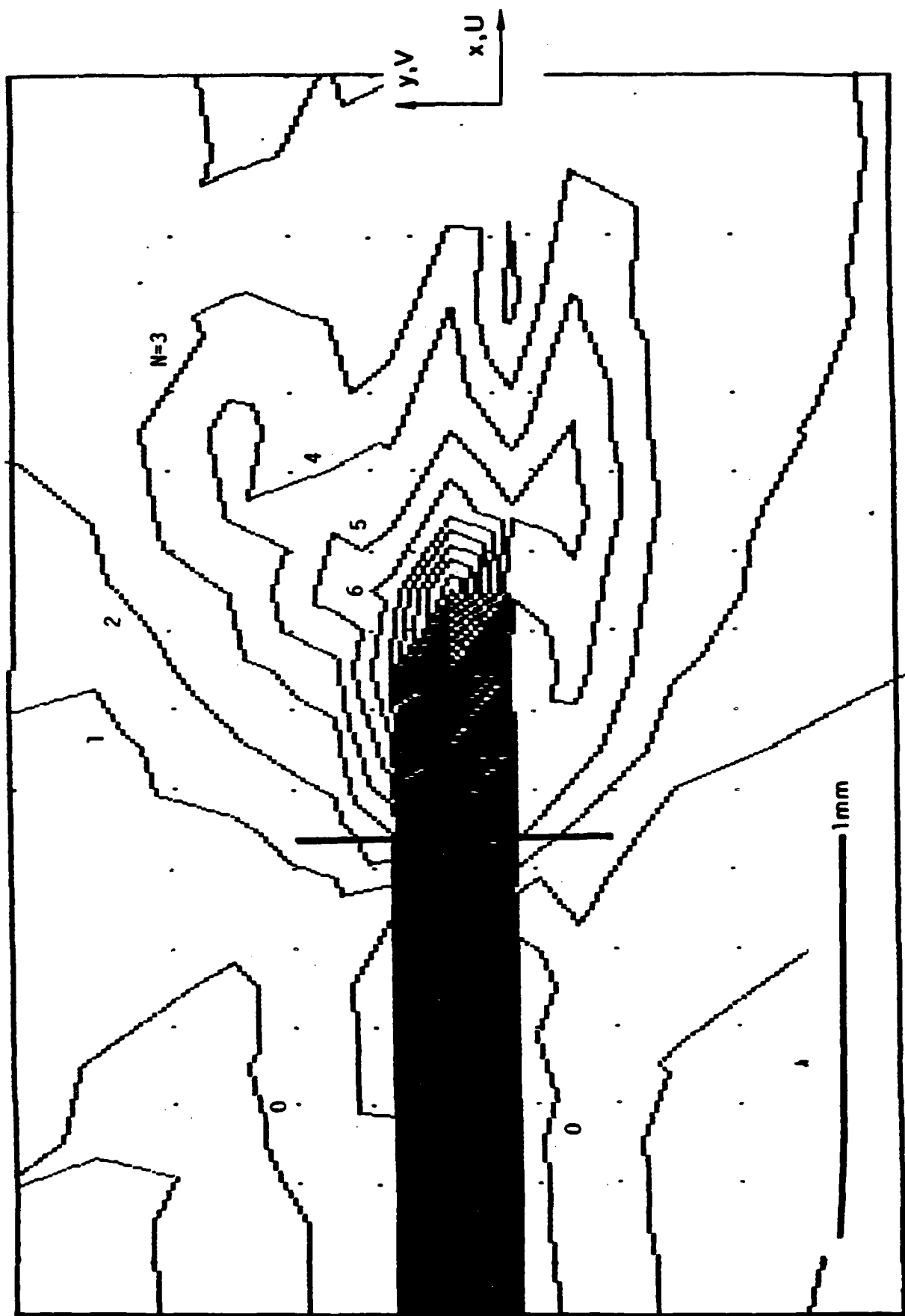


Fig. 16f Contour map of strain  $\epsilon_y$ . Test 1, frame 12.  $\epsilon_y = 0.05 N$ .

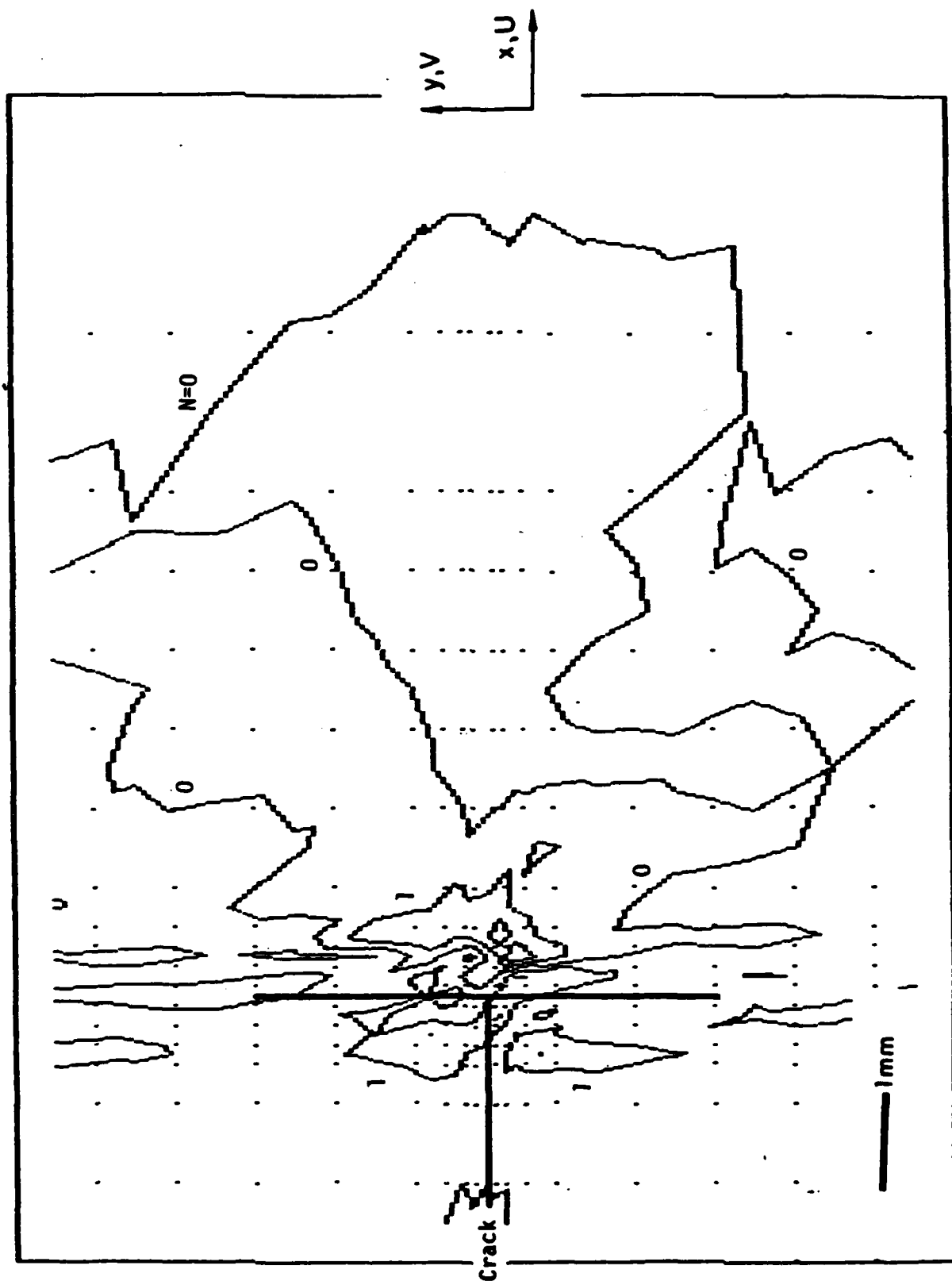


Fig. 16g Contour map of strain  $\epsilon_x$ . Test 1, frame 12.  $\epsilon_x = 0.02$  N.

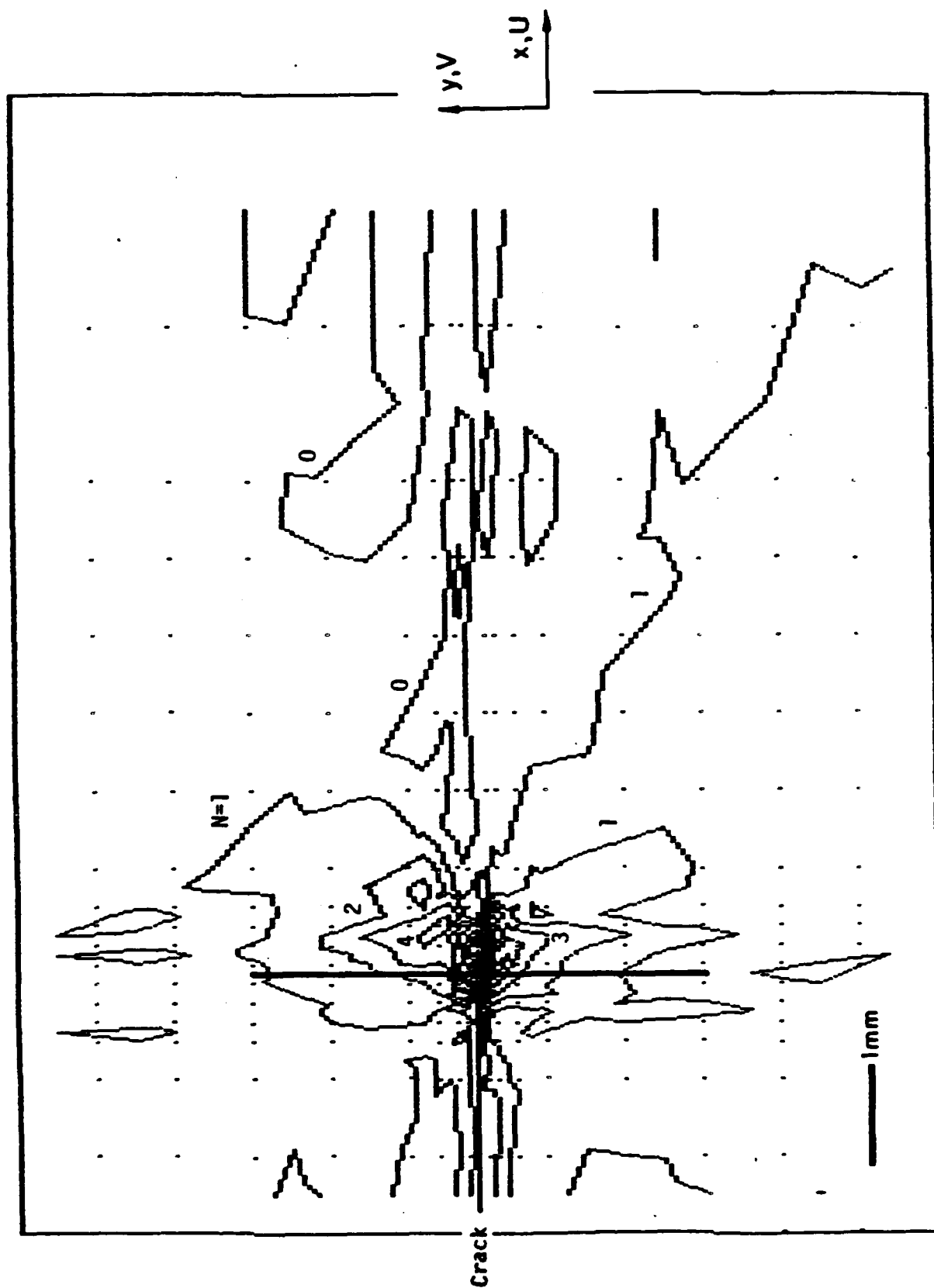


Fig. 16h Contour map of strain  $\gamma_{xy}$ . Test 1, frame 12.  $\gamma_{xy} = 0.04 N$ .

Figure 16b is the V-displacement field, obtained by connecting points of equal V displacement. The contour interval is 0.05 mm or 0.002 in. and the displacement at any point is the contour interval multiplied by the contour number N at the point; N can be interpolated between curves. Figure 16c is a magnified view of the V field near the crack. Some lack of symmetry and lack of smoothness is evident in both figures.

What is the meaning of the broad black region near the crack? It is not the shape of the crack opening. Instead, it represents the zone around the crack where meaningful data are not available, approximately one grid pitch from the crack lips.

The U displacements -- perpendicular to the loading direction -- are plotted in Fig. 16d. Note that the contour interval is very small, 1/5 that of the V contours. Accordingly the gradients of U are relatively small and the related strain contributions are small. Note, too, that the contours are free of severe oscillations. This means that the effective resolution of the technique is a fraction of the contour interval, or about 2.5  $\mu\text{m}$  or 100  $\mu\text{in.}$  By this argument, irregularities in a contour that exceeds about 1/3 the distance to the neighboring contour represents a real irregularity in the specimen deformation; in the preceding V contours, irregularities of 1/15 of the contour spacing represent real behavior. Curiously, the 100  $\mu\text{in.}$  (2.5  $\mu\text{m}$ ) resolution is equal to the resolution of the grid digitizing equipment (Appendix D), which implies that the error in locating grid intersection points did not exceed the system resolution.

Figures 16e and f are contour maps of the dominant strains,  $\epsilon_y$ . These contours are much less smooth than the displacement contours.

This is natural, because strains are highly sensitive to small irregularities of displacements. It is reasonable to expect that a portion of the irregularities stems from experimental error, but the results are reasonable assessments of actual specimen behavior. The major irregularities represent local strain anomalies in this heterogeneous material.

These strains were calculated by the relationship  $\epsilon_y = \partial V / \partial y$ , which results from Eq. 1 when the derivatives of U and W are negligible.

The calculation of strains did not use the smoothed displacement data. Instead, for each array of 4 measurement points forming a rectangle, the change of length of the vertical sides of the rectangle were determined and averaged; similarly for the horizontal sides; the three strains,  $\epsilon_y$ ,  $\epsilon_x$  and  $\gamma_{xy}$ , were determined from these averaged changes of length and assigned to the center-point of the rectangle. This interpretation of the raw data afforded only a small degree of smoothing, providing some attenuation of severe irregularities. Another factor that provided attenuation of irregularities was increase of gage length. The array of 4 data points forming the rectangle was not necessarily the 4 nearest points; the rectangles used for strain calculations were larger, so the effective gage lengths -- the sides of the rectangle -- were larger and the local irregularities were smoothed. The locations of the data points used for the calculations are printed on each figure. In these experiments, the pitch of the grid printed on the specimen was less than half the width of the largest (rigid) inclusions, and extensive small-scale irregularities of deformation are inevitable. The data reduction techniques were designed to mask or attenuate some of these, for otherwise the contour maps of

strain would show great oscillations instead of the general strain trends.

Figure 16g shows the contours of  $\epsilon_x$ , but with a smaller contour interval. Clearly these strains are very small and insignificant compared to  $\epsilon_y$ .

Figure 16h shows  $\gamma_{xy}$ , the in-plane shear strains near the crack. The shear strains are significant near the tip of the crack, and insignificant elsewhere. This is also evident in Fig. 13a (image g) which shows the change of grid elements from rectangular to rhomboidal shape near the crack tip.

The shear strain was calculated by the strain relationship

$$\gamma_{xy} = \partial U / \partial y + \partial V / \partial x \quad (3)$$

A more rigorous calculation would use the Lagrangian large strain relationship

$$\gamma_{xy}^L = \arcsin \frac{\frac{\partial U}{\partial y} + \frac{\partial V}{\partial x} + \left(\frac{\partial U}{\partial x}\right)\left(\frac{\partial U}{\partial y}\right) + \left(\frac{\partial V}{\partial x}\right)\left(\frac{\partial V}{\partial y}\right) + \left(\frac{\partial W}{\partial x}\right)\left(\frac{\partial W}{\partial y}\right)}{(1 + \epsilon_x^L)(1 + \epsilon_y^L)} \quad (4)$$

For shear strains near 0.3, the arcsin and the angle in radians are nearly equal. As already indicated,  $\epsilon_x$ , or  $\partial U / \partial x$ , is negligible and the product of derivatives of  $W$  are negligible. In the region where  $\gamma_{xy}$  is large,  $\partial U / \partial y$  is much smaller than  $\partial V / \partial x$ , as seen in the grid of Fig. 13a (image g). Under these conditions, the right side of Eq. 4 reduces to  $\partial V / \partial x$ , so use of Eq. 3 is justified as a good approximation.

Figure 17a shows the  $V$ -displacement fields around cracks that have reached their maximum opening prior to crack growth. The vertical line indicates the location of the crack tip in each case. The bar in each



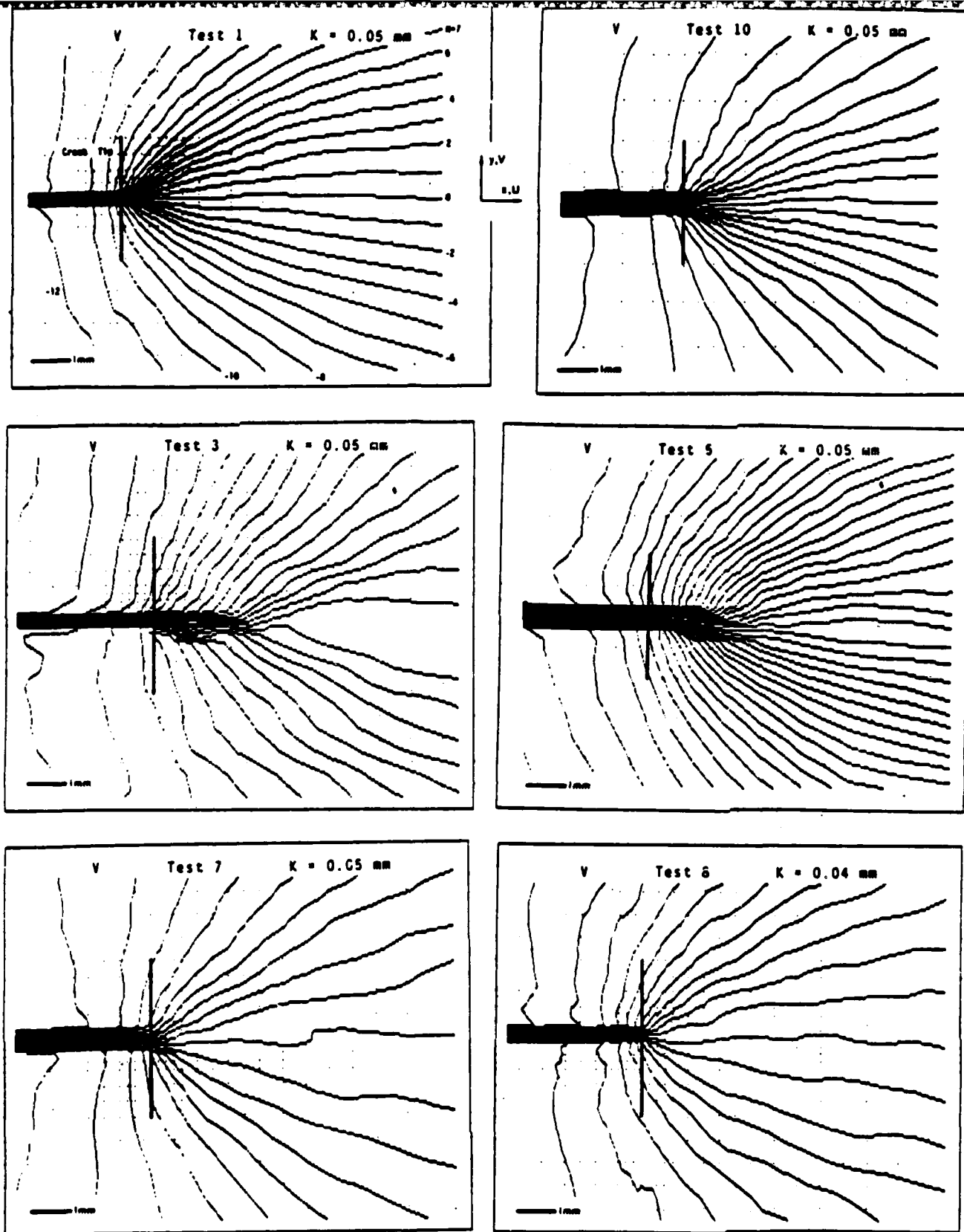


Fig. 17a V-displacement fields for maximum crack opening prior to crack growth.

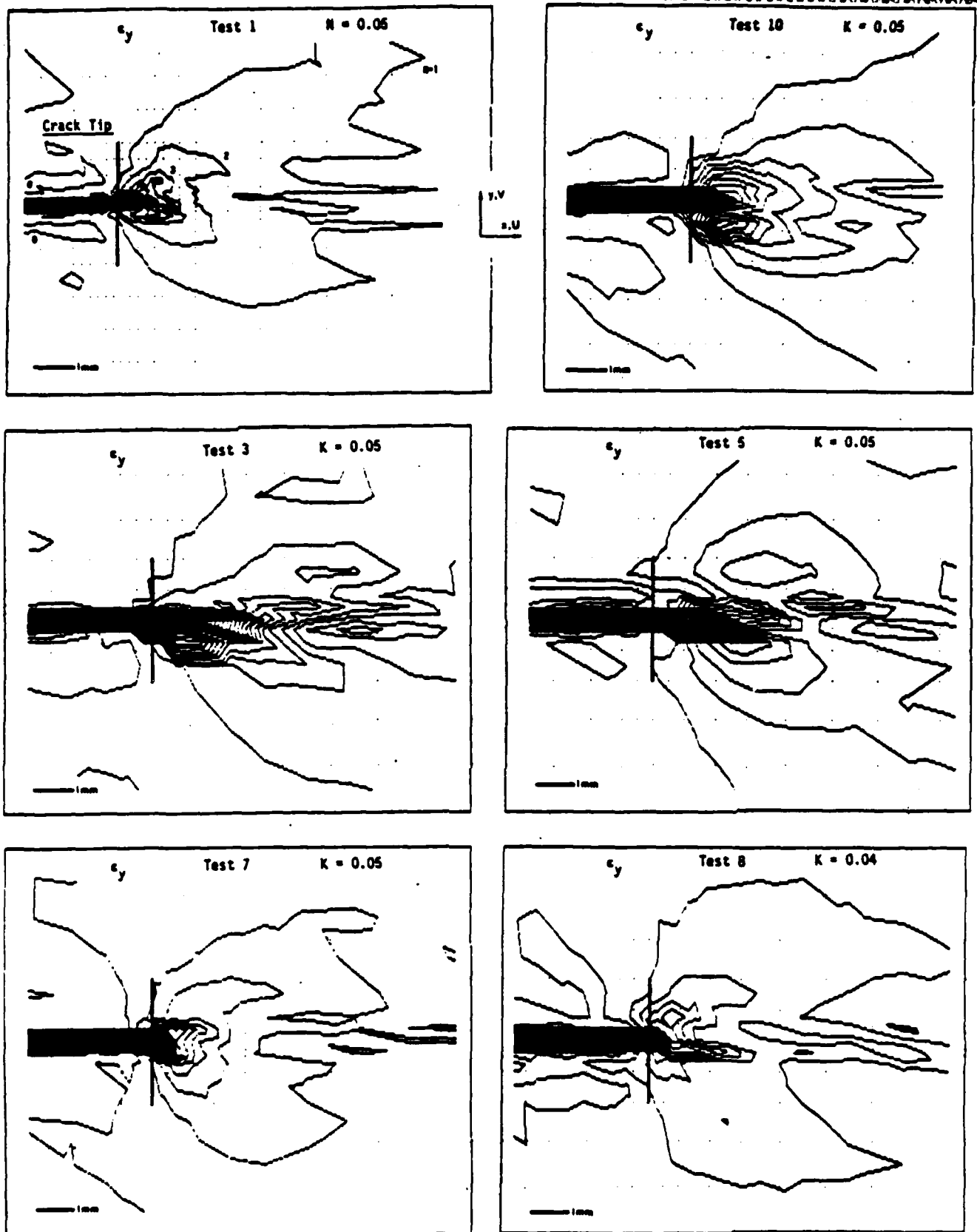


Fig. 17b  $\epsilon_y$  fields for maximum crack opening prior to crack growth.

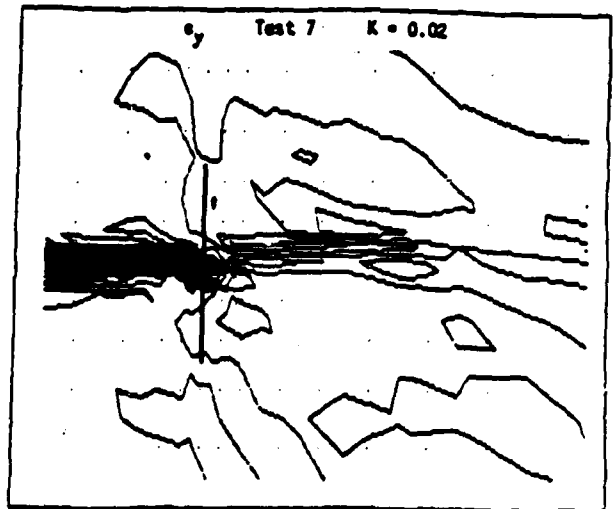
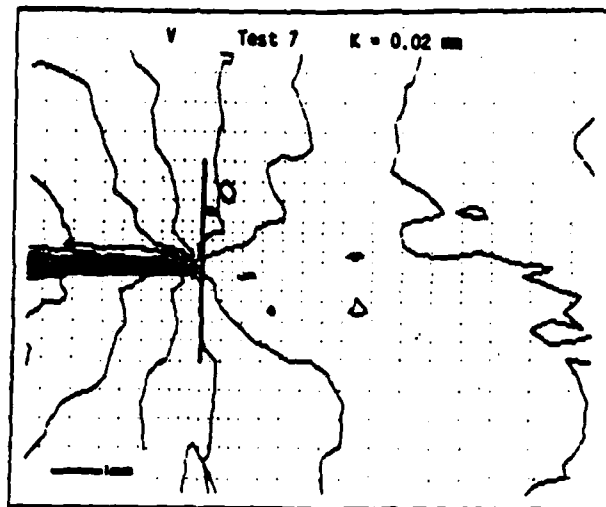
lower-left corner is a scale representing 1-mm length in the specimen. The contour interval is  $K$ , given in mm of displacement per contour level. Again, data points are plotted in their initial positions. The contour maps show essentially the same global features for each test. Local irregularities appear in the contours and they appear to be randomly distributed.

The corresponding strain fields,  $\epsilon_y$ , are shown in Fig. 17b. The crack positions and scales are defined as before. The contour interval  $K$  is the strain (m/m) per contour level. Again the general features are the same for each test. Local random irregularities are extensive, as expected for the heterogeneous specimen material. The patterns show (irregular) cusp-shaped contours symmetrical with the crack plane; on lines  $x = \text{constant}$ , ahead of the crack,  $\epsilon_y$  reaches its maximum value at some distance from the crack plane.

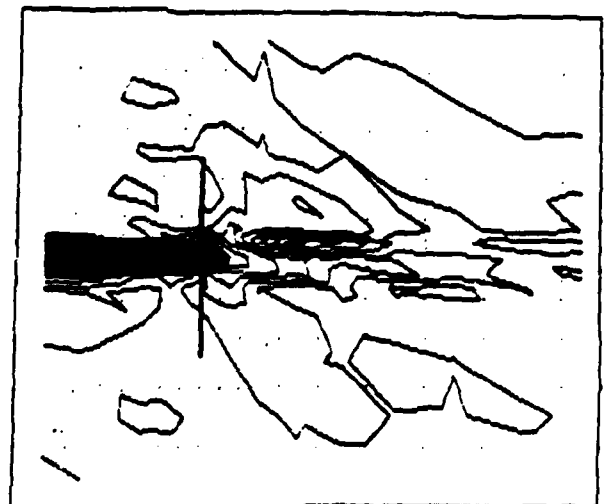
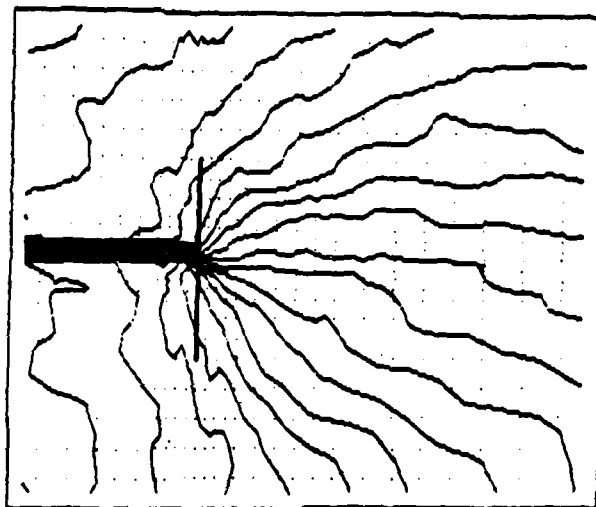
Strain rate effects are shown in Fig. 18. The rate of deformation is not constant. Instead, as the specimen is stretched with a uniform rate of grip displacement, the deformation increases slowly at first and then more quickly.

In the three time intervals of one second each, the crack opening increased progressively by 0.08, 0.16 and 0.22 mm. This strong nonlinearity indicates a redistribution of material compliance during the test. It changes from a uniform compliance throughout the specimen at the beginning of the test to a subsequent condition of increased compliance locally where strains become high. A physical model of such material behavior is proposed in Appendix H.

Deformation during 0-1 second.



Deformation during 1-2 second.



Deformation during 2-3 second.

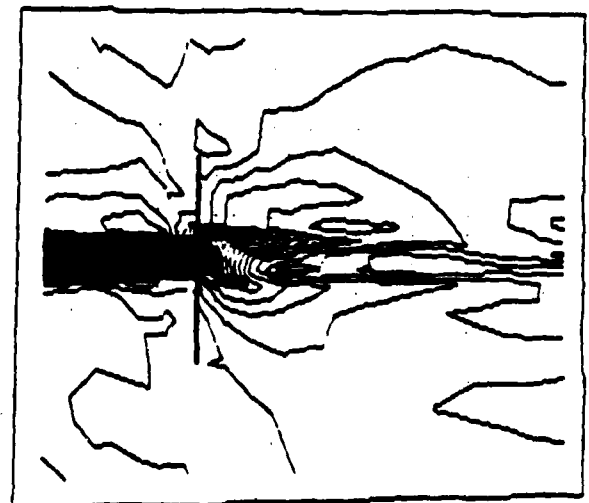
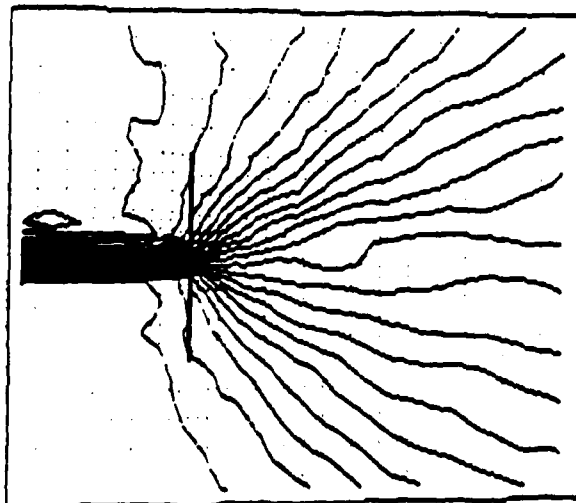


Fig. 18 Displacement  $V$  and strain  $\epsilon_y$  accumulated during sequential one second intervals during crack opening phase. Specimen 7: 0.6 in. (15 mm) thick; 1.0 in. (25 mm) per min loading rate.

### Interpretation: Process Zone

The model proposed in Appendix H is developed to explain the physical behavior in the process zone, or pre-crack zone. The model is explained in terms of idealized arrangements of rigid inclusions in the rubber matrix, but the general features should apply to the random arrangement present in the real specimen material. Since the specimen has random qualities, however, the model represents generalizations or first approximations of its performance. The model prescribes the following performance.

1. The process or pre-crack zone extends as a triangular region ahead of the blunt crack tip. Virtually no inclusions lie in this zone. Instead, the zone separates inclusions that were previously located on each side of a very narrow path of matrix rubber.
2. The material in the pre-crack zone is matrix rubber that spans the zone as narrow ligaments. The magnitude of the normal strain in the ligaments is of the order of  $\epsilon_y \approx 5$ .
3. Let the rubber surrounding the inclusions in the undeformed state be categorized as having basically vertical elements (with their long dimension parallel to the load direction) and horizontal elements. The ligaments are extended bodies of matrix rubber that were previously vertical elements between inclusions.
4. As the deformation develops from zero, horizontal elements of matrix rubber sustain the stress. The corresponding material stiffness is high. As deformation increases, voids are developed between horizontal surfaces of inclusions and rubber. Then debonding and relative sliding

between rubber and inclusions begins at the vertical interfaces. Debonding and sliding ceases where attached horizontal elements of matrix key the rubber to the inclusions. Substantially increased compliance accompanies this voiding and stretching of vertical elements of rubber.

5. The stretched vertical elements of rubber carry the load in both the pre-crack zone and the surrounding finite strain zone. This material stretches to form ligaments in the pre-crack zone, which subsequently rupture. Crack growth takes place as the ligaments in the pre-crack zone rupture.

6. Rubber-rich surface layers bound the outside surfaces of the triangular pre-crack zone. They stretch to span the pre-crack zone. The vertical leg of the triangular surface layer is the apparent blunt end of the crack.

7. Large tensile strains and shear strains are developed in the surface layer. The principal tensile strain remains nearly vertical. Small cracks are formed ahead of the main crack, presumably wherever the principal strain reaches a critical value. The crack planes would be essentially horizontal like the main crack, but the crack lips deform into tall elliptical shapes in the severe strain field.

8. As the specimen is stretched, elliptical voids coalesce and also the blunt end of the surface layer progressively ruptures. Thus, the crack tip advances as new pre-crack material is developed ahead of it.

9. The end of the pre-crack zone in the surface layer probably lags that in the interior.

10. At any junction, the preferred path of the crack passes through the thinner layer of matrix rubber. Inclusion arrangements that inhibit high strains can act as crack arresters. Then a new pre-crack zone develops at a neighboring strain concentration.

#### Determination of $\lambda_u$ from Cracked Inert Propellant

Since tests on large polyurethane plates revealed no thickness effect upon the determination of  $\lambda_u$  for 6.4 and 12.7 mm thick specimens, it was decided to utilize the thin (5 mm thick) plates of inert propellant mainly to make specimens for pilot tests to determine measurement techniques and then utilize the thicker (15.25 mm) plates mainly for determination of  $\lambda_u$  values at various displacement head rates. Using this approach, values of  $\lambda_u$  were determined at several different global strain levels up to initiation of growth for three different head displacement rates.

A brief description of the data collection and reduction techniques used will now be presented. Figure 15b shows the surface profile of an opened crack with a surrounding grid of  $\approx 20$   $\mu$ /mm. Data are taken only along the vertical lines passing through the crack tip. Data points (i.e. locus of the intersection points of the grating lines) are collected and stored in a microcomputer using a digitizing table with resolution of 0.025 mm. Appropriate software were written for use in data collection and reduction. The error introduced into the data due to resolution error was found to be negligible so long as the photographic prints were magnified at least 10X. Data were collected both above and below the crack tip and were then averaged.

The coordinates of the grid points in the no load condition are necessary for data reduction. The no load coordinates can be found in

one of two ways. First, the enlarged photograph of the no-load grating can be read as previously described. Alternatively, the no load data point locations can be computed assuming perfect grid application. Both methods were used and gave essentially the same results. The present analysis was based upon the perfect grid assumption.

As noted in the previous section, the cracks in the inert propellant biaxial specimen tests exhibited severe blunting in some cases but not in others. In order to account for the blunting effect, it was necessary to further generalize the algorithm given by Eq. B9 for converting displacement data into the appropriate fracture parameter (in this case  $\lambda_u$ ). Basically, this involved the inclusion of a term  $(V)_0$  in the equation for the displacement  $V$  along  $\theta = \pi/2$ . Thus Eq. B8, when so modified becomes:

$$V = (V)_0 + D_y r^{\lambda_u} \quad (5)$$

whence

$$\ln [V - (V)_0] = \ln D_y + \lambda_u \ln r \quad (6)$$

The value of  $V$  is found by subtracting the  $y$  coordinate under load from its no-load value. Figure 19 indicates schematically the role of  $(V)_0$  and Figure 20 shows test data from which  $\lambda_u$  is determined. It is important to collect data over a much larger range than the zone dominated by  $\lambda_u$  so as to clearly delineate this data zone.

Data from four different tests were used to determine  $\lambda_u$  values. Information pertinent to these tests is presented in Table 4. The data from the specimens utilizing the 5 lines/mm grating were obtained by reading both the top and bottom of the horizontal grid lines instead of the central values. The location of the data zone dominated by the lowest eigenvalue  $\lambda_u$  is seen to be further from the crack tip due to



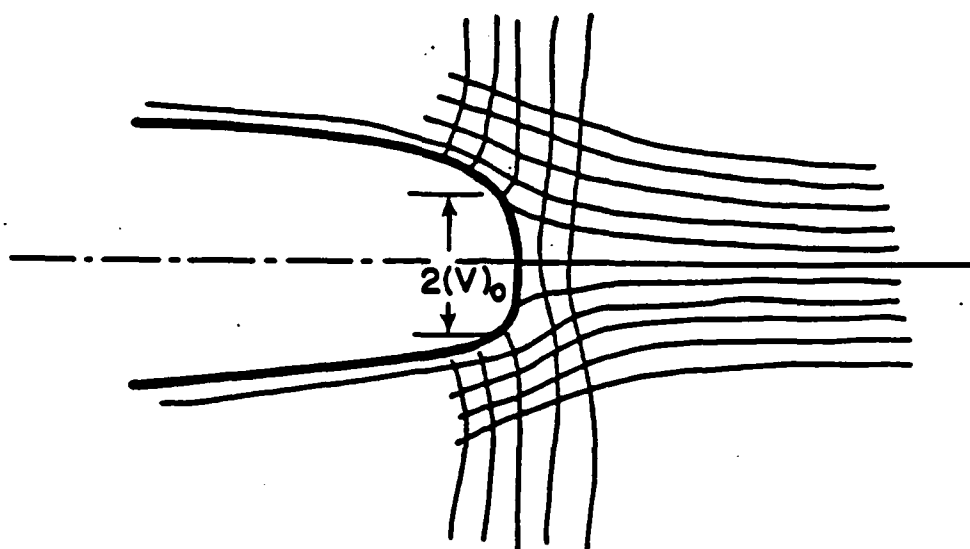


Fig. 19 The role of  $(V)_0$  in Equation 1.

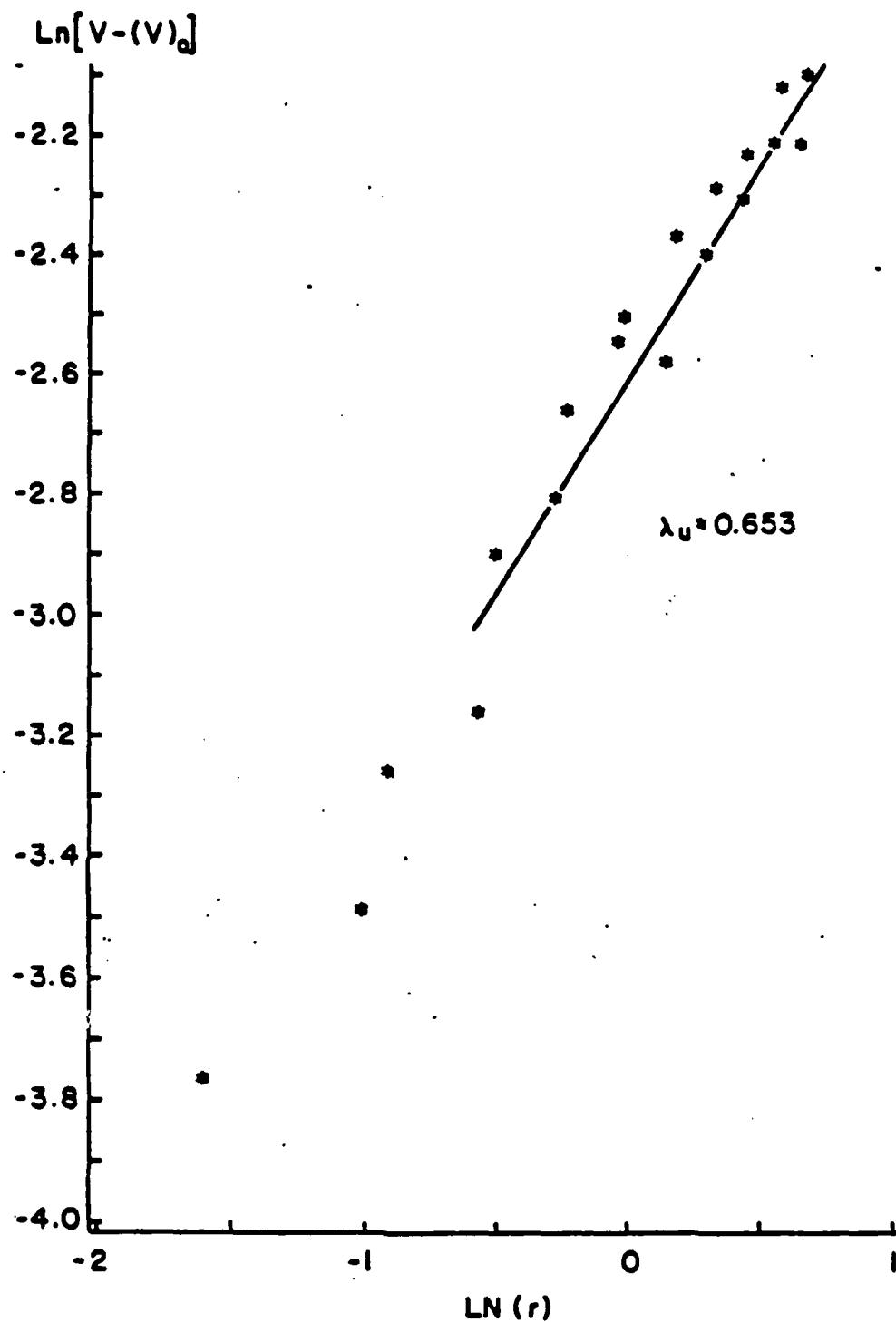


Fig. 20 Data Plot for Determination of  $\lambda_u$  for Inert Propellant.

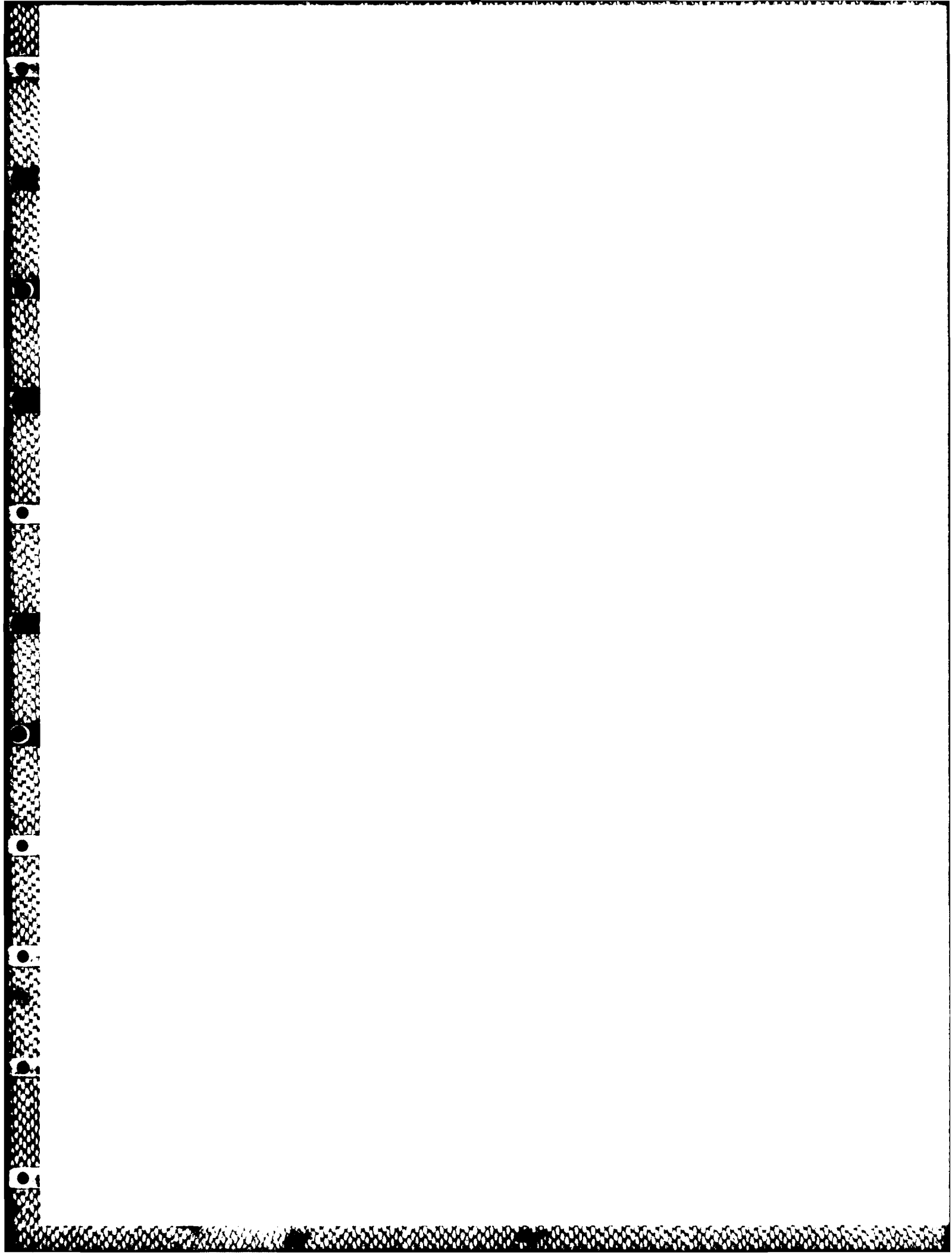


Table 4: Test Data for  $\lambda$  Determination

<u>Test</u>	<u>Head Rate (mm/min)</u>	<u>Grating Frequency <math>\lambda</math>/mm</u>	<u>Data Zone (mm)</u>
9	.25	20	0.5-1.5
5	2.5	5	0.6-1.6
6	2.5	20	0.6-1.0
8	25	5	1.0-2.0

Table 5: Test Data for  $\lambda$  Measurements

Test 9 - Range [0.5-1.5]mm      Displ. Rate = 0.01 in/min or 0.25 in/min

<u><math>\epsilon</math> (%)</u>	<u><math>\lambda_u</math></u>	
1.5	0.625	
3.0	0.687	
5.0	0.778	
5.5	0.748	$\lambda_u$ AVG = 0.71

Test 5 - Range [0.6-1.6]mm      Displ. Rate = 0.1 in/min or 2.5 mm/min

<u><math>\epsilon</math> (%)</u>	<u><math>\lambda_u</math></u>	
1.25	0.689	
2.10	0.698	
2.92	0.688	$\lambda_u$ AVG = 0.69

Test 6 - Range [0.6-1.0]mm      Displ. Rate = 0.1 in/min or 2.5 mm/min

<u><math>\epsilon</math> (%)</u>	<u><math>\lambda_u</math></u>	
1.25	0.707	
1.67	0.758	
2.10	0.630	
2.92	0.652	$\lambda_u$ AVG = 0.69

Test 8 - Range [1.0-2.0]mm      Displ. Rate = 1.0 in/min or 25 mm/min

<u><math>\epsilon</math> (%)</u>	<u><math>\lambda_u</math></u>	
5.0	0.653	
6.7	0.613	
8.3	0.565	
10.0	0.794	$\lambda_u$ AVG = 0.66

blunting than in the polyurethane models and its location varies somewhat in the different tests. The latter is attributed mainly to the heterogeneity of the inert propellant although the displacement rate may have had some influence.

The resulting values of  $\lambda_U$  are presented in Table 5. The average value of  $\lambda_U$  appears to decrease slightly with increasing global displacement rate. However, it should also be noted that some crack growth appeared to occur for the extreme load rates (i.e. Tests 8 and 9). Consequently, at this juncture, it would appear that  $\lambda_U$  is relatively independent of the head displacement rate. Taken collectively, for the 15 measurements, the results yield an average value of  $\lambda_U = 0.69$  with a standard deviation of  $\pm 0.06$ . These results compare favorably with Benthem's result of 0.67, suggesting that the continuum description of this phenomenon is still valid during the crack opening process in the inert propellant.

Returning now to Figure 9, and plotting  $\lambda_\sigma = |1 - \lambda_U| = 0.31$  avg, one would have a data point which would lie approximately on the lower bound of the frozen stress test data. Since the thickness of the compact bending specimens were approximately the same as the thicker biaxial inert propellant specimens, one may infer the transition zone for  $\lambda_\sigma$  (or  $\lambda_U$ ) to be the same thickness also. Finally, we arrive at the  $\lambda_\sigma$  distribution for the inert propellant by adjusting the transition zone to agree with the surface value of 0.31 and this is shown in Fig. 21. In view of the heterogeneous nature of the inert propellant, it appears inappropriate to attempt further refinement of the distribution. However, it should be noted that some crack growth did occur in the extremely slow and fast displacement rate cases, producing more scatter

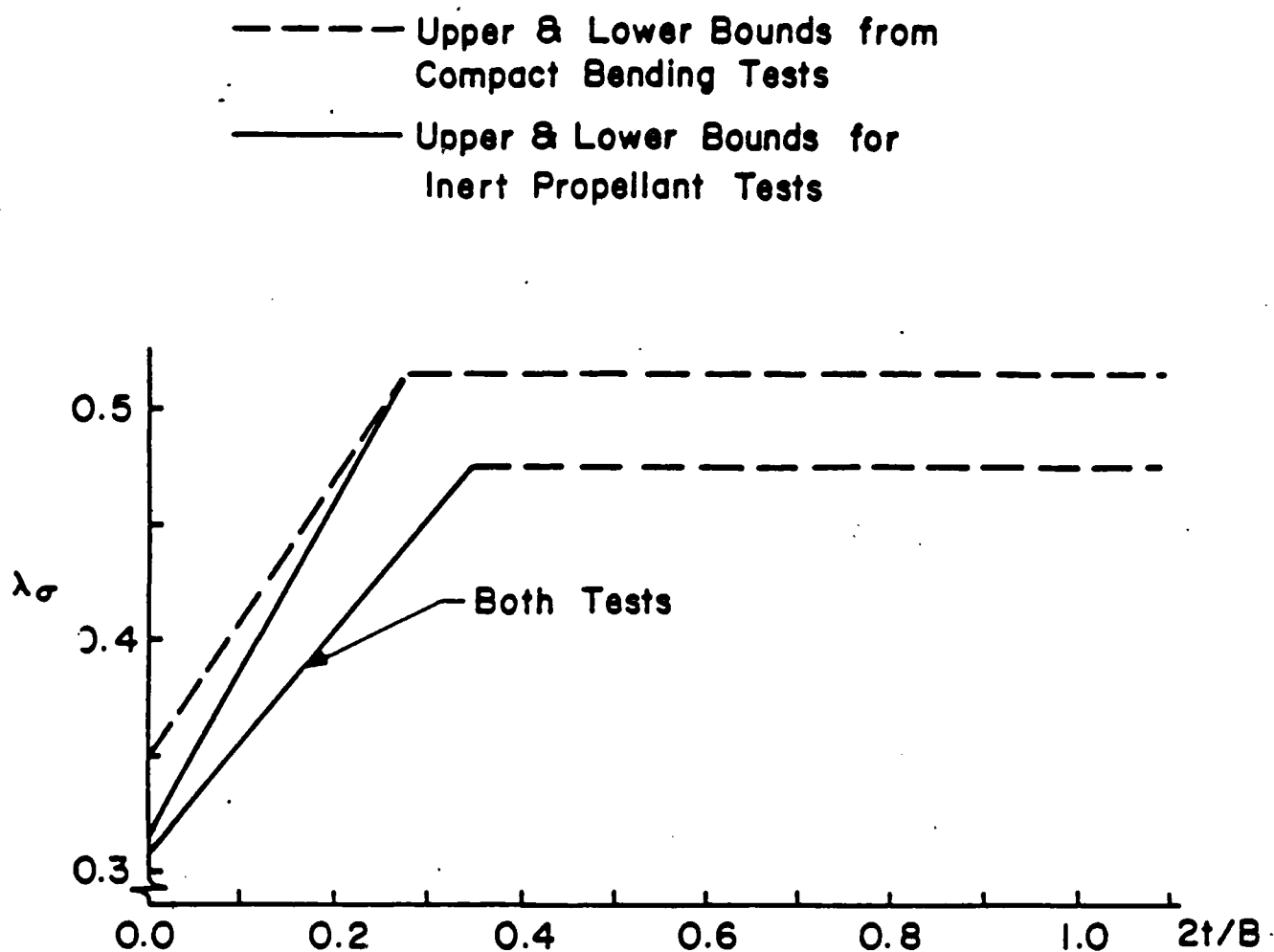


Fig. 21  $\lambda_\sigma$  Distribution for Inert Propellant.

in  $\lambda_u$  for those tests (8 and 9) than might otherwise have been experienced. In any event, it appears that the values of  $\lambda_u$  through the transition zone in the inert propellant biaxial specimens may be slightly lower than in the compact bending polyurethane specimens.

## SUMMARY AND RECOMMENDATIONS

### Summary

The foregoing study consisted of four main parts. These parts and their findings are as follows:

I - Preliminary tests were conducted on transparent polyurethane specimens to evaluate the influence of the free surface effect on the order of the singularity of the biaxial test configuration and the zone dominated by this effect together with the influence of specimen thickness on this effect. Results showed that

i) The zone dominated by the free surface singularity effect exists but is severely reduced by the biaxial specimen geometry and extends from approximately 0.2 to 0.9 mm. in isotropic, homogeneous, nearly incompressible polyurethane.

ii) The influence of the free surface on the stress singularity order at the crack tip is negligible for through thickness data.

iii) Additional observations revealed that:

a) Increasing specimen thickness from 6.4 to 12.7 mm did not alter the values of  $\lambda_u$  in large polyurethane models.

b) Some crack front curvature was observed when crack growth occurred.

c) Crack tip profiles retained a nearly semi-elliptic shape when loaded and revealed no macroscopic evidence of crazing during either opening or growth stages.

II - Preliminary tests were conducted on cracked biaxial inert propellant specimens in order to determine appropriate methods for measuring near tip displacement and strain fields during various constant cross-head displacement rates. The grid method was selected for in-plane displacement measurements and the shadow moire method for out-of-plane measurements. Methods for printing gratings on the inert propellant surface, and instrumentation to record sequential images of the deformed grid and shadow moire fringes were developed. Techniques for data extraction and data reduction were implemented. In addition, a test method for simultaneous determination of U,V and W displacements from a single photograph was demonstrated.

III - Local displacement and strain fields in cracked biaxial inert propellant specimens were determined for 0.2 and 0.6 in. (5 and 15 mm) thick specimens loaded at various cross-head rates from 0.01 to 1.0 in. (0.25 to 25 mm) per minute. No systematic dependence on thickness or loading rate was found. The character of the global fields was established. Local irregularities associated with the heterogeneous nature of the specimen material were abundant.

Strain-rate effects were investigated for the crack opening phase. The deformation accumulates slowly at first and then progressively more rapidly as the specimen is stretched at a uniform rate. This nonlinear response was attributed to a redistribution of local material compliance around the crack, consistent with the model of Appendix H.

IV - Results of extraction of free surface singularity order from measurements on cracked biaxial inert propellant specimen surfaces and inference of its distribution through the thickness from frozen stress results yielded:



i) An average value of  $\lambda_u = 0.69$  over 15 tests with a standard deviation of 0.06 which included global strain levels of 1.5 to 10% and head rates of 0.25, 2.5 and 25 mm/min.

ii) Using frozen stress data from a compact bending specimen of approximately the same thickness as the biaxial specimens, a transition zone for  $\lambda_\sigma$  was found to be about 20% of the specimen thickness over which  $\lambda_\sigma$  varied from 0.31 to 0.50.

These results reveal that, using a continuum approach, the LEFM stress singularity is lost near the free surface of the crack front/free surface intersection point but increases through a transition zone to its LEFM value.

Since the value of the lowest dominant eigenvalue differs from that associated with classical fracture mechanics, one is led to address the issue of how the quantified knowledge of this phenomena can be introduced into the framework of classical fracture mechanics so it can be utilized in engineering analysis. A simple way in which to achieve this is to introduce a stress intensity factor which would be required to produce the same value of  $\tau_{\max}$  as one measures in the actual tests where  $\lambda_\sigma$  is not equal to the classical value. Calling this the corresponding SIF, one may write

$$\frac{(K_{\text{cor}})_{\text{Ap}}}{r^{1/2}} = \frac{(K_{\lambda_\sigma})_{\text{Ap}}}{r^{\lambda_\sigma}} \quad (7)$$

Now, substituting relation (7) into Eq. (C6), one has:

$$\tau_{\max} = \frac{\lambda_\sigma (K_{\text{cor}})_{\text{Ap}}}{\sqrt{2\pi} r^{1/2}} \quad (8)$$

Now, combining Eqs. (B3) and (8), one has

$$\frac{\lambda_{\sigma} (K_{cor})_{Ap}}{\sqrt{2\pi} r^{1/2}} = \frac{K_{Ap}}{\sqrt{8\pi} r^{1/2}} \text{ whence}$$

$$(K_{cor})_{Ap} = \frac{K_{Ap}}{2\lambda_{\sigma}} \quad (9)$$

Since values of  $K$  and  $K_{cor}$  are obtained by extrapolating plots of  $K_{Ap}$  and  $(K_{cor})_{Ap}$  vs  $r^{1/2}$  across a nonlinear zone to the origin, it follows that,

$$K_{cor} = \frac{K}{2\lambda_{\sigma}} \quad (10)$$

It should be emphasized that the introduction of relation (7) is quite arbitrary and is based upon purely dimensional grounds. Moreover, since the analysis here is quasi-two dimensional, one depends on moire results using Benthem's analysis to validate the stress algorithm at the free surface.

Equation (9) then, may be applied in the transition zone to convert the SIF obtained from LEFM into the value which would exist there had the singularity order been 0.5. In the present case:

$$K_{cor} = \frac{K}{2 \times 31} = 1.6K \quad (11)$$

and so  $K_{cor}$  may be viewed as a very conservative way of treating free surface effects. On the other hand, if one is dealing with thickness averaged values instead of surface values, no correction for the effect would appear to be indicated. It should be emphasized that this discussion is based upon a continuum approach.

### Recommendations

The foregoing studies revealed that the location of the zone dominated by the lowest eigenvalue was further from the crack tip in inert

propellant than in polyurethane and that significant changes of material properties occurred in the process zone for propellant but not for the polyurethane. Moreover, severe crack tip blunting occurred in the propellant. Special blunting characteristics were associated with a rubber-rich surface layer on the propellant material. Finally, tests on the polyurethane showed some thumbnailing when the cracks grew. It is recommended that an exploratory study be undertaken using inert propellant material, binder material only and binder material with additive to determine the differences between crack opening and growth mechanisms in these materials and to attempt to extract  $\lambda_u$  values from such tests employing biaxial specimens. The inert propellant material should be machined from bulk stock, rather than cast in plate form, to eliminate the effects of rubber-rich surface layers. It is also recommended that a frozen stress analysis of a thumbnailed crack front simulating that exhibited by a growing crack in inert propellant be undertaken and results be compared with straight front crack results.

#### REFERENCES

- [1] Benthem, J. P., "The State of Stress at the Vertex of a Quarter Infinite Crack in a Half Space," International Journal of Solids & Structures, Vol. 13, pp. 479-492, 1977.
- [2] Smith, C. W., Post, D., and Epstein, J. S., "Measurement of Stress and Displacement Fields Near Crack Tips by Optical Methods," Proceedings of the 40th Anniversary Meeting of the Society for Experimental Stress Analysis (now Society for Experimental Mechanics), pp. 1-6, 1983.
- [3] Jolles, M., McGowan, J. J., and Smith, C. W., "Use of a Hybrid Computer Assisted Photoelastic Technique for Stress Intensity Determination in Three Dimensional Problems," Computational Fracture Mechanics, ASME-PVP, pp. 83-102, 1975.
- [4] Smith, C. W., Olasebikan, O., and Epstein, J. S., "An Analytical-Experimental Investigation of the Linear Elastic Zone for Photoelastic Mode I SIF Extraction," Journal of Theoretical & Applied Fracture Mechanics, Vol. 2, pp. 157-169, Dec. 1984.

- [5] Rooke, D. P., and Cartwright, D. J., Compendium of Stress Intensity Factors, Her Majesty's Stationary Office, London, 1974.

## APPENDIX A INSERTION OF CRACKS IN POLYURETHANE MODELS

A cutter (Fig. A-1) made by shaping and sharpening the edges of a putty knife was forced through the thickness of the model material to make a straight front crack. Slotted aluminum blocks were used above and below the polyurethane to insure that the crack fronts were normal to the specimen surfaces.

## APPENDIX B ALGORITHMS FOR CONVERTING OPTICAL DATA INTO FRACTURE PARAMETERS (LEFM AND $\lambda_u$ UNDEFINED)

In developing algorithms for converting free surface data into fracture parameters, the authors used both linear elastic fracture mechanics (LEFM) concepts and the results of Benthem's analysis (loc. cit.). For benefit of the reader and preservation of continuity both will be briefly reviewed here.

### Mode I LEFM Algorithm for Photoelastic Data

We may describe the near tip stresses in LEFM for two dimensional problems as (Ref. [B1])

$$\sigma_{ij} = \frac{K_1}{(2\pi r)^{1/2}} f_{ij}(\theta) - \sigma_{ij}^0(\theta) \quad i, j = x, y \quad (B1)$$

where  $\sigma_{ij}$  are the near tip in-plane stress components,  $K_1$  is the Mode I stress intensity factor (SIF),  $\sigma_{ij}^0$  may be regarded as the near tip contribution of the non-singular stresses which, experience shows, can be represented as a set of constant values very near the crack tip and  $(r, \theta)$  are polar coordinates as shown in Fig. B-1. Along  $\theta = \pi/2$ , we may compute from Eqs. (B1) [when  $(\sigma^0)^2$  is small relative to  $8\tau_m^2$  [B1]] where  $\sigma^0/\sqrt{8}$  represents the contribution of the non-singular stress state

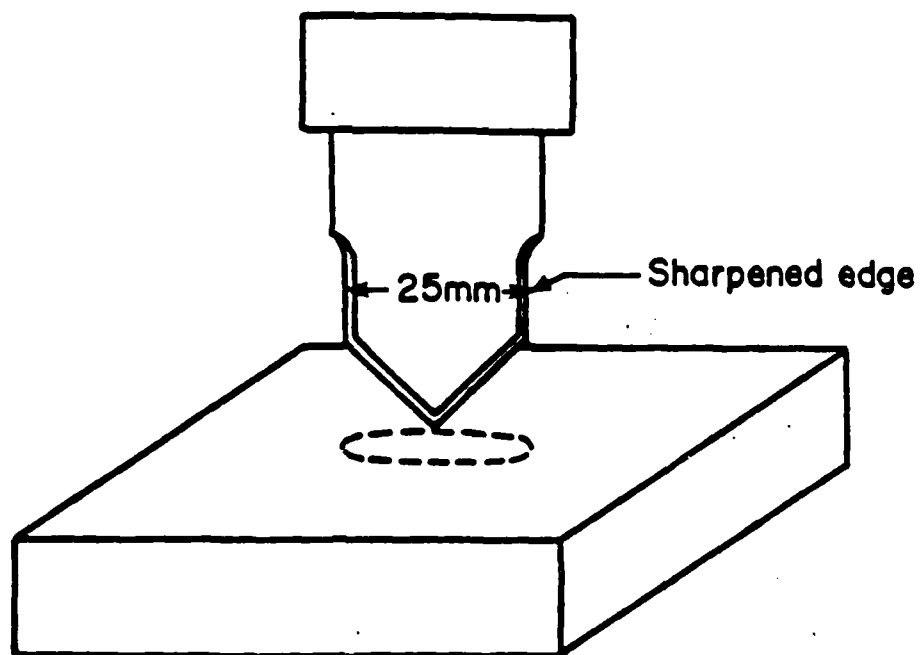


Fig. A1 Method for Inserting Cracks into Polyurethane Models.

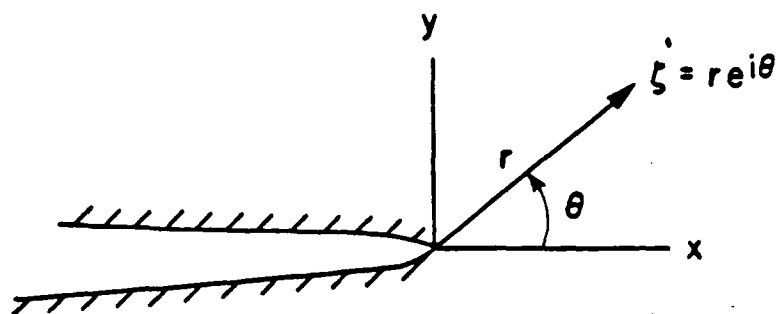


Fig. B1 Near Tip Polar Coordinates.

to  $\tau_{\max}$  locally as:

$$\tau_{\max} = \frac{K_1}{(8\pi r)^{1/2}} + \frac{\sigma^0}{\sqrt{8}} \quad (B2)$$

Now defining an "apparent" SIF,

$$(K_1)_{AP} = \tau_{\max} (8\pi r)^{1/2} \quad (B3)$$

and normalizing with respect to  $\bar{\sigma}(\pi a)^{1/2}$  where  $\bar{\sigma}$  represents the remote stress and  $a$  the half crack length, we have

$$\frac{(K_1)_{AP}}{\bar{\sigma}(\pi a)^{1/2}} = \frac{K_1}{\bar{\sigma}(\pi a)^{1/2}} + \frac{\sigma^0}{\bar{\sigma}} \left(\frac{r}{a}\right)^{1/2} \quad (B4)$$

which suggests a linear zone in a plot of

$$\frac{(K_1)_{AP}}{\bar{\sigma}(\pi a)^{1/2}} \text{ vs } \left(\frac{r}{a}\right)^{1/2} \text{ with a slope of } \frac{\sigma^0}{\bar{\sigma}}.$$

Experience shows this zone to lie between  $(r/a)^{1/2}$  values of approximately 0.2 to 0.4 (or above) in most two dimensional problems. By extracting optical data from this zone and extrapolating across a near tip non-linear zone, an accurate estimate of  $K_1/\bar{\sigma}(\pi a)^{1/2}$  can be obtained. This is illustrated for a large specimen in Fig. B-2. Details of this approach are found in Ref. [B1].

#### Mode I LEFM Moire Algorithm

Corresponding to Eqs. (B1) we have, for displacements for the two dimensional case (Ref. [B2])



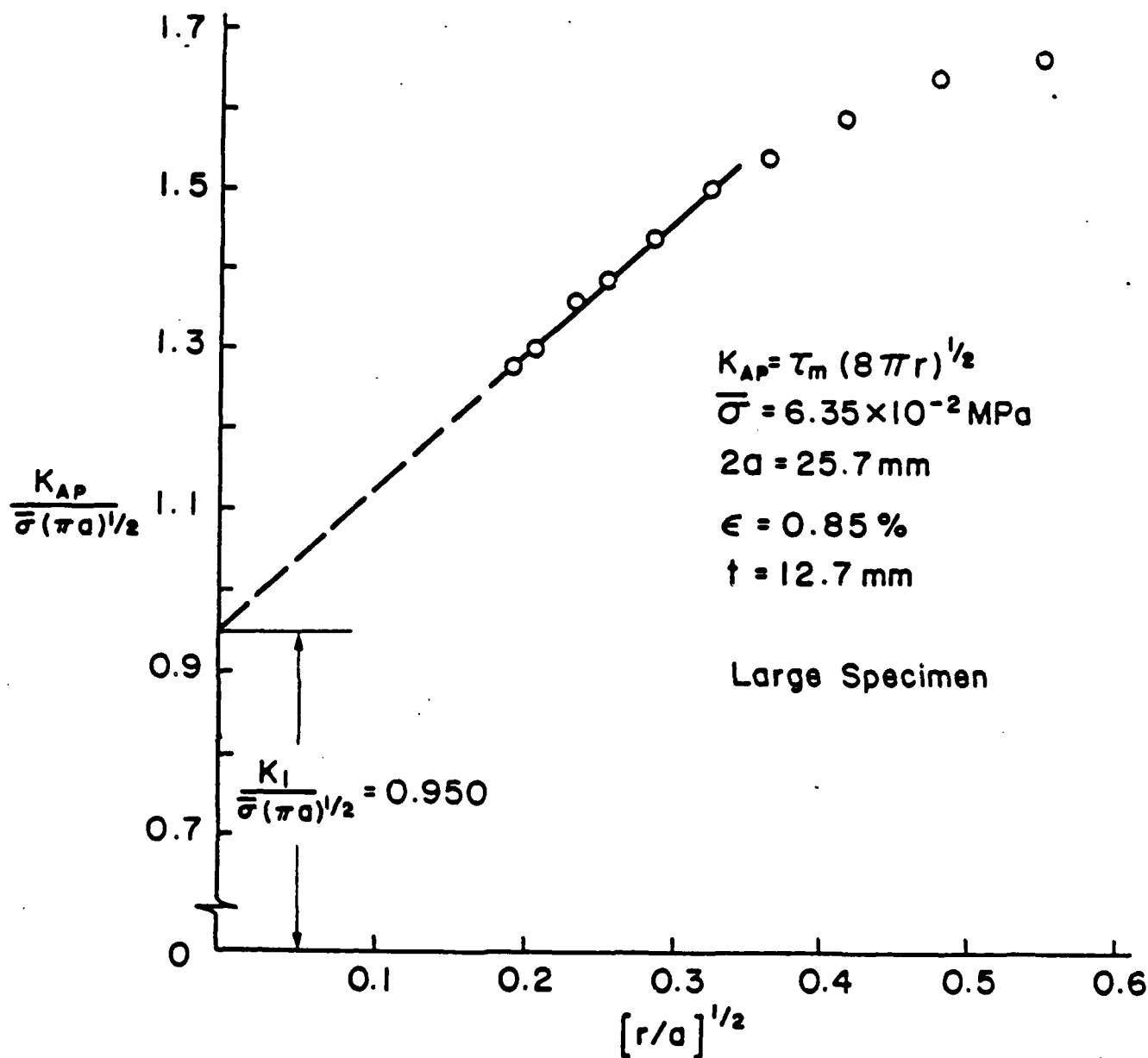


Fig. B2 Determination of Normalized  $K_I$  from Photoelastic Data.

$$\begin{aligned}
 U &= CK_1 G_x(\theta) r^{1/2} - \frac{\sigma^0}{E_s} r \cos \theta \\
 V &= CK_1 G_y(\theta) r^{1/2} - \frac{\sigma^0}{E_s} r \sin \theta
 \end{aligned}
 \tag{B5}$$

where C is a constant containing the elastic constants,  $\sigma^0$  is a non-singular stress term and  $E_s$  is the shear modulus.

In the photoelastic algorithm, we included the effect of the non-singular stress since it was independent of r. However, in Eqs. (B5), we may, for sufficiently small values of r, neglect the effect of the  $\sigma^0$  terms. Thus, along  $\theta = \pi/2$ , we may write,

$$V = C' K_1 r^{1/2} \tag{B6}$$

where a plot of  $V/r^{1/2}$  vs  $r^{1/2}$  should yield a horizontal line with ordinate proportional to  $K_1$ . Sometimes however, the  $\sigma^0$  term does make a contribution in the data zone so we must use the form

$$V = C''(K_1)_{AP} r^{1/2} \tag{B7}$$

and extrapolate to the origin as before a plot of  $V/r^{1/2}$  vs  $r^{1/2}$ .

#### Algorithms for Accounting for Free Boundary Effect on the Crack Tip Singularity at the Free Surface

Following the reasoning in LEFM and focusing only on the leading term in Benthem's series expression for V, we may write directly, along  $\theta = \pi/2$

$$V = D_y r^{\lambda_u} \tag{B8}$$

whence

$$\log V = \log D_y + \lambda_u \log r \quad (B9)$$

so that the slope in the linear zone of a plot of  $\log V$  vs.  $\log r$  will yield  $\lambda_u$ .

### References

- [B1] Smith, C. W., "Use of Three Dimensional Photoelasticity and Progress in Related Areas," Ch. 1 of Experimental Techniques in Fracture Mechanics, 2, Society for Experimental Stress Analysis Monograph No. 2, A. S. Kobayashi, Ed., pp. 3-58, 1975.
- [B2] Eftis, J., Subramonian, N. and Liebowitz, H., "Crack Border Stress and Displacement Equations Revisited," J. of Engineering Fracture Mechanics, Vol. 19, No. 1, pp. 889-210, 1977.

### APPENDIX C ALGORITHMS FOR CONVERTING OPTICAL DATA INTO FRACTURE PARAMETERS ( $\lambda_\sigma$ UNDEFINED)

In developing algorithms for converting frozen stress data into values of  $\lambda_\sigma$ , the authors used both the linear elastic fracture mechanics (LEFM) concepts described in Appendix B and the results of Benthem's analysis (loc. cit.). The developments from the latter results are described below.

#### Photoelastic Algorithms for Accounting for Free Boundary Effect on the Crack Tip Singularity at the Free Surface

Although the above noted effect involves a three dimensional state of stress, one may consider measurements on the free surface itself and within thin layers parallel to the free surface as being associated with a quasi-two dimensional stress state. Thus, one may begin, as in LEFM, with a two dimensional stress function  $f(z)$  the form:

$$Z = \frac{f(z)}{\lambda_\sigma z} \quad (C1)$$

where  $z = re^{i\theta}$  and is measured from an origin at the crack tip (Fig.

B1). Expanding  $f(z)$  in a MacLaurin series about the crack tip and letting  $z \rightarrow 0$  we recover

$$Z|_{z \rightarrow 0} = \frac{K_{\lambda_{\sigma}}}{\sqrt{2\pi} r^{\lambda_{\sigma}}} \quad (C2)$$

where  $K_{\lambda_{\sigma}}$  may be designated as a stress eigenfactor. Now substituting (C2) into

$$\sigma_{xx} = \text{Re}Z - y\text{Im}Z$$

$$\sigma_{yy} = \text{Re}Z + y\text{Im}Z$$

$$\sigma_{xy} = -y\text{Re}Z'.$$

we obtain, using  $\sigma^0$  to account for non-biaxiality of remote loads,

$$\begin{aligned} \sigma_{xx} &= \frac{K_{\lambda_{\sigma}}}{\sqrt{2\pi} r^{\lambda_{\sigma}}} \{ \cos \lambda_{\sigma} \theta - \lambda_{\sigma} \sin \theta \sin(\lambda_{\sigma} + 1) \theta \} - \sigma^0 \\ \sigma_{yy} &= \frac{K_{\lambda_{\sigma}}}{\sqrt{2\pi} r^{\lambda_{\sigma}}} \{ \cos \lambda_{\sigma} \theta + \lambda_{\sigma} \sin \theta \sin(\lambda_{\sigma} + 1) \theta \} \\ \sigma_{xy} &= \frac{K_{\lambda_{\sigma}}}{\sqrt{2\pi} r^{\lambda_{\sigma}}} \{ \lambda_{\sigma} \sin \theta \cos(\lambda_{\sigma} + 1) \theta \} \end{aligned} \quad (C3)$$

where  $\sigma^0$  plays the same role as  $\sigma^0_{ij}$  in LEFM. From Eqs. (C3) one may compute

$$\tau_{\max} = [(\frac{\sigma_{yy} - \sigma_{xx}}{2})^2 + \sigma_{xy}^2]^{1/2} \quad (C4)$$

Now, noting that

$$\frac{\sigma^0 (2\pi)^{1/2} r^{\lambda_{\sigma}}}{K_{\lambda_{\sigma}} \lambda_{\sigma} \sin \theta} < 1$$

and truncating the resulting expression, one obtains:

$$\tau_{\max} = \frac{\lambda_{\sigma} K_{\lambda_{\sigma}} \sin \theta}{\sqrt{2\pi} r^{\lambda_{\sigma}}} + \frac{\sigma^0}{2} \sin(\lambda_{\sigma} + 1)\theta \quad (C5)$$

Along  $\theta = \pi/2$  (C5) reduces to

$$\tau_{\max} = \frac{\lambda_{\sigma} K_{\lambda_{\sigma}}}{\sqrt{2\pi} r^{\lambda_{\sigma}}} + \frac{\sigma^0}{2} \sin(\lambda_{\sigma} + 1) \frac{\pi}{2} = \lambda_{\sigma} \frac{(K_{\lambda_{\sigma}})_{Ap}}{\sqrt{2\pi} r^{\lambda_{\sigma}}} \quad (C6)$$

and for  $\lambda = 1/2$ , the LEFM case, we recover Eq. B2.

Since one expects LEFM to prevail away from the free surface, one can, by assuming  $\lambda_{\sigma} = 1/2$ , obtain  $\sigma^0$  from the slope of a plot of:

$$\frac{(K_1)_{Ap}}{\sigma(\pi a)^{1/2}} \text{ vs } \left(\frac{r}{a}\right)^{1/2} \quad (\text{see Eq. B4})$$

This, in effect determines the value of the non-singular term on R.S. of Eq. (C6).

If we define this term as  $\tau_0$ , i.e.

$$\tau_0 = \frac{\sigma^0}{2} \sin(\lambda_{\sigma} + 1) \frac{\pi}{2} \quad (C7)$$

then Eq. (C7) suggests that  $\tau_0$  may vary if  $\lambda_{\sigma}$  varies. Thus, as one approaches the free surface, one should experience a variation in  $\tau_0$ . LEFM determinations of  $\sigma^0$  show that it begins to change significantly a short distance from the free surface. If one then imposes a linear decrease in  $\tau_0$  from this point to zero for the surface slice, one finds reasonable correlation between the photoelastic and moiré data within the transition zone. Using this approach, and Eq. (C6) in the form

$$\tau_{\max} = \frac{D(\lambda_{\sigma})}{r^{\lambda_{\sigma}}} + \tau_0 \quad (C8)$$

whence

$$\log(\tau_{\max} - \tau_0) = \log D(\lambda_\sigma) - \lambda_\sigma \log r \quad (C9)$$

we may extract values of  $\lambda_\sigma$  in the transition region from a plot of  $\log(\tau_{\max} - \tau_0)$  vs  $\log r$ .

### References

- [C1] Smith, C. W., "Use of Three Dimensional Photoelasticity and Progress in Related Areas," Ch. 1 of Experimental Techniques in Fracture Mechanics, 2, Society for Experimental Stress Analysis Monograph No. 2, A. S. Kobayashi, Ed., pp. 3-58, 1975.

### APPENDIX D CHOICE OF EXPERIMENTAL METHODS

Whole-field optical methods potentially applicable for these deformation measurements include the moire,<sup>1,2,3</sup> grid<sup>4</sup> and speckle<sup>5</sup> methods for in-plane displacements; and shadow moire,<sup>2,3</sup> projection moire<sup>6</sup> and speckle<sup>5</sup> methods for out-of-plane displacements. Durelli offers additional perspective in Ref. 7.

Speckle methods have been applied to various fracture problems, notably by Chiang<sup>5</sup> and coworkers, but the cases treated involved smaller displacements than encountered here. The propellant crack problem involves displacements that are too large to maintain speckle correlation between the before and after deformation images, so speckle techniques are inappropriate.

In-plane moire techniques have advantages for the far-field regions of the propellant-crack specimen. In the near-field, however, the rather large rotations and strains would cause ambiguous results. The fact that the large rigid inclusions create local displacement irregularities would further confuse the moire fringe patterns.

The grid method appears to offer the best features for in-plane measurements. Although more effort is required for data reduction, the

laboratory work for acquisition of the data is comparatively easy. The grid method can be applied in regions of very large extensions and rotations fully as well as regions of modest deformation. The actual surface displacements are sensed independently of irregularities caused by the rigid inclusions. (This quality is distinct from moire, which requires smoothly varying deformations; for a field of irregular deformations, fringe contrast is diminished and ultimately lost as the severity of irregularities increases.) The grid method was selected for this work. Its resolution depends upon the data extraction techniques employed and with the relatively simple techniques used here, the resolution was estimated (in the section Results: Global Deformations) as  $2.5\text{ }\mu\text{m}$  or  $100\text{ }\mu\text{in}$ . Moire with about 2000 lines per inch (80 lines per mm) would be required for equal resolution, and use of such fine gratings would be exceedingly difficult for these tests.

For out-of-plane measurements, the correlation problem again precluded the speckle method. The shadow moire method offers all the needed features, being easy to employ and fitting the needed sensitivity range. It is incompatible with the grid method, however, for simultaneous U, V and W data collection from the same specimen surface. However, it was rationalized in the section Utility of W Measurements that W need not be measured on the same surface as U and V. Consequently, shadow moire data were taken for many tests (Table 2) on the back surface of the specimen.

The projection moire method of W determination is compatible with the grid method, simultaneously on the same surface. An innovative method was developed for simultaneous data collection in a single photograph. The method, described in Appendix G, is somewhat similar to that

of Chiang and Williams<sup>6</sup>. However, they used moire for U and V instead of the grid method; and they used single-beam projection instead of double beam, with consequent reduction of sensitivity.

### References

- [D1] Chiang, F. P., "Moire Methods of Strain Analysis," Manual on Experimental Stress Analysis, Third Edition, A. S. Kobayashi, Editor, SESA, Westport, CT (1978).
- [D2] Durelli, A. J., and Parks, V. J., Moire Analysis of Strain, Prentice-Hall, Inc., Englewood Cliffs, NJ (1970).
- [D3] Parks, V. J., "Geometric Moire," Handbook for Experimental Mechanics, A. S. Kobayashi, Editor, Prentice-Hall, Inc., Englewood Cliffs, NJ, pp. 282-313 (1987).
- [D4] Parks, V. J., "Strain Measurements Using Grids," Optical Engineering, 21(4), pp. 633-639 (July/August 1982).
- [D5] Chiang, F. P., and Wu, X. P., "Three Dimensional Crack-Tip Deformation in a Plastically Deformed Three-point Bend Specimen," Technical Report No. 475, State University of New York at Stony Brook, College of Engineering and Applied Sciences (March 1986).
- [D6] Chiang, F. P., and Williams, R., "Simultaneous Determination of U, V and W of Fracture Specimens," J. Engineering Fracture Mechanics, 22(5), pp. 731-735 (1985).
- [D7] Durelli, A. J., "The Difficult Choice: Evaluation of Methods Used to Determine Experimentally Displacements, Strains and Stresses," Applied Mechanics Update 1986 (ASME), pp. 259-277 (1986).

## APPENDIX E THE GRID METHOD

### Printing the Grid

For printing a grid on the surface of the specimen, the basic tool used in this work is a commercially available metal screen. This is a thin nickel sheet with regularly spaced square openings. These screens are cataloged under the name Electroformed Mesh and sold by

Buckbee-Meers  
245 East 6th Street  
St. Paul, MN 55101

The screens selected for this work were grids of 125 lines per inch and



500 lines per inch (5 and 20 lines per mm). The standard nickel thickness is 0.0001 in. (2.5  $\mu\text{m}$ ), but thicker screens of 0.0003 in. (7.5  $\mu\text{m}$ ) were obtained by special order for this work. The increased thickness makes handling easier. The square openings were wider than the vertical and horizontal metal bars that comprised the screen; the screen has the appearance of the printed grid in Fig. 13.

Several alternative printing processes were used. In all of them, the screen was fixed to the specimen surface to act as a mask or stencil. Reflective material was deposited through the openings in the screen. When the screen was removed, its image appeared on the specimen as bright square dots on the dark (nonreflective) specimen material. The screen could not be reused.

It was necessary to fix the screen in intimate contact with the specimen. In one alternative, the screen was laid on the tacky surface of the specimen and pressed down lightly with a roller. Then an ultra thin film of aluminum was deposited on the surface by high vacuum evaporation. The screen was peeled off to complete the operation.

An equivalent method was used on the non-tacky side. In this case a very thin film of liquid epoxy monomer was applied to the specimen to provide a sticky surface. Then the process proceeded as before.

While this printed grid gave good results, some improvement was desired. Some dark blemishes appeared in photographs in zones where the local slope of the specimen was great, i.e., where a salt crystal rotated out-of-plane as the specimen deformed. The dark blemish appeared because that part of the surface did not reflect light into the camera lens. A higher degree of diffuse reflection was desired so light would reflect in a wide angle of directions.

Titanium dioxide powder has strong diffuse reflection and it was used successfully. In this case, a thin layer of vacuum grease (silicone grease) was spread on the specimen surface and the screen was pressed onto the grease. TiO powder was sprinkled onto the surface, pressed into the openings using a ball of absorbent cotton and excess powder was blown off. When the screen was peeled off, the powder was left stuck to the grease in neat square dots. The results were excellent for 125 line per inch (5 lines per mm) grids, but the method was exceedingly difficult for 500 lines per inch (20 lines per mm).

#### Test Apparatus and Procedure

The experimental arrangement is illustrated schematically in Fig. E1. The specimen with a grid printed on it was installed in a tensile testing machine. It was stretched at a constant, predetermined cross-head speed; the machine was equipped with a strip-chart recorder that graphed the load vs. crosshead displacement curve.

The grid was illuminated by diffuse white light. A 35 mm camera was critically focused on the grid. The camera lens, with 100 mm focal length, was displaced from the camera body using extension tubes to obtain approximately 1:1 magnification. The lens aperture was stopped down to f/8, but the effective aperture was smaller because of the extension tubes. Exposure time was 1/30 second, using Kodak Technical Pan film.

The camera was equipped with a motor drive and successive photographs of the grid were taken while the testing machine stretched the specimen. The photographs were made at predetermined time intervals, using an electronic interval timer to trigger each exposure and advance

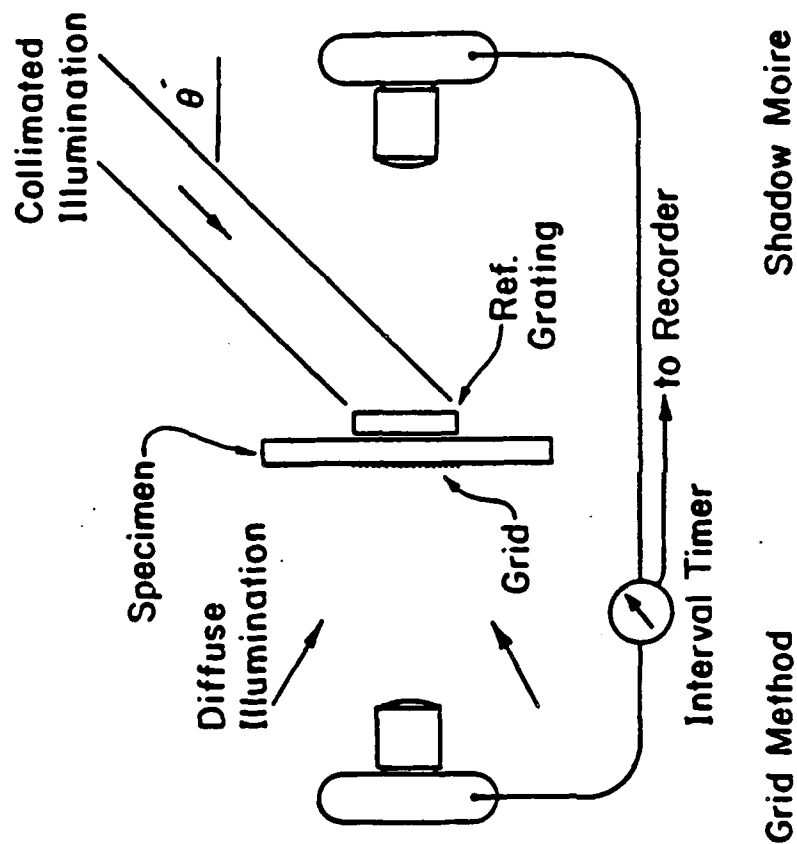


Fig. E1 Experimental arrangement. A sequence of photographs were made simultaneously by the two cameras as the specimen was stretched at a uniform rate.

the film. The interval timer also sent a voltage pulse to the strip-chart recorder; this produced a mark on the load-deflection curve at the instant each exposure was made. The raw data of the grid method is illustrated by Figs. 10 and 13.

The shadow moire tests were carried out simultaneously, as described in Appendix F.

#### Data Extraction

Photographic prints of the deformed grid images were produced with approximately 10 times magnification. The print was fixed to a digitizing table used to measure the x,y coordinates of the grid intersection points. The points chosen are indicated in Fig. 16a. In this operation, a magnifier with a fine cross-hair was positioned manually over the grid intersection point and a button was pressed to transmit the x,y coordinates of the cross-hair to a computer memory file. The digitizing table has a resolution of 0.001 in. (25  $\mu\text{m}$ ), which translates to 0.0001 in. (2.5  $\mu\text{m}$ ) resolution on the specimen scale.

While this procedure is tedious, favorable comments can be made. After initial experience is gained, the time required to digitize one grid pattern was about one hour. The overall effort was small compared to that needed to develop an automated data extraction system. In addition, an automated system would have lower potential for accuracy and reliability, given the variation of line shapes near the intersection points and the blemishes or noise in the photographs.

#### Data Reduction

After digitization, the data for each grid intersection point was stored in computer memory files, viz., the column and row numbers that

identify the point and the x and y coordinates of the point. Computer programs were developed to perform several operations on the data.

These include

- Subtraction of coordinates from two grid systems, to obtain the U,V displacements of points relative to the zero deformation condition (or other previous condition).
- Four-point averaging of displacements.
- Deletion of lines or columns of data to increase gage lengths and affect smoothing.
- Calculation of strains  $\epsilon_y$ ,  $\epsilon_x$  and  $\gamma_{xy}$  using U,V data from 4 points.
- Contouring, to connect points of equal displacement or strain to form contour plots.

The results are illustrated in Fig. 16 as obtained from a printer.

#### APPENDIX F SHADOW MOIRE METHOD

The technique is illustrated on the right side of Fig. E1. A rigid reference grating with opaque bars and transparent spaces is fixed next to the specimen. The oblique illumination beam casts shadows of the opaque bars onto the specimen surface, thus forming a grating of dark and bright lines on the specimen. Light reflected diffusely from the shadow grating passes through the reference grating to the observer (camera). Interaction of the shadow grating and reference grating creates moire fringes, fringes that depict the contour map of the gap between the warped specimen surface and plane reference grating surface.

This map represents the relative out-of-plane displacement of each point on the specimen.

In these experiments, TiO powder was rubbed onto the specimen surface to increase its diffuse reflectivity. The reference grating was held against the specimen by a thin film of vacuum grease. The grease was applied near the ends of the reference grating and squeezed into a thin film to maintain a minimum separation between the grating and specimen; the grease did not extend into the measurement zone. In addition the grating was restrained from vertical translation by a frame attached to the lower (fixed) grip.

The relationship defining out-of-plane displacements  $W$  is

$$W = \frac{P}{\tan \theta} N = \frac{1}{f \tan \theta} N \quad (F1)$$

where  $P$  is the pitch of the reference grating,  $f$  is its frequency,  $\theta$  is the angle of illumination (Fig. E1) and  $N$  is the fringe order in the moire pattern. In practice  $W$  must be interpreted as the relative displacement between points on the specimen, since there is no accounting for the arbitrary initial gap.

In this work,  $f$  was 20 lines per mm and  $\theta$  was  $45^\circ$ . The sensitivity  $W/N$  was 0.05 mm (0.002 in.) per fringe order. An example of the shadow moire fringe pattern is given in Fig. 11.

#### APPENDIX G U,V,W METHOD

This method captures the information needed for whole-field determination of  $U$ ,  $V$  and  $W$  in a single photograph. As before, the specimen is prepared with a 125 lines per inch (5 lines per mm) grid, using the TiO powder method. Double-beam projection moire is used to create a low

visibility moire pattern of  $W$  on the specimen. A photograph records this pattern on a background of the deformed grid, as shown in Fig. G1. The  $U$  and  $V$  displacement information can be extracted exactly as described in Appendix E. The  $W$  information is extracted by optical filtering, using the negative from which Fig. G1 was printed.

The experimental arrangement is illustrated schematically in Fig. G2(a). The specimen is illuminated by symmetrical beams  $A$  and  $B$ . These beams do not have constant intensity across their widths, but instead they exhibit closely spaced dark and bright stripes. These stripes are projected onto the diffusely reflecting specimen and they are photographed by the camera. The stripes are called projected gratings. The two projected gratings from  $A$  and  $B$  form a moire pattern of  $W$ . It is a moire pattern of intensity addition (G1), however, which inherently has poor visibility until the optical filtering process is used.

The method used to form the projected gratings is illustrated in the figure. Here, light from a laser is expanded into a conical beam. It passes through a subsystem comprised of the beam-splitter cube  $BS$  and mirrors  $M1$  and  $M2$ . When the mirrors are parallel to their adjacent cube faces, light propagates toward the parabolic mirror as a single diverging beam. However, when  $M1$  is rotated, two separate beams emerge, one shown by solid lines and the other by dashed lines. The two beams are collimated by the parabolic mirror, but they retain their angular separation  $\alpha$ . Since the two beams are mutually coherent, they combine in constructive and destructive interference. The interference fringes are perpendicular to the plane containing angle  $\alpha$ . Their frequency (fringes per unit length) is proportional to  $\alpha$  when  $\alpha$  is small. The direction and frequency of fringes are easily adjusted by rotation of mirror  $M1$ .

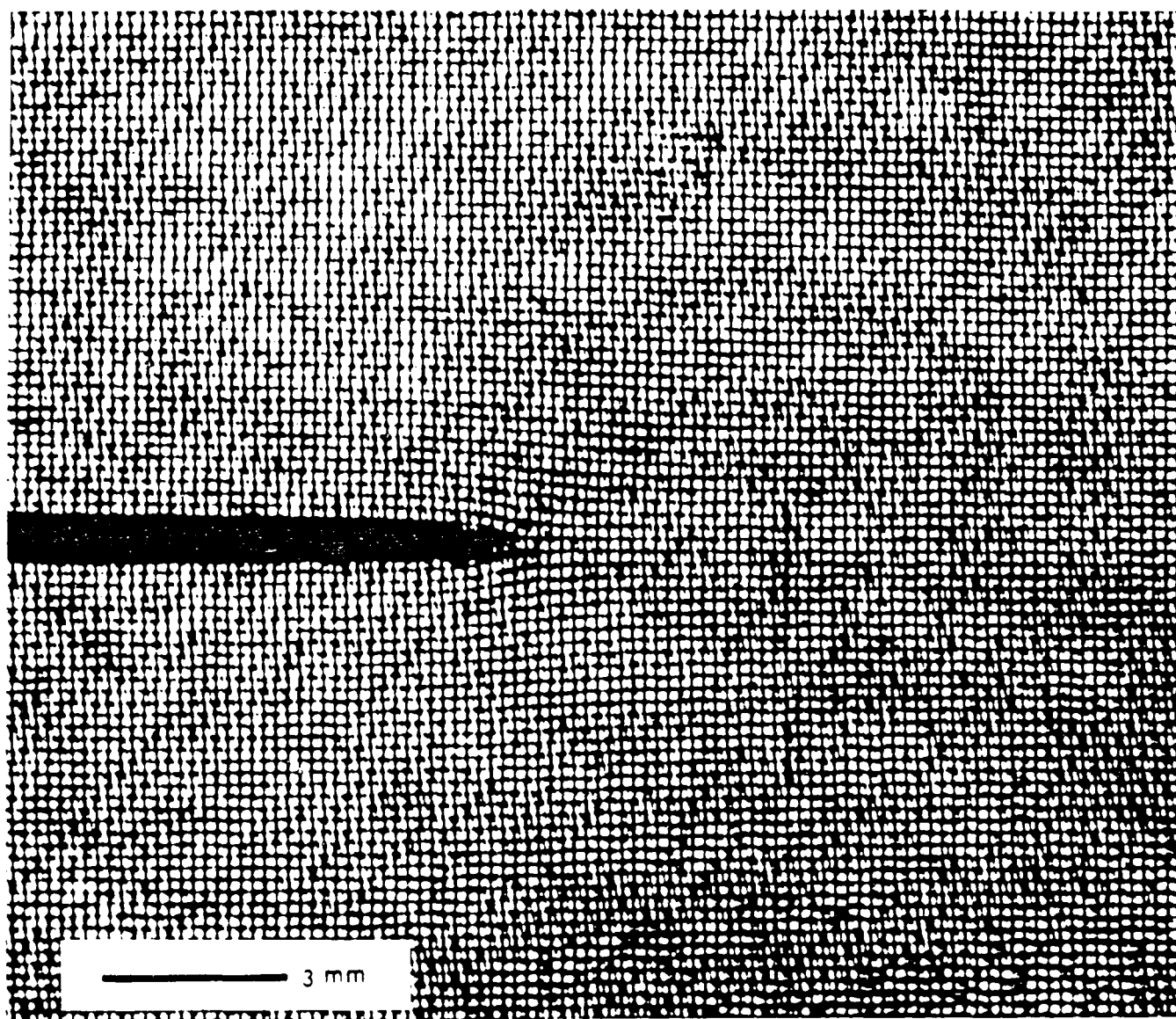


Fig. G1 Deformed grid and projection moiré record.



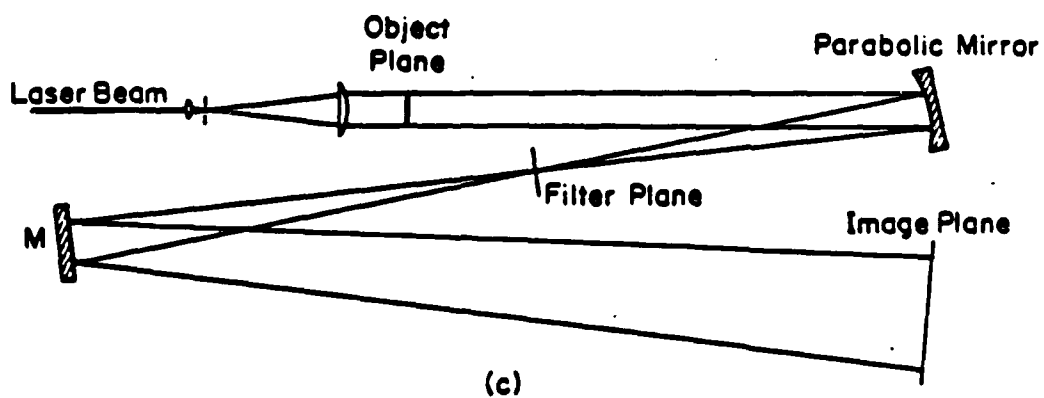
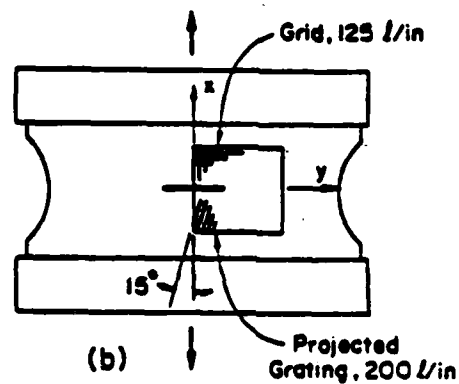
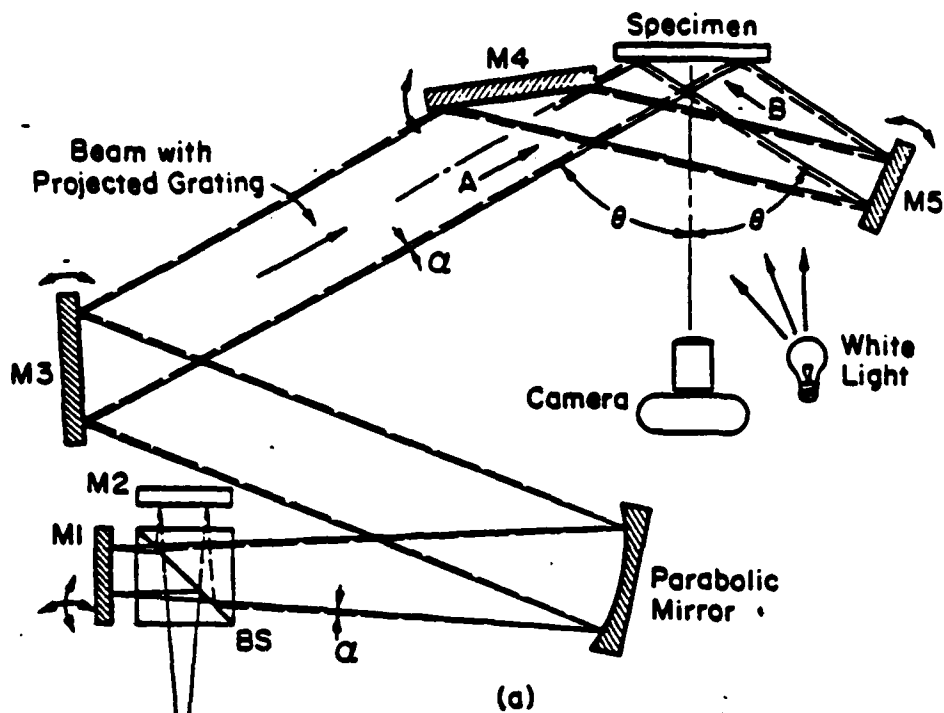


Fig. G2 (a) Experimental arrangement for U,V,W method. (b) Specimen with grid lines and projected grating. (c) Optical filtering arrangement.

The grating frequency that appears on the plane of the specimen depends also upon angle  $\theta$ . In this work the frequency of the grating projected on the specimen was 200 lines per inch (8 lines per mm) and its orientation was  $15^\circ$  from the y axis, as illustrated in Fig. G2(b). This frequency and angle were obtained by adjusting mirror M1.

Mirrors M4 and M5 are used to project the second grating on the specimen. When the angle of B is symmetrical to A, the frequencies of the two projected gratings are equal and a null field is achieved. The adjustment is difficult, however, since gratings of 200 lines per inch (8 lines per mm) cannot be seen with the naked eye, and since the moire fringes are virtually invisible. An indirect technique was used in this work, but a practical means of adjusting beam B to achieve an initial null field is to view the moire fringes using a television camera and a monitor screen adjusted for high contrast. The specimen should be viewed at sufficiently high magnification to resolve the individual lines of the projected gratings on the monitor screen. Mirrors M4 and M5 should be adjusted in this operation, not M1, to achieve a null field prior to deforming the specimen.

An auxiliary white light source is used to take the photographic exposure. This enhances the visibility of the grid in the photograph. The intensity of the auxiliary light was adjusted during trial exposures to achieve a good balance between the grid visibility (for U and V) and the projected moire information.

The optical filtering arrangement used in this work is illustrated in Fig. G2(c). The negative to Fig. G1 was placed in the object plane; its enlarged image, focused by the parabolic mirror, appeared in the image plane. A camera back was located in this plane to record the filtered image on photographic film.

The negative placed in the object plane contained an image of the projected gratings. This image is itself a grating, capable of diffracting the transmitted light. Light from each of its diffraction orders appeared in the filter plane as bright spots, uniformly spaced along a 105° line (perpendicular to the 15° projected grating lines). Light from the +1 diffraction order was allowed to pass through an aperture (or hole) in an opaque screen placed in the filter plane. All other light was obstructed. This light carried the projected moire pattern (the W field), with enhanced contrast, to the film plane. The result is illustrated by Fig. 12. This is a contour map of the out-of-plane displacement of the specimen surface, showing its global deformation plus irregularities caused by local elements of the heterogeneous material.

Light was also diffracted by the grid lines present in the negative (object plane). These diffractions appeared as spots in the filter plane, but the spots were sufficiently distant from the aperture to be obstructed, or filtered, out.

The basic sensitivity is twice that of the shadow moire method. Displacements  $W$  are related to fringe orders  $N$  by

$$W = \frac{1}{2f \tan \theta} N \quad (G1)$$

where  $f$  is the frequency of projected grating lines on the specimen surface. In this work,  $f$  was 200 lines per inch (8 lines per mm) and  $\theta$  was 65°, to yield a sensitivity  $W/N$  of 0.0012 inches per fringe order (0.03 mm per fringe order).

## References

- [G1] Parks, V. J., "Geometrical Moire," Handbook for Experimental Mechanics, A. S. Kobayashi, Editor, Prentice-Hall, Inc., Englewood Cliffs, NJ, pp. 282-313 (1987).

## APPENDIX H PHENOMENOLOGICAL ANALYSIS OF CRACK OPENING AND GROWTH

### Introduction

Many qualities of crack opening and growth cannot be observed directly, but can be inferred from the experimental evidence. A process of observations and self-consistent deductions was undertaken and reported in this section. Because of the random nature of the material -- random orientations and spacings of the inclusions -- one can only generalize on its behavior. The interpretation is intended to represent typical behavior, while fully realizing that diverse variations are present.

Specimen 1 exhibits the characteristics to be discussed. Its deformation, depicted by Fig. 13, will be used as an example.

### Crack Blunting

Figure 13a shows the progress of crack opening and blunting as the specimen is stretched. Image (g) shows the last phase of blunting on the specimen surface prior to void formation and crack extension. The material adjacent to the blunt end of the crack suffers very large elongations. The zone of very large elongations extends ahead of the crack, essentially as an equilateral triangle with the blunt crack tip as its base.

The deformation of the surrounding material is qualitatively evident from observation of the grid and quantitatively from Fig. 16. Above and below the crack lips, deformations are very small. Finite

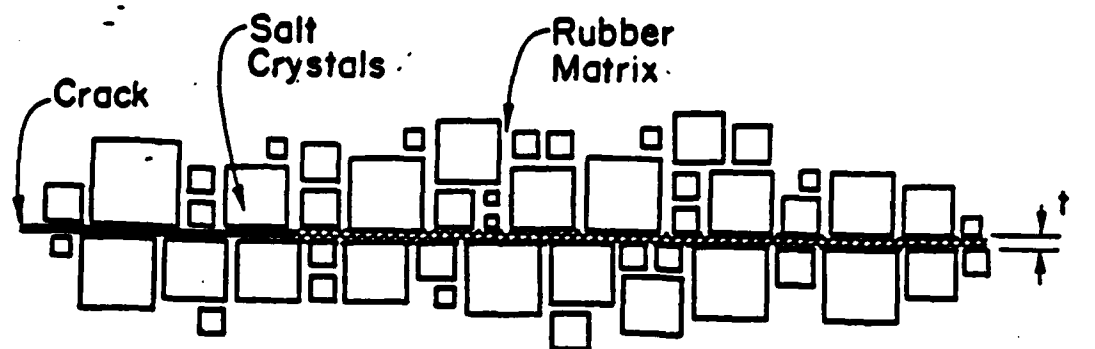
strains appear in the region surrounding the triangular zone, where extensions ( $\epsilon_y$ ) and shears ( $\gamma_{xy}$ ) are of the order of 30%. These are average strains reflecting the integrated deformation of the compliant rubber and stiff (virtually rigid) inclusions.

An explanation or model consistent with the experimental observations is proposed below.

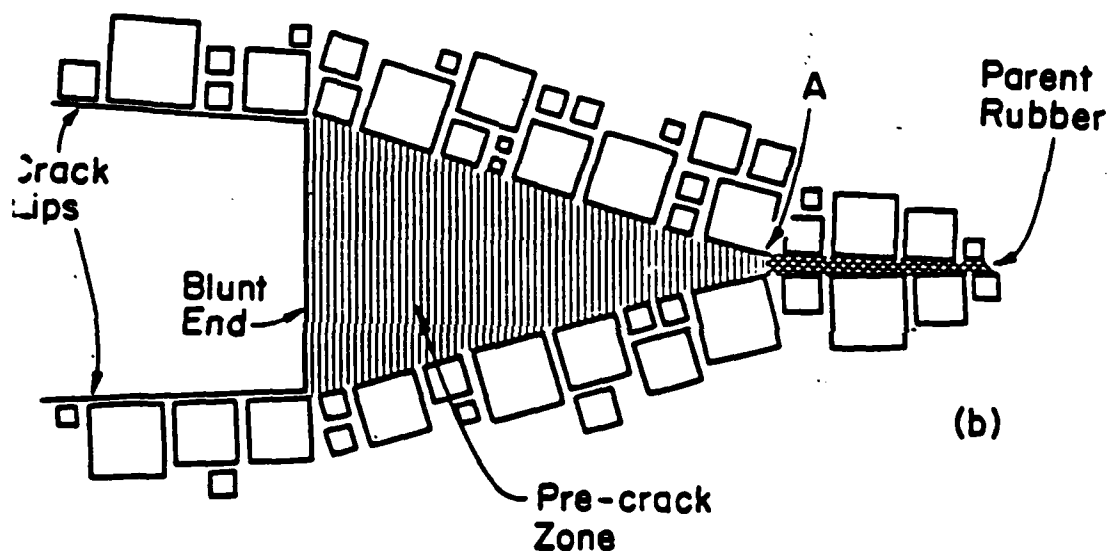
#### Localization of the Pre-crack Zone

Figure H1 is an idealized schematic view of the deformation process. The original crack with zero opening is shown in (a). Crystals of salt are illustrated as squares along the crack boundary and along a path ahead of the crack. This representation is idealized inasmuch as the crystals are given an orderly alignment and spacing; in addition, the secondary system of rigid inclusions are not illustrated. The salt crystals are surrounded by the rubber matrix, which occupies all the space not occupied by the crystals. The thickness of the rubber is exaggerated, too. The largest crystals in the inert propellant are cubes with faces more than 0.4 mm wide, more than twice the pitch of the grid in Fig. 13, whereas the thickness of the rubber is very much smaller.

As the specimen is stretched (perpendicular to the crack plane), the rubber immediately ahead of the crack suffers the largest normal strain  $\epsilon_y$ . The basic thesis here is illustrated in Fig. H1: the thin cross-hatched zone in (a), consisting of a continuous path between crystals, is extended to form the triangular zone shown in (b). This will be called the pre-crack zone, since the crack will subsequently grow into this zone. The material in this triangular zone is capable of



(a)



(b)

Fig. H1 (a) Rubber matrix material along a single path ahead of the crack is (b) subsequently transformed to pre-crack material. Thickness  $t$  is of the order of  $10\text{ }\mu\text{m}$ , and the blunt-tip height is about  $1\text{ mm}$ . The width of the largest crystals is greater than twice the grid pitch in Fig. 11. The normally random distribution of crystals is given an idealized arrangement.

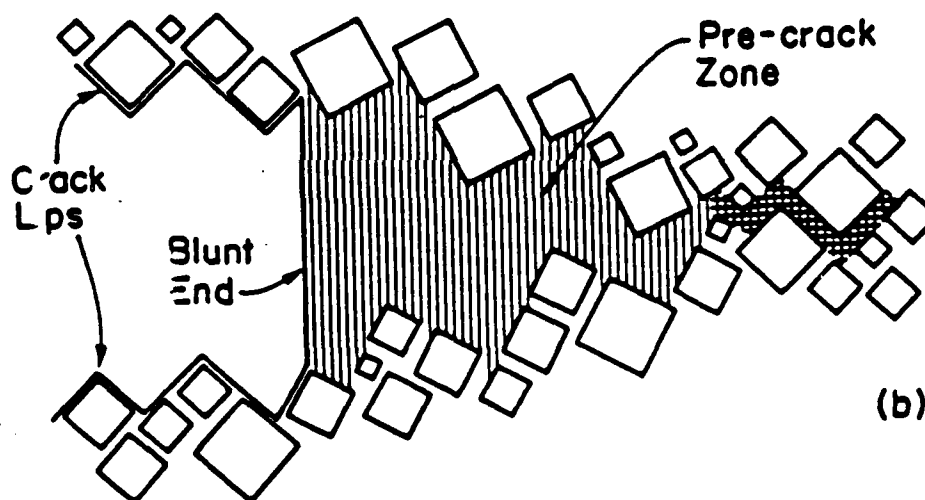
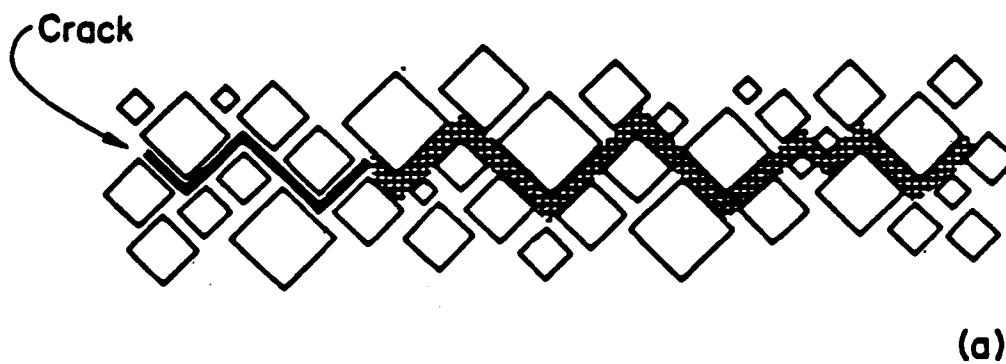


Fig. H2 (a) Crack path and (b) pre-crack zone for another idealized, orderly arrangement of crystals.

sufficiently large extension that parent rubber outside the zone is not required to share the burden of very large extensions.

Figure H2 illustrates another idealized geometry, in which the crystals are oriented  $45^\circ$  to the crack plane. With this distribution of crystals, the crack itself must have jagged lips, essentially as shown. The matrix material in the jagged path shown by crosshatching spreads out to form the pre-crack zone.

The orientations and spacings of inclusions in the real specimen material is far more random. Nevertheless, the inclusions are surrounded by matrix rubber, and continuous paths of rubber analogous to those illustrated here, exist for any configuration. The thesis remains the same: the triangular pre-crack zone is formed from rubber that occupied a single narrow path between inclusions.

#### Rubber-rich Surface Layer

The specimen material used here was cast as plates of uniform thickness and the specimens retained the original as-cast surfaces. These surfaces were rich in rubber, with a much smaller concentration of salt crystals and other particles than the interior. The thickness of the surface layer appears to be about 0.1 mm on the tacky surface of Specimen 1 (see Table 2). The rubber-rich layer was thinner on the non-tacky surface of the specimen material, approximately  $1/4$  to  $1/2$  as thick.

#### Auxiliary Observations

When the specimen material is cut or fractured, salt crystals appear imbedded in the fracture surface. They can be pried out easily



with a sharp pick and the crystals usually emerge with clean surfaces. In only a few cases, rubber remains attached to the crystal after it is pried out. The implication is that the bond strength between the rubber matrix and salt crystals is low -- the tensile strength and shear strength of this bond is smaller than the cohesive strength of the rubber.

Observations were made with a bar of the inert propellant cut from the sheet and loaded as a beam in bending. The maximum tensile stress was developed at the cut surface; the bending forces were parallel to the rubber-rich surfaces of the material. The beam was bent and viewed with magnification on the tensile side. At a sufficient tensile strain, separation occurred between the rubber and one side of some crystals. This formed voids which, in the case of the larger crystals, were easily seen. The voids became wider in the direction of the tensile stress as bending proceeded. Subsequently, the rubber walls between neighboring voids ruptured and a crack was formed on the specimen surface. The crack penetrated into the beam and at some depth, narrow ligaments of rubber could be seen spanning the width between the lips of the crack. The crack grew deeper as the beam was bent, and this growth proceeded by rupture of these ligaments and creation of new ligaments (between voids) at greater depths.

The rubber-rich surface layers also ruptured as the crack width and depth increased. However, this rupture lagged the ruptures of ligaments; the depth of the crack at the rubber-rich surface was typically less than the depth at which interior ligaments appeared. The magnitude of the lag was greater on the tacky thicker rubber-rich surface and smaller on the opposite side -- the nontacky thinner rubber-rich surface.

### Failure Process

The foregoing observations used flexural specimens so that the failure process could be viewed from a direction perpendicular to the crack front. While the specimen geometry was different, the basic features of failure are believed to be the same as those in the biaxial tension tests.

Figure H3 illustrates the hypothesized fracture process in the biaxial specimen of Fig. 13, for a highly idealized crystal arrangement. In (b), the pre-crack zone is characterized by large voids and narrow ligaments separating the crystals. The matrix rubber is separated from opposing horizontal faces of the crystals to form elongated box-shaped voids. The rubber is also unbonded from the vertical sides of opposing crystals and this material is stretched to form the ligaments and the extended surface layer. The voids are closed cells, i.e., the ligaments are hollow tubes of matrix rubber. In (c) the crack opening is great enough to cause rupture of ligaments but the stretched surface layer is intact. With greater crack opening (d) the surface layer is ruptured and the rubber relaxes back to approximately its original shape.

Figure H4 illustrates an internal section of the specimen. The separate conditions of Fig. H3 occur at different regions of the specimen, identified here by corresponding letters in parentheses. The ligaments appear as very narrow zones, but a three-dimensional view would show them as thin walls of elongated tubes.

In Fig. H4, notice the two tiny crystals located between two vertical elements of rubber. For such a case, stretching of the surrounding rubber matrix would carry the lower crystal down into the triangular pre-crack zone. The presence of crystals in the ligament zone was not detected, however, in microscopic inspections.

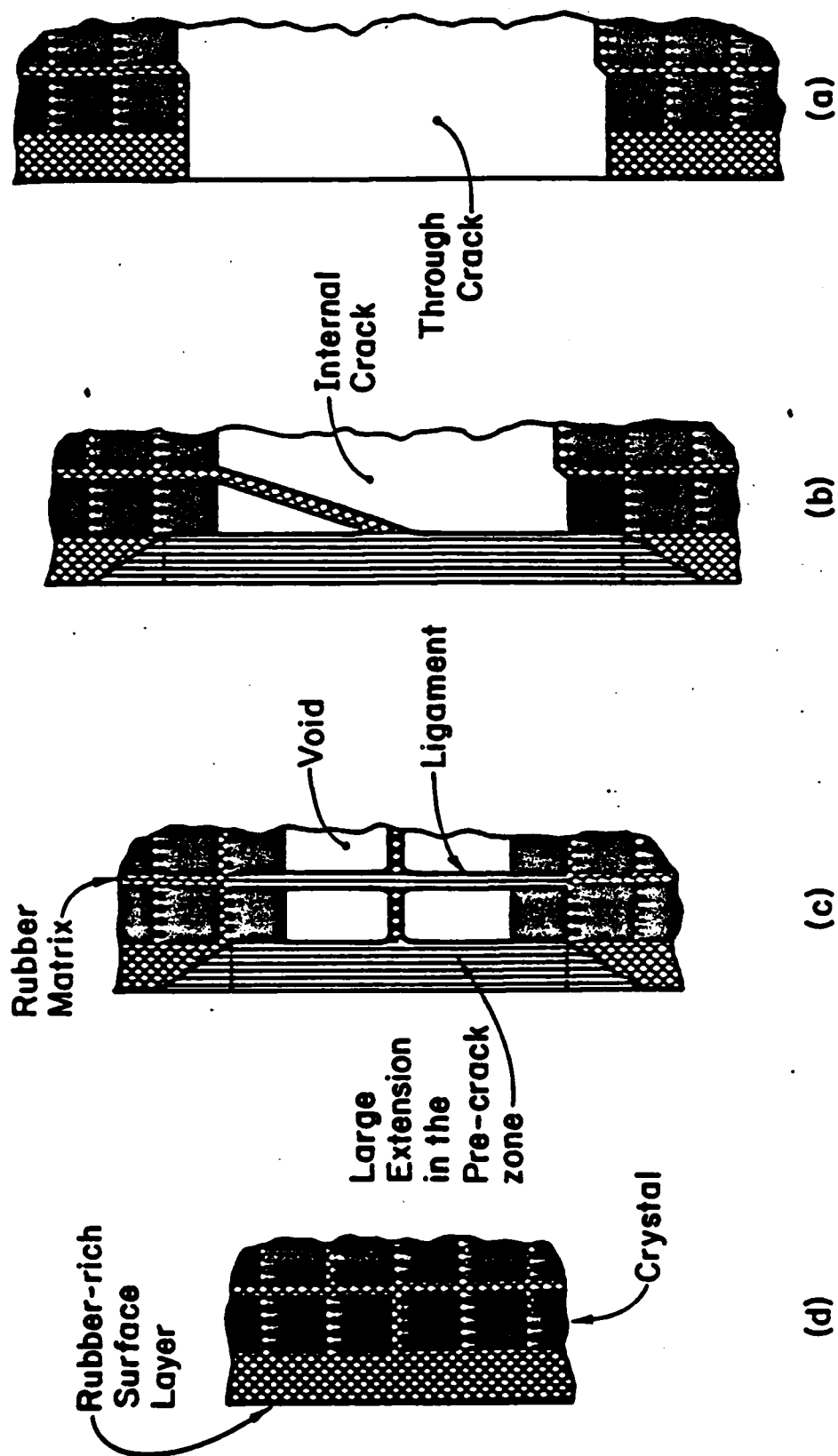


Fig. H3 (a) Cross-sectional view of the specimen material with an idealized crystal arrangement; (b) Pre-crack zone with voids and ligaments; (c) internal crack prior to rupture of rubber-rich layer; (d) through crack with rubber relaxed into its original configuration.

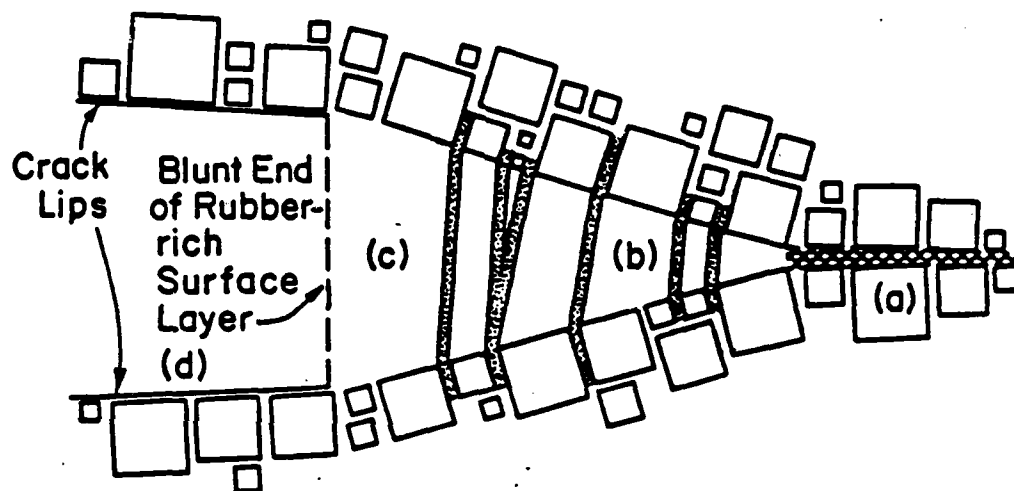


Fig. H4 Interior ligaments and a rubber-rich surface layer span the pre-crack zone. Letters indicate sections in Fig. H3.

An important question arises: Why is the crack end so blunt? If the shear strength between the rubber and crystals is low, why doesn't the rubber-rich surface layer act independently as a thin sheet of rubber, which would form an elliptical-shaped crack opening? The answer lies in Fig. H3(c). While the surface layer debonds from the vertical sides of the opposing crystals, it remains connected to the horizontal elements of rubber matrix. This keys the surface layer to the crystals on both sides of the pre-crack zone and it stretches between these points to form the nearly straight crack tip.

Referring to Fig. H3 (b and c), take note of the triangular portions of the rubber-rich surface layer. Strains in the surface layer can change rather abruptly near the crystals, where the rubber is keyed. Elsewhere in the surface layer, the strains must change in a smooth transition from the smaller strain in the cross-hatched region to the larger strain in the vertically-hatched region. This transition occurs in the triangular portions of the rubber-rich layer.

Some numerical values will help give perspective to these conditions. Crystals exceeding  $400\text{ }\mu\text{m}$  in width were found in abundance in the material. Assume a representative size of all crystals is  $100\text{ }\mu\text{m}$  and assume a uniform array of  $100\text{ }\mu\text{m}$  cubical crystals, each crystal surrounded uniformly by the rubber matrix. For 75% volume fraction of crystals, the thickness of the rubber matrix is calculated as  $10\text{ }\mu\text{m}$ . The cross-sectional areas of rubber and crystal are in the ratio 1:5, or 1/6 the total area is rubber.

The thickness of the rubber-rich surface layer (on the tacky side) is about equal to the representative cube width. The crack blunting in Fig. 13a (image g) is about 1 mm. If the conditions of Fig. H3(b)

prevail, the extended length of the surface layer is 1 mm plus two crystal heights, or 1.2 mm; its original length [Fig. H3(a)] is 0.2 mm. The simple tensile strain in the surface layer at the blunt end is  $\epsilon_y = 5$  or 500%. This is reasonable.

A similar model of voids and connecting ligaments is described in Ref. H1 by Bills and Blatz. They remark, however, that certain data challenges the theory. Whereas the tensile strength of the material would be expected to decrease with the volume fraction of inclusions, they found essentially constant strengths of HTPB propellant, independent of the volume fraction. This factor remains unexplained. Similar tensile tests were not conducted for the present inert propellant.

#### Force Transfer

Different mechanisms of force transfer should exist in the triangular pre-crack zone (including regions immediately surrounding this zone) and the remaining regions. Remote from the high strain regions, one could reasonably hypothesize that debonding between crystals and matrix rubber does not occur. The condition is modeled, ideally, by Fig. H3(a). Under a vertical tensile force, the vertical matrix elements are restrained from stretching by the adjacent rigid crystals. The horizontal matrix elements become thicker, or exhibit a local strain  $\epsilon_y$ . This accounts for some small average strain in the composite material.

At a higher strain level, bonds fail at the horizontal crystal-matrix interfaces. This is because of strong triaxial tensile stresses developed adjacent to the rigid crystals, as in the classical poker-chip test; the rubber cannot respond with a change of its volume and failure must occur.

At still higher strain levels, debonding occurs by shear at the vertical interfaces between crystals and matrix. Subsequent strain is accommodated by stretching of these vertical rubber elements, while the horizontal elements remain unloaded.

A progression is prescribed in which load is carried exclusively by horizontal matrix elements at first and later exclusively by vertical elements. Strains vary accordingly. In low strain regions, the vertical tensile load is carried on a continuous horizontal path of rubber of area  $A$ . In high strain regions the load is carried by the vertical matrix elements only, whose representative area is estimated in the previous section as  $A/6$ . Tensile stress accumulates with tensile load six times faster in the pre-crack zone than in the low strain zone. The highly nonlinear load-displacement curve of Fig. 10 reflects this quality.

What condition exists immediately adjacent to the triangular pre-crack zone, where the average strains are of the order of 30%? With the representative 10:1 crystal to matrix widths, an assumption that the strain is concentrated in the horizontal rubber elements of Fig. H3(a) is unreasonable; since the crystals are rigid, this would lead to strain  $\epsilon_y$  in the rubber exceeding 300%. Instead, the strain must represent 30% change of length of the vertical matrix elements. This requires debonding from the rigid crystals and also void formation along the horizontal crystal faces. The condition would be represented by Fig. H3(b) where the voids are much smaller, viz., void height about 30% of crystal height. In this zone, like the pre-crack zone, force transfer is through the vertical matrix elements.

While these generalizations are developed for an orderly array of crystals, it appears reasonable that they apply in principle to random arrays and to the specimen material.

### Crack Growth

Figure 13b shows a long sequence of crack growth for the same specimen as Fig. 13a. The fixed parameter was cross-head speed, or rate of separation of the specimen grips. The load on the specimen was decreasing monotonically as shown in Fig. 10.

In Fig. 13b [images (a)-(d)], two voids appear in the pre-crack zone, but they subsequently become part of the main crack by disappearance of material to their left. In images (e)-(h), the pre-crack zone advances along an oblique path and voids are formed which subsequently coalesce with the main crack. In images (i)-(l), a new pre-craze zone is formed at a small distance from the main crack; voids form and enlarge, but they are separated from the main crack by a bridge. The bridge continues to stretch until image (m); by that stage the bridge material has failed and disappeared, and a new pre-crack zone has formed at the blunt end of the crack. In images (n)-(p), we see another episode of crack extension and void formation. The dramatic qualities revealed by the sequence of photos are huge shear strains, void formation and coalescence, path changes and bridging. These will be rationalized in the following sections.

### Oblique Paths and Shear Strains

The pre-crack and subsequent crack can extend along an oblique path, as seen in Fig. 13b, images (e)-(h). Figure H5 illustrates the mechanism consistent with the observations and the stated thesis.



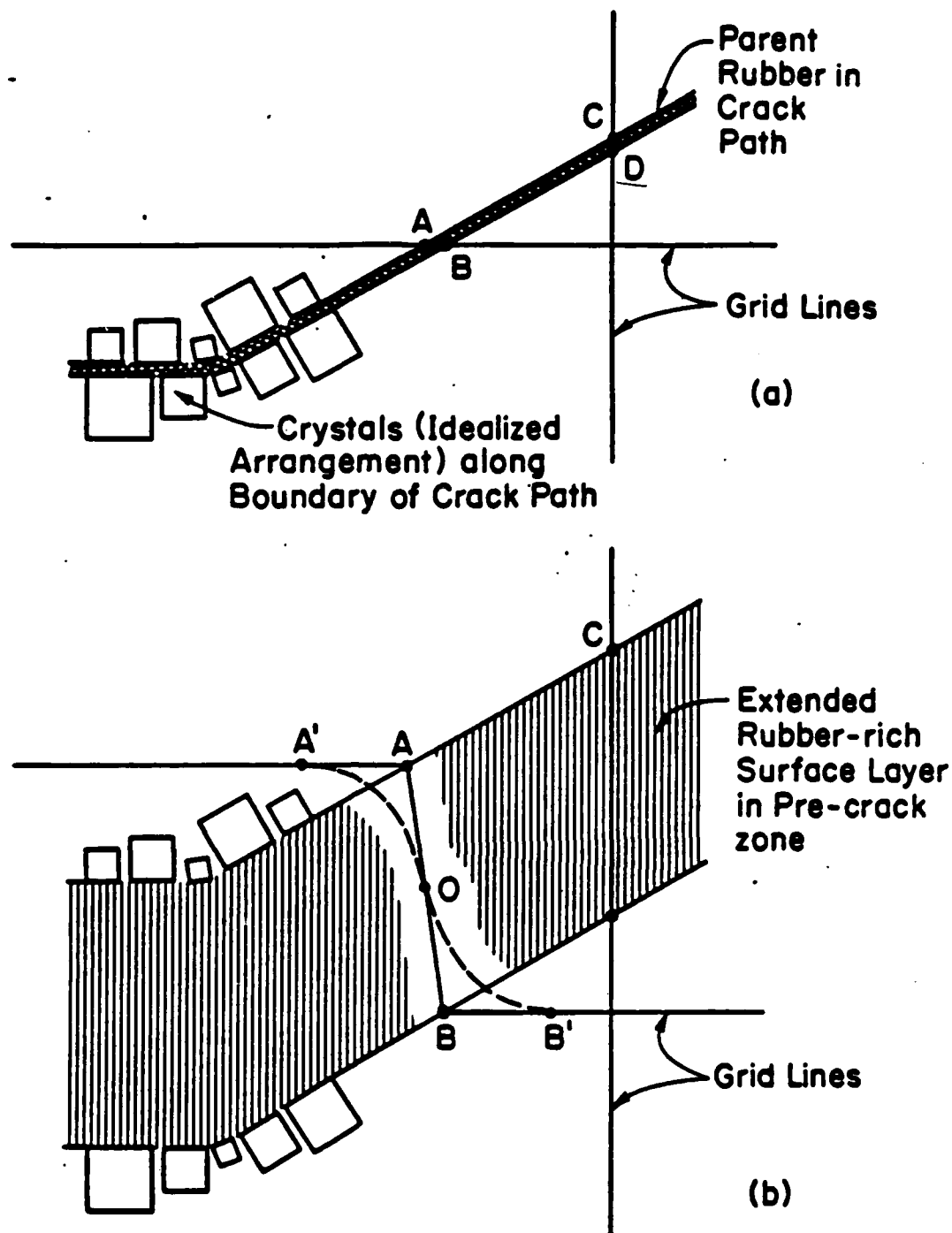


Fig. H5 (a) Inclined path and (b) subsequent pre-crack zone. Because the rubber-rich surface layer spreads the region of deformation, a horizontal grid line distorts as  $A'O'B'$  instead of  $AOB$ .

Again, the pre-crack zone is created by a vertical translation that separates the upper and lower boundaries of the vertically translated crystals. A horizontal and a vertical grid line are shown crossing the crack path in (a) and the pre-crack zone in (b). The original positions of points A and B are changed by a relative displacement equal to the vertical translation; similarly, C and D are displaced vertically. One would expect to see sharp discontinuities in the horizontal grid line, as illustrated by the full line in (b). This represents the deformation presumed to exist in the crystals.

The surface deformation is different, however, as a result of the rubber-rich surface layer. Referring again to Fig. H3(b and c), large deformations on the outside surface do not commence opposite the translated crystal boundaries, but at points above and below the boundaries. This means that large vertical displacements commence at some point A' in Fig. H5b, a point outside the pre-crack boundary. The vertical displacement builds up more gradually on the outside surface; consequently, the originally horizontal grid line dips down gradually along path A'O, and it recovers its horizontal slope gradually along path OB'.

This dramatic curvature of the initially horizontal lines is seen in Fig. 13b, image (e)-(h). Their slopes become nearly vertical, nearly parallel to the initially vertical grid lines. This signifies severe shear strains, which exist in the rubber-rich surface layer.

#### Failure of Ligaments and Surface Layer

The crack growth is explained as a progression of ligament extensions and failures. On the outside surface, however, it is a progression of void formation and coalescence in the rubber-rich layer.

Failure of the ligaments could be expected to occur at a limiting strain (assuming uniform strain rate). Typically, the limiting strain would be reached first at the blunt end of the triangular pre-crack zone. Exceptions are possible, however, because the original lengths of the ligaments are not all the same. The original length relates to the vertical debond length between crystals and rubber, beyond the position where the rubber is keyed and fixed by crystals; see Figs. H3 and H4. With random crystal arrangements, this debond length must be random, too, causing the strain to vary from ligament-to-ligament. Consequently, ligament failures will not advance exclusively from the blunt end of the crack; some will occur further ahead of the blunt end.

Failure of the rubber-rich surface layer is analogous. Figure 13b shows that voids typically appear where tensile strains and shear strains are both large. Again, the magnitude of these strains is related to the local conditions, especially the positions where the surface layer is keyed to crystals. With random crystal distribution, the limiting value of combined tensile and shear strain can occur within the triangular pre-crack zone as well as at the blunt end of the zone.

What is this limiting value? Why are the voids elliptical with major axes parallel to the tensile direction? Probable answers were found from crude tests using broad rubber bands. Tensile failure surfaces were perpendicular to the load, suggesting that maximum principal stress or strain is the failure criterion. Figure H6 illustrates that a shear strain, when combined with a large normal strain, significantly increases the principal strain, but changes the principal strain direction only a small amount. Consequently, failure leading to a void in the rubber-rich surface layer would be a localized rupture or crack with

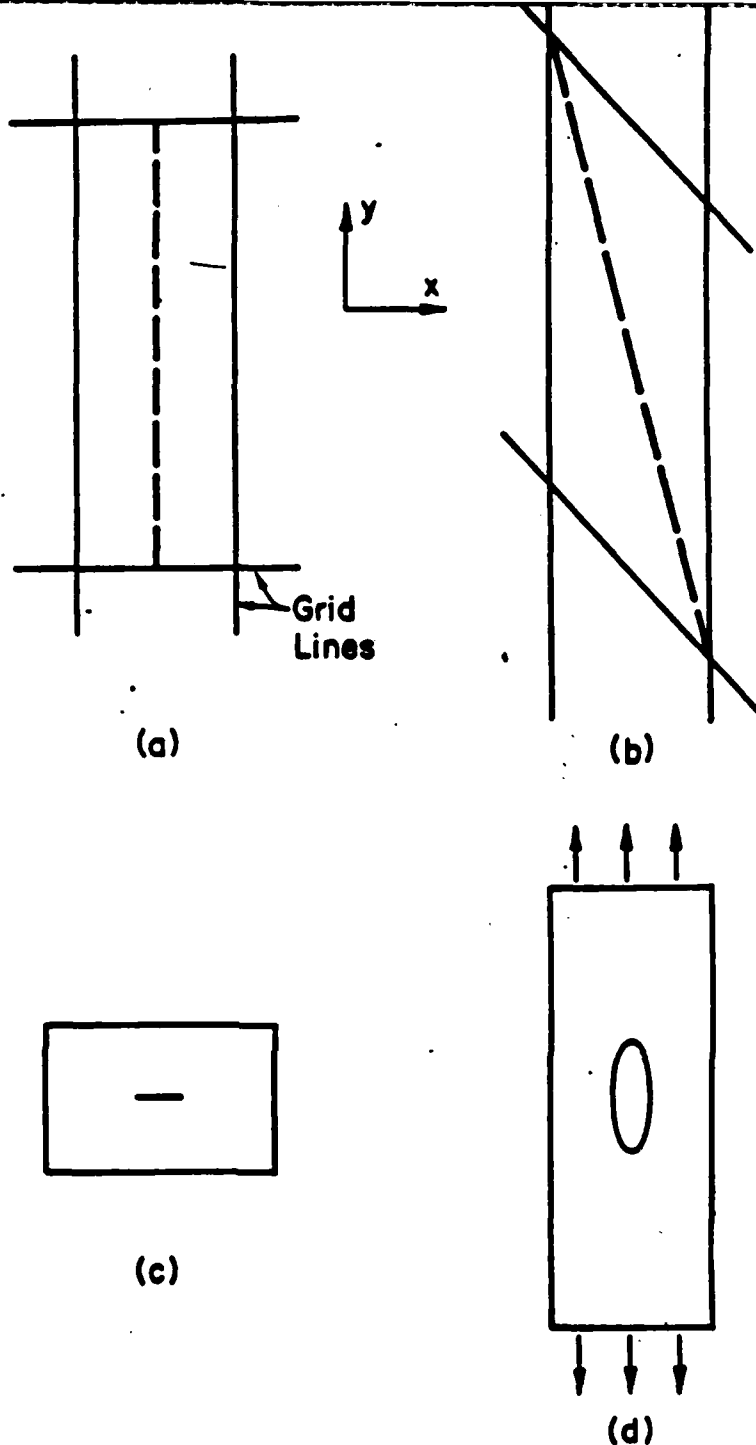


Fig. H6 (a) Grid lines for the case of  $\epsilon_y = 3$  and  $\epsilon_x = \gamma_{xy} = 0$ ;  
 (b) same condition except  $\gamma_{xy}$  is large. The bold dashed lines represent maximum extensions and maximum principal strain directions. (c) represents a crack in a rubber sheet and (d) represents the sheet when its height is extended by an average strain  $\epsilon_y = 3$ . The crack lips deform into a tall elliptical boundary.

the crack plane perpendicular to the principal strain. This is essentially perpendicular to the direction of tensile loading.

When such a crack is cut in a broad rubber band and the band is stretched, the crack opens into an ellipse. For large strains, the ratio of lengths of the vertical (the load direction) and horizontal axes of the ellipse is approximately equal to the principal strain ratio. This is illustrated in Fig. H6(d), where  $\epsilon_y \approx 3$ . Correspondingly, the elliptical voids in Fig. 13b exhibit nearly vertical principal axes.

This model of void formation and coalescence in the specimen surface is one in which small cracks are developed in the rubber-rich surface layer ahead of the main crack. In the unloaded condition the crack planes would be perpendicular to the maximum principal strain direction -- essentially the y direction, the loading direction. In the highly strained condition, the lips of each small crack extend into an elliptical shape with major axes essentially parallel to the y direction. These cracks grow longer (in the x direction) as the specimen is stretched, causing the elliptical void to enlarge. When adjacent cracks join, their corresponding voids coalesce.

#### Path of Crack Growth

Let Fig. H7 represent (an idealized schematic diagram of) a blunt crack and pre-crack zone, leading to the candidate path of crack extension. How can we rationalize the probable path of the crack as it extends among the crystals?

Returning to the reasoning of Fig. H3, the onset of debonding along vertical crystal/rubber interfaces follows debonding at horizontal interfaces. The global strain level at which horizontal debonding

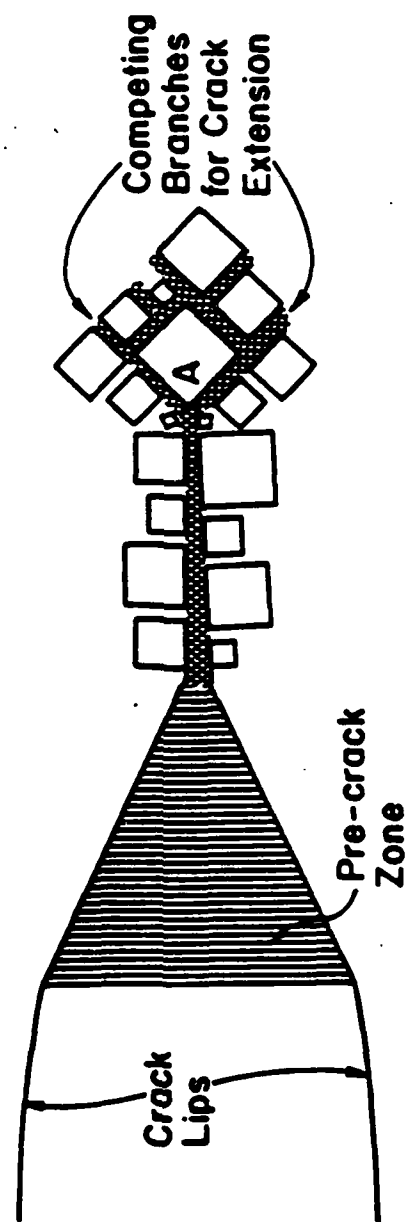


Fig. H7 The path of crack extension. The crack is expected to follow the route where  $\epsilon_y$  is initially largest, the upper branch in this case.

occurs is inversely related to the thickness of the horizontal elements of matrix rubber. Accordingly, the onset of debonding along vertical interfaces is hastened in regions where the horizontal portions of rubber are thinner than elsewhere.

Where debonding along vertical surfaces commences, the local stiffness of the composite is greatly reduced and further deformation concentrates in that neighborhood. By this argument, the path of the pre-crack zone, and subsequently the path of the crack itself, follows the route along which the vertical height of matrix material is smallest. In the case of Fig. H7, the upper branch beyond point A would be the path of crack extension.

#### Crack Stoppers, Bridges

Another fascinating behavior is observed in the deformation sequence seen in Fig. 13b [images (j)-(m)], deformation that proceeds as the specimen is stretched. In image (j), the main crack has achieved a certain length, but subsequent views show no increase of its length. Instead, a new pre-crack zone opened slightly below the tip of the main crack. Voids grew and coalesced in that zone until it was separated from the main crack by a bridge of highly strained material. By (m) the bridge failed and the new zone joined the main crack.

An explanation of crack arrest is required. The crack extends inexorably along a single path, but the path can lead to a crack stopper -- like a dead-end street. This is the condition where a local crystal configuration inhibits the development of large strains. Such a condition is illustrated schematically in Fig. H8. Meanwhile, a point B will exist in the neighborhood of A, where local strains are large, and

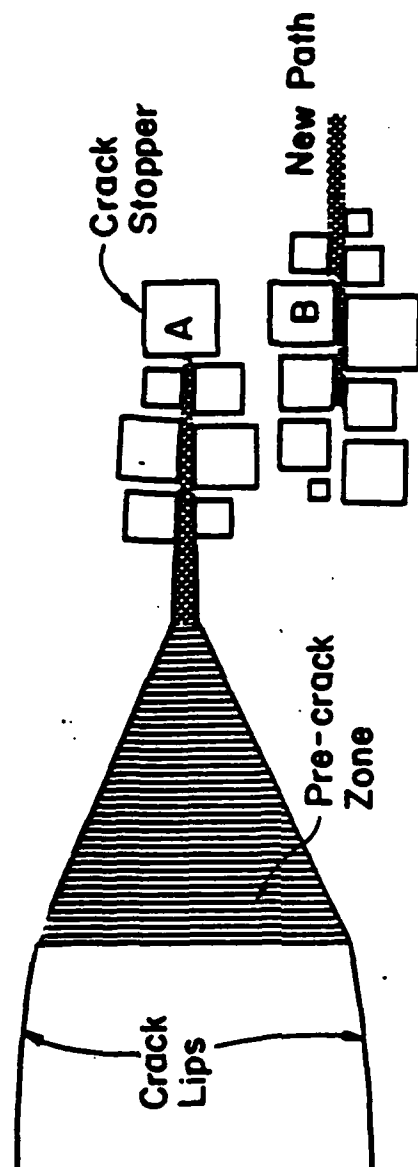


Fig. H8 The path of crack extension. Here, the crystal configuration at A inhibits large strains and the crack must terminate. A neighboring path of crack extension develops at nearby strain concentration B.



a new crack path is established. The localization of deformation continues along this new path until it leads, by chance, to a crack stopper -- to a local zone where large strains cannot occur.

#### References

- [H1] Bills, K. W., Jr., and Blatz, P. J., "Nonlinear Fracture Mechanics - New Theories of Solid Propellant Response and Fracture Behaviors," Naval Weapons Center Technical Publication 5684, China Lake, CA, February 1975.